

On the use of silicon microcantilevers for mass detection and adsorption of water molecules

By

LAKSHMOJI KOSURU

Enrolment No.: PHYS02200804007

Indira Gandhi Centre for Atomic Research

Kalpakkam, 603102, Tamil Nadu, India

*A thesis submitted to the
Board of Studies in Physical Sciences
In partial fulfillment of requirements*

For the Degree of

DOCTOR OF PHILOSOPHY

of

HOMI BHABHA NATIONAL INSTITUTE

Deemed University

Mumbai, India



October, 2013

Homi Bhabha National Institute

Recommendations of the Viva Voce Board

As members of the Viva Voce Board, we certify that we have read the dissertation prepared by **Lakshmoji Kosuru** entitled “**On the use of silicon microcantilevers for mass detection and adsorption of water molecules**” and recommend that it may be accepted as fulfilling the dissertation requirement for the Degree of Doctor of Philosophy.

Date:

Chairman – Dr. C.S. Sundar

Date:

Convener – Dr. A.K. Tyagi

Date:

External Examiner -

Date:

Member 1 – Dr. G. Amarendra

Date:

Member 2 – Dr. Sitaram Dash

Date:

Technical advisor – Dr. J. Jayapandian

Final approval and acceptance of this dissertation is contingent upon the candidate's submission of the final copies of the dissertation to HBNI.

Date:

Place:

CERTIFICATE

I hereby certify that I have read this dissertation prepared under my direction and recommend that it may be accepted as fulfilling the dissertation requirement.

Date:

Place:

(A.K. Tyagi)

STATEMENT BY AUTHOR

This dissertation has been submitted in partial fulfillment of requirements for an advanced degree at Homi Bhabha National Institute (HBNI) and is deposited in the Library to be made available to borrowers under rules of the HBNI.

Brief quotations from this dissertation are allowable without special permission, provided that accurate acknowledgement of source is made. Requests for permission for extended quotation from or reproduction of this manuscript in whole or in part may be granted by the Competent Authority of HBNI when in his or her judgment the proposed use of the material is in the interests of scholarship. In all other instances, however, permission must be obtained from the author.

Lakshmoji Kosuru

Kalpakkam

October 2013

DECLARATION

I, hereby declare that the investigation presented in the thesis entitled “ On the use of silicon microcantilevers for mass detection and adsorption of water molecules” submitted to Homi Bhabha National Institute (HBNI), Mumbai, India, for the award of degree of Doctor of Philosophy in Physical Sciences is the record of work carried out by me during the period from September 2008 to October 2013 under the guidance of Dr. A.K. Tyagi, Head, Surface and Nanoscience Division, Materials Science Group, Indira Gandhi Centre for Atomic Research, Kalpakkam. The work is original and has not been submitted earlier as a whole or in part thereof for a degree / diploma at this or any other Institution / University.

Lakshmoji Kosuru

Kalpakkam

October 2013

Dedicated to my parents

ACKNOWLEDGEMENTS

The outcome of this thesis is an effort and support of many wonderful people to whom I sincerely express my deepest gratitude. The first person to thank is my research supervisor **Dr. A.K. Tyagi**. I am grateful to him for giving me an opportunity to pursue my thesis in the area of cantilever sensors. I express my deep sense of gratitude to him for his invaluable guidance, suggestions, constant support and encouragement.

I wish to express my sincere thanks to **Dr. C.S. Sundar** for sharing his knowledge and scientific understanding with me. His critical comments helped me to improve my understanding on the subject as well as my experimental skills. I am also grateful to him for critically reviewing this thesis.

I express my deep sense of gratitude to **Dr. J. Jayapandian** for his invaluable guidance, suggestions, constant support and encouragement. His hospitality to any new person he meets is incomparable. Every time I spoke to him, his power packed words gave me tremendous motivation and confidence in the work that I do. His optimism, enormous patience, very caring nature, vast knowledge and freedom he gave, made my work very smooth. It is great honor for me to work with such eminent and valuable scientist.

This thesis would not have been possible without the help, support and valuable suggestions from **Dr. K. Prabakar**. A person who added values to my every result in this thesis work is him. I highly acknowledge the support extended by him during my ph.d time which was invaluable for the experimental work. He is very kind and careful to me and taught me many finer aspects of doing experiments and writing articles. I always wonder at his patience while correcting the draft of my papers and the thesis in making them free of grammatical and technical errors. His ever availability, friendliness and kindness have always kept my work at ease.

It gives me immense pleasure to thank the members of the doctoral committee **Dr. G. Amarendra** and **Dr. Sitram Dash** for their suggestions during the progress.

I take this opportunity to thank with great pleasure for strong support from the members of Electronics and Instrumentation section, **Smt. Usha rani, smt. O.K. Sheela, Raghuram** and other members of MSG. I express my sincere thanks to **Dr. S. Tripura Sundari** for critically reviewing my research articles and thesis.

I take this opportunity to sincerely acknowledge the **Department of Atomic Energy, Government of India**, for providing financial assistance in the form of Junior and Senior Research Fellowships which buttressed me to perform my work comfortably. I thank the former and present Directors, IGCAR, **Dr. Baldev Raj** and **Dr. P.R. Vasudeva Rao** and Associate Director, RMG, IGCAR, **Dr. M. Saibaba**, for providing me accommodation, necessary infrastructure and resources to accomplish my research work.

I wish to express my sincere thanks to **Mr. Atul Kumar** for his diversified help and fruitful scientific discussions during the course of work.

I highly acknowledge the support extended by **Mr. Sudarsan, Mr. Piyush, Dr. J. Brijjita and Dr. Prasanna sahu** for my experimental work. I acknowledge **Dr. Sandhip dhara** for providing micro-Raman facility.

I express my heartfelt thanks to my friends **D. Sri Maha Vishnu, Jammu Ravi, Jagadeesh sure, D. Sharath, K. Siva Srinivas, Pradeep Samantray, Illayaraja, Naveen, Herojit, N. Mariyappa, Sudhansu pati, Bhupathi, Maneesha, Pravathi, Debasmita, Ravi kirana, Padmasri, Ramya, Revathi, Lakshmi, Priyada, Samba, Sadhu, Avinash, Bonu venkata ramana, Yadagiri, B. Siva kumar, Trinadha raja**, and all others residing at the enclave for their numerous help, support and enjoyable company for making the life at Kalpakkam more cheerful. I would like to thank my JNV friends **Vamsi, Kishore, Sekhar, Brahma Reddy, Gopal Raju, Sushma, Raghavendra, Durga** for their valuable help, enjoyable company and support. I would also like to thank all my **Teachers**, who throughout my educational career have supported and encouraged me to believe in my abilities. They have directed me in various difficult situations, which have helped to reach this accomplishment.

I am also indebted to my father **Shri. Appa Rao**, Mother **Smt. Adi Lakshmi**, my brother **Ramoji, Vidya**, and **Varshith**, Sister **Padmaja**, Brother-in-law **Shri. B. Nageswara Rao, Divya, Pavan** and other family members for their relentless support, encouragement and love.

Finally, I thank **almighty** for providing me opportunity to step into the world of science.

CONTENTS

	Page. No.
Abstract	xiii
List of figures	xv
List of Tables	xxii
List of Abbreviations	xxiii
CHAPTER 1 Microcantilever based sensors	1
1.1 Motivation of the present thesis	1
1.2 Introduction to microcantilever based sensors	3
1.3 Modes of operation of microcantilevers	7
1.4 Readout techniques	9
1.4.1 Optical lever method	9
1.4.2 Piezoresistive method	11
1.4.3 Capacitive method	13
1.4.4 Piezoelectric method	14
1.5 Excitation methods	14
1.6 Microcantilever theory	16
1.6.1 Dynamic mode	16
1.6.1.1 Expression for natural frequency of cantilever beam	16
1.6.1.2 Higher modes vs microcantilever dimensions	18
1.6.1.3 Mass estimation	21
1.6.1.4 Factors affecting mass sensitivity	23
1.6.1.5 Q-factor of microcantilevers	23
1.6.2 Static mode	24
1.7 Objectives of the present thesis	30
1.8 References	31

CHAPTER 2	Experimental techniques	37
2.1	Microcantilevers used in the present work	37
2.2	Handling and <i>Piranha</i> cleaning of microcantilevers	39
2.3	AFM head	40
2.4	Experimental set up for water adsorption studies on microcantilevers	45
2.5	Nano vibration analyzer	46
2.6	FEM analysis	49
2.7	Functionalization of microcantilevers with polymers	50
	2.7.1 Synthesis of PAAm and PVP polymer solutions	50
	2.7.2 Dip coating setup	50
2.8	Preliminary studies on identifying the higher modes of vibration of microcantilevers	51
2.9	Mapping of mode shape of microcantilever vibrations	54
2.10	Micro Raman studies on microcantilevers	57
	2.10.1 Effect of laser power	60
	2.10.2 Residual stress in microcantilever	62
2.11	References	64
CHAPTER 3	Microcantilever based mass sensors	66
3.1	Enhancing the sensitivity of microcantilever based mass sensors	66
	3.1.1 Mass sensitivity	67
	3.1.2 Quality factor	69
	3.1.3 Comparison of mass sensitivities of microcantilevers when working at higher modes and reducing dimensions	71
	3.1.3.1 Discussions	76
3.2	Tailoring the cantilever for enhanced mass sensitivity – FEM simulation studies	77
3.3	Estimation of dynamic range of mass using millimeter sized cantilever	84
3.4	Polymer coated microcantilevers for gamma radiation detection	87

3.5	Conclusions	93
3.6	References	94
CHAPTER 4	Adsorption of water molecules on uncoated Si microcantilevers	98
4.1	Influence of adsorption induced surface stress on stiffness changes of microcantilevers	99
4.1.1	Literature survey	99
4.1.2	Results and discussions	102
4.2	Higher modes of vibration of Si microcantilever for humidity detection	108
4.3	Adsorption and desorption kinetics of water molecules on uncoated microcantilever	110
4.3.1	Kinetics during dynamic mode	110
4.3.2	Kinetics during static mode	114
4.4	Stress concentrators as origin of uncoated microcantilever bending	116
4.4.1	Literature survey	116
4.4.2	Results and discussions	119
4.5	Conclusions	124
4.6	References	126
CHAPTER 5	Summary and scope of future work	129
PUBLICATIONS		132
Appendix A – Programs used in NVA		
A -1	Program for estimation of natural frequency of MC	134
A-2	Program for mapping the mode shape of vibration of MC	135

ABSTRACT

Present thesis deals with two important aspects of microcantilever (MC) based sensors. In the first part, methods to enhance the MC mass sensitivity are studied. Working at higher modes and reducing the dimensions of MC are compared. Resonance frequency of MC is measured using the laser photo diode arrangement of an Atomic Force Microscopy (AFM) head and Nano Vibration Analyzer (NVA). Micro-Raman spectroscopy was used to estimate the residual stress in MCs. Finite Element Modeling (FEM) analysis was extensively used to identify and assign the mode shapes of MC, obtained experimentally. A precise dip coating setup is indigenously developed to add polymer mass on MCs. It is shown that mass sensitivity increases linearly with increase of eigenvalue (λ_n^2) and decreasing dimensions (T/L^2) where T is thickness and L is length of MC. Using FEM simulations, mass sensitivities for various nanostructures like nanobelt, nanowire and nanotube which can be attached to a conventional MC are studied. Factors affecting the dynamic range of cantilever based mass sensors are discussed. Polymer (PAAM and PVP) coated MCs are also explored for gamma radiation dosimeter application.

In the second part of the thesis, resonance frequency shift upon adsorption of water molecules in MCs with reducing dimensions are investigated. AFM head placed inside an air tight chamber, purged with dry/wet N₂ is used for these studies. Experimental evidence has been presented to show that the effect of dimensions of MC leads to negative or positive frequency shift during adsorption, clearly depicting the competition between mass loading and stiffness changes. The relative change in

stiffness of MC is seen to increase linearly with the surface stress scaled with cube of width to height ratio of MCs, confirming the dimensional dependence of adsorption induced stiffness change. Adsorption and desorption kinetics of water molecules on MC surface are studied. Apart from this, various possible mechanisms responsible for deflection of uncoated Si MC when exposed to water molecules is discussed. It is shown that the bending is a consequence of difference in surface roughness on front and back side of uncoated MCs. The results are explained in terms of the large number of “stress concentrators” on the back side compared to front side of MC in accordance with the recent theoretical models. Finally it is demonstrated that uncoated MCs can be effectively used as a humidity sensor both in static and dynamic mode.

LIST OF FIGURES

Figure No.	Title of Figure	Page No.
1.1	General schematic of cantilever sensing principle. Cantilever is a fixed free beam which transduces direct interaction with specific target analyte through electrical, thermal, or optical signals that can be both measured and recorded. This figure is adapted from reference [26]	4
1.2	Microcantilevers are extensively studied as physical, chemical and biological sensors. These are operated in two modes, dynamic and static. In the dynamic mode shift in resonance frequency (Δf) is measured before and after the addition of mass or environmental damping. In static mode, cantilever bending (Δz) due to differential surface stress is measured. Optical, piezoresistive, capacitance, or electron tunneling methods, are some of the known methods for detecting the cantilever vibrations or bending	8
1.3	Schematic of optical readout method. The movement of the cantilever is detected by a reflected laser beam focused on cantilever and a position sensitive detector. This figure is adapted from reference [79]	11
1.4	Schematic of array of Piezoresistive MC (adapted from [84]). The greatest advantage of this technique is read-out electronics can be integrated on the same silicon chip. Wheatstone bridge configuration is also shown in the figure.	12
1.5	The natural frequency of MC with mode number. Frequency of MC is increasing with mode number as a function of parabola	19
1.6	Variation of natural frequency with (a) cantilever length and (b) thickness. Frequency of MC is proportional to $1/L^2$ and thickness of MC	20
1.7	Schematic of cantilever beam deflection. The radius of curvature R is derived as a function of deflection of the beam	25
1.8	Cantilever beam geometry and bending moment diagram. σ_1 and σ_2 stresses in upper and lower surface of the beam respectively. M is the bending moment induced in the cantilever beam	26

1.9	Stress in a thin film on a cantilever. (a) As the film expands the cantilever bends down. The resulting stress in the film is compressive as its expansion is hindered and balanced by the bending of the cantilever. (b) For a contracting film the cantilever bends up and the resulting stress in the film is tensile. This figure is adapted from reference [1]	29
2.1	SEM and AFM images of MC1 used in this study. Average roughness of MC1 is about 0.85nm	38
2.2	(a) Commercially available gel pack box in which usually MCs are shipped (b) handling of the MCs using a tweezer	39
2.3	Contact angle measurements on a) before and b) after <i>Piranha</i> cleaning of MCs. The contact angle was found to reduce from 95° to ~ 29° after <i>Piranha</i> cleaning	40
2.4	Photograph of AFM head and schematic of control electronics panel	41
2.5	The four quadrant photo diode system in AFM. Normal constituent corresponds to difference of AB and CD photo diode signal and it gives information about vertical vibrations. Lateral constituent corresponds to difference of AD and BC signals and it gives information about lateral and torsional vibrations	42
2.6	First vertical bending (VB1) and lateral bending (LB1) modes of MC1 obtained using AFM shown in (a) and (b) respectively. Amplitude of vibrations is in nA. The direction of vibration for VB1 and LB1 is shown as inset	43
2.7	Deflection response of MC1 with time when relative humidity is reduced from 50% to 6%	44
2.8	Calibration curve obtained by performing force distance curve on hard Si surface in motion. From linear contact part, slope was found to be 20 pA/nm shown in inset. (b) Deflection direction of MC towards back during positive deflection signal of MC	44
2.9	(a) Schematic diagram and (b) Photograph of the experimental set up used for water adsorption studies. Dry/wet N ₂ gas is purged into chamber to reduce/increase relative humidity in the chamber	46

2.10	(a) Block diagram and (b) photograph of experimental setup used for estimating the natural frequency of the cantilever using NVA. (c) Resonance spectrum of MC1 obtained using NVA	48
2.11	Mode shape of first vertical bending mode of MC1. Mesh used was 3nm. Normalized amplitude of vibration of mode is shown	49
2.12	MCs are coated with polymer solution using this dip coating setup. MC and polymer solution in a container are mounted on two 3-axis micro manipulators, and by carefully observing through a digital microscope, MC was dipped into the solution (see inset), kept for 20 minutes and removed	51
2.13	Experimental results of vertical bending (VB) signals of the microcantilever studied in the present work using AFM head. Seven unique modes of vibration are identified and assigned from FEM simulations (shown as stick). Some of the mode shapes are shown as inset	52
2.14	Frequency spectra of MC1 obtained using NVA. The peaks in the spectrum corresponding to vertical bending modes. VB1 has higher amplitude of vibration as compared to other higher modes	53
2.15	LF signal of MC1 obtained using AFM. This signal showing both Lateral (LB) and torsional bending (TB) of MC1. The peaks 8 and 9 corresponds to LB1 and TB1 modes of MC1	54
2.16	Mode shape of vibrations along the length of MC for its first three VB modes. The data is fitted to polynomial fit	55
2.17	Mode shapes of VB1, VB2, VB3 and VB4 of MC1 obtained using FEM analysis (simulation) and NVA (experimental). It may be noted that FEM results show normalized amplitudes, where as NVA results are real amplitude of vibrations.	56
2.18	Raman shift at room temperature on the substrate of the cantilever with Lorentzian fit	60
2.19	(a) Variation of Raman shift with increasing laser power at three different positions namely free end, middle and fixed end of the MC1 (b) Three different positions on a free standing MC1	61

2.20	Raman shift along the length of the microcantilever in free standing position and resting on a substrate as shown inset. Stress calculated from Raman shift using equation 2.1 is shown in right axis of the figure. Arrow shows the laser probing direction and for these experiments 2 mW laser is used	63
3.1	Estimation of quality factor from resonance spectrum (VB1) of MC1	70
3.2	Shift in natural frequency of first vertical bending mode (VB1) of MC1 for an added mass of 1.62 ng	71
3.3	Variation of mass sensitivity with (a) square of Eigen value for MC1 and (b) T/L^2 of MC1, MC2 and MC3 at VB1	73
3.4	Variation of Q-factor with (a) square of eigenvalue for MC1 and (b) T/L^2 of MC1, MC2 and MC3 at VB1	75
3.5	Variation of mass sensitivities of VB, LB and TB modes with square of the mode number	77
3.6	Frequency – displacement and phase angle curve for three different nanostructures namely NC, NW and NT. Right axis shows the corresponding phase angle behavior at resonance. Inset of these figures shows the geometry and dimensions of NC, NW and NT used for simulations.	79
3.7	Variation of mass sensitivity of CNT with varying the position of gold from the fixed end	82
3.8	(a) Step position introduced at 200nm from fixed end of the NC (b) Variation of the resonance frequency of NC with position of step discontinuity along its length	82
3.9	Frequency shift of cantilevers whose length is varied from 4 mm to 10 mm for the addition of wide range of mass	85
3.10	Resonance spectrum of the cantilever used obtained using NVA. Resonance spectrum is fitted to lorentzian fit	85

3.11	Variation of frequency shift of cantilever of length 8.3 mm with the addition of mass is compared theoretically and experimentally. The open circle shows the theoretical values and solid circle shows the experimental values. Inset of figure shows the linear variation between actual mass (calculated from volume and density of copper wire pieces) and estimated mass using NVA	86
3.12	Optical photograph of the PVP coated MC. Polymer solution is coated only at the free end to avoid stiffening effect	89
3.13	Shift in resonance spectrum of MC due to added polymer. The estimated mass due to PVP coating on MC is about 31pg using equation 1.14	90
3.14	Comparison of frequency shift of PVP coated and uncoated MC when exposed to different gamma doses	91
3.15	Q-factor of PVP coated and uncoated MC when irradiated to different gamma doses	91
3.16	PVP surface after (a) 2 krad (b) 20 krad (c) 50 krad (d) 80 krad gamma irradiation	92
4.1	Relative shift in resonance frequency with increasing RH in MC1, MC2 and MC3	102
4.2 (a)	Adsorption isotherm of adsorbed water on the SiO ₂ surface taken from [30]. Square symbols in this figure are the total thickness of the adsorbed water layer calculated from the intensity of H-O-H bending vibration peak.	103
4.2 (b)	Estimated mass on three MCs with increasing RH. Water layer thickness on SiO ₂ surface was taken from Assay and Kim data [30] and density of water was taken as 1000 kg/m ³	103
4.3	Relative shift in resonance frequency with relative mass on three MCs. This figure also shows the estimated frequency shift in MC1	104

4.4	(a) Variation of stiffness change with respect to mass per unit area of three MCs. This was estimated by converting the difference of fig.4.1 and 4.2(b) as Δk using equation 4.3. (b) Surface stress generated during adsorption in all the MCs with respect to mass per unit area. This was estimated from cantilever bending data using Stoney's equation. (c) Linear fit of $(\Delta k/k)$ with $(\Delta\sigma)$ in MC2 and MC3	106
4.5	$(\Delta k/k)$ Vs $(\Delta\sigma)$ scaled to $(W/T)^3$ ratio in MC2 and MC3. Collapsing of the data in this figure is the experimental evidence for the dependence of stiffness changes during adsorption to surface stress and MC dimensions	108
4.6	The frequency shifts for (a) VB1 and (b) VB7 modes of vibration of MC1 for the change of RH from 50% to 6%	109
4.7	Variation in the resonant frequency of MC1 and the relative humidity as a function of time	111
4.8	Variation in the resonant frequency of the microcantilever and desorbed/adsorbed mass as a function of time (a) during desorption and (b) adsorption of water molecules. Desorption is fitted to single exponential decay with rate constant of 0.000573. Initial adsorption is well fitted to Langmuir fit as shown in inset in 4.8 (b)	112
4.9	Variation of deflection of the MC as a function of time during desorption and adsorption of water molecules	114
4.10	Differential surface stress estimated from deflection of the MC during (a) desorption and (b) adsorption of water molecules. Adsorption and desorption data fits to Langmuir isotherm and single exponential decay respectively	115
4.11	Deflection response of MC1 for four adsorption-desorption cycles when RH switched between 50% to 6%. Laser was focused on back side of MC1	119

- 4.12 Long time deflection response of MC when laser is focused on (a) back and (b) front surface of MC1 120
- 4.13 Surface morphology of (a) front and (b) back side Si microcantilever used in the present study. Scan area is $4 \times 4 \mu\text{m}^2$. Inset shows a typical horizontal cross section line profile. Inset also shows the histogram plots of “stress concentrators” on front and back surface. This was estimated by considering a threshold surface at 50 % from maximum height in each case 123
- 4.14 Deflection response of MC1 and MC2 during desorption of water molecules when RH is switched from 50 % RH to 6 %. Inset shows Surface morphology of front and back side of MC2. The estimated RMS roughness is $\sim 2\text{nm}$ on both sides. This result is a experimental evidence for the roughness induced MC bending 123

LIST OF TABLES

Table. No.	Title of Table	Page. No.
1.1	Summary of the microcantilever applications for medicine, biology, chemistry and environmental monitoring. [68]	6
2.1	Details of four different microcantilevers used in the present study. The natural frequency was measured using AFM head and spring constant values are estimated using Sader's method [2]	38
2.2	Frequency values of MC1 for all modes of vibrations obtained using AFM, NVA (experimental) and FEM analysis (simulation).	57
3.1	Resonance frequencies before (f_1) and after coating polymer (f_2), Q-factor before (Q_1) and after addition of mass (Q_2), shift in frequency due to added mass (Δf) and estimated mass sensitivity (S) for MC1, MC2 and MC3	72
3.2	Advantages and disadvantages of the each method i.e. working at higher modes and reducing the dimensions of MC	76
3.3	Comparison of FEM values with theoretical and experimental values of three different single walled CNTs	81
4.1	Resonance frequency (f_1), shift in frequency (Δf) and sensitivity of various modes of vibration of MC1 when RH is varied from 50 % to 6%.	109

LIST OF ABBREVIATIONS

MC	Microcantilever	SEM	Scanning Electron
MEMS	Micro		Microscope
	Electromechanical	PDMS	Poly(dimethylsiloxane)
	Systems	DFL	Vertical bending photo diode signal
NEMS	Nano		
	Electromechanical	LF	Lateral bending photo diode signal
	Systems	VB	Vertical Bending
FEM	Finite Element	LB	Lateral Bending
	Modeling	TB	Torsional Bending
AFM	Atomic Force	RH	Relative Humidity
	Microscope	CAD	Computer Aided
QCM	Quartz Crystal		Design
	Microbalance	TEM	Thermo
SAW	Surface Acoustic Wave		Electro Mechanical
SAM	Self-assembled	PAAm	Poly Acrylamide
	Monolayer	KPS	Potassium PerSulfate
CMOS	Complementary Metal	TEMED	Tetramethylenediamine
	Oxide Semiconductor	PVP	PolyVinylPyrrolidone
PSD	Position Sensitive	DP	Deformation Potential
	Photo Detector	RS	Raman Shift
CCD	Charge-Coupled	CNT	Carbon NanoTube
	Device	NC	Nano Cantilever
NVA	Nano Vibration	NW	NanoWire
	Analyzer	NT	NanoTube

Chapter 1 - Microcantilever based sensors

This chapter describes the basic principle of microcantilever (MC) based sensors. Different modes of operations, detection techniques and excitation methods are discussed. General theory of dynamic and static mode of cantilever beam is presented in this chapter. Principle of mass sensing and the estimation of mass sensitivity from MC frequency shift due to addition of mass are derived. Estimation of surface stress from deflection of MCs using Stoney's equation is presented. Some of the important chemical and biological applications of these sensors from literature are briefed. Finally objectives of the thesis are presented.

1.1 Motivation of the present thesis

Microcantilever (MC) based sensors have been demonstrated to be extremely versatile sensors and have potential applications in physical, chemical and biological sciences [1, 2]. The greatest advantage of these sensors is that they can be batch produced using conventional micromachining techniques and offer improved dynamic response, greatly reduced size, high precision and increased reliability compared with conventional sensors [3]. Micro Electro Mechanical systems (MEMS) and Nano Electro Mechanical systems (NEMS) based resonators and cantilevers have been extensively studied in recent times for their ultra sensitive mass detection [4–8]. In fact, systems capable of detecting masses in the atto and zeptogram ranges have been reported [9–11]. For high sensitivity, these sensors are operated in dynamic mode by measuring the cantilever's resonant frequency shift before and after loading the mass. The resonant frequency of a cantilever is given

by $f = \frac{1}{2\pi} \sqrt{\frac{k}{m^*}}$, where k is spring constant and m^* is effective mass of the

cantilever [12, 13]. The mass change Δm is obtained from the resonant frequency

shift Δf due to added mass by $\Delta m = \frac{-2m}{f} \Delta f$. To achieve high-sensitivity in mass

detection, it is necessary to use a cantilever with a small mass and a high resonant frequency. Very short cantilevers with high resonance frequency are, therefore, promising in extending the detection limit down to a few molecules [11]. Apart

from reducing the dimensions, one can also physically tailor these cantilevers for enhancing the sensitivity, since sensitivity also depends on effective mass. Besides,

to increase the resonance frequencies of a cantilever, higher resonant modes of the cantilever have been also investigated, and found to have enhanced sensitivity [14].

The sensitivity of the resonant cantilever when used as a mass sensor also depends on the spectral resolution, which is directly related to the quality factor (Q -factor) of the resonant mode [15]. In the first part of the thesis some of these issues associated

with enhancing the mass sensitivity of MCs are addressed. Working at higher modes and reducing the dimensions of MC are compared. Finite Element Modeling

(FEM) analysis was extensively used to identify and assign the mode shapes of MC obtained experimentally. A precise dip coating setup is developed to add mass of

polymer films on MCs. Using, FEM simulations, mass sensitivities for various nanostructures like nanobelt, nanowire and nanotube attached to a conventional MC

are estimated and compared. Factors affecting the dynamic range of cantilever based mass sensors are discussed.

When used as mass sensor, it is normally assumed that the absorbed or adsorbed analyte does not affect the microcantilever stiffness, and the measured frequency

shift is proportional to the square root of the added mass [16]. In contrast, many experimental studies report that surface stress can significantly affect the stiffness of MC, making mass measurements qualitative [16-20]. Several theoretical models have been proposed to understand this phenomenon [21-25]. This effect is also dependent on MC dimensions and is addressed in the second part of the present thesis. Adsorption and desorption kinetics of water molecules on MC surface is studied. Experimental evidence is presented to show that the effect of dimensions of MC leads to negative or positive frequency shift during adsorption, clearly depicting the competition between mass loading and stiffness changes. Apart from this, various possible mechanisms responsible for deflection of uncoated Si MC when exposed to water molecules is discussed. It is shown that the bending is a consequence of difference in surface roughness on front and back side of uncoated MCs. Finally it is demonstrated that uncoated MCs can be effectively used as a humidity sensor both in static and dynamic mode.

1.2 Introduction to microcantilever based sensors

Unlike many other types of transducers for physical and chemical sensors, MCs are simple mechanical devices. They are tiny plates, typically 0.2–1 μm thick, 20–100 μm wide, and 100–500 μm long, which are connected on one end to an appropriate support for convenient handling much like the diving board. Figure 1.1 shows the general schematic of cantilever beam.

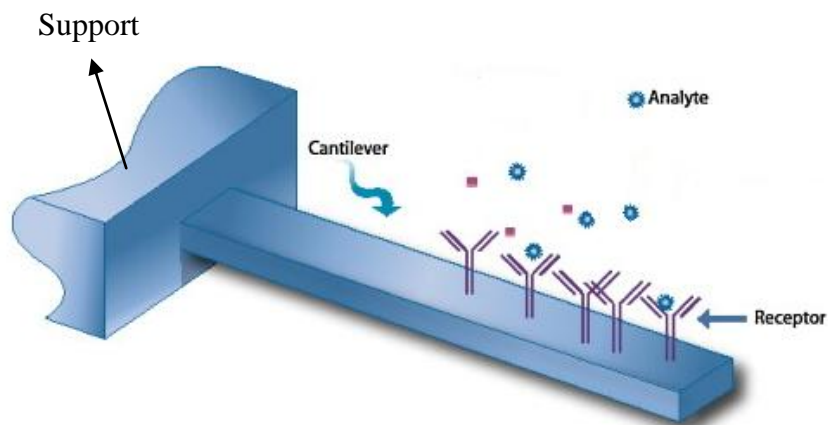


Figure 1.1 General schematic of cantilever sensing principle. Cantilever is a fixed free beam which transduces direct interaction with specific target analyte through electrical, thermal, or optical signals that can be both measured and recorded. This figure is adapted from reference [26].

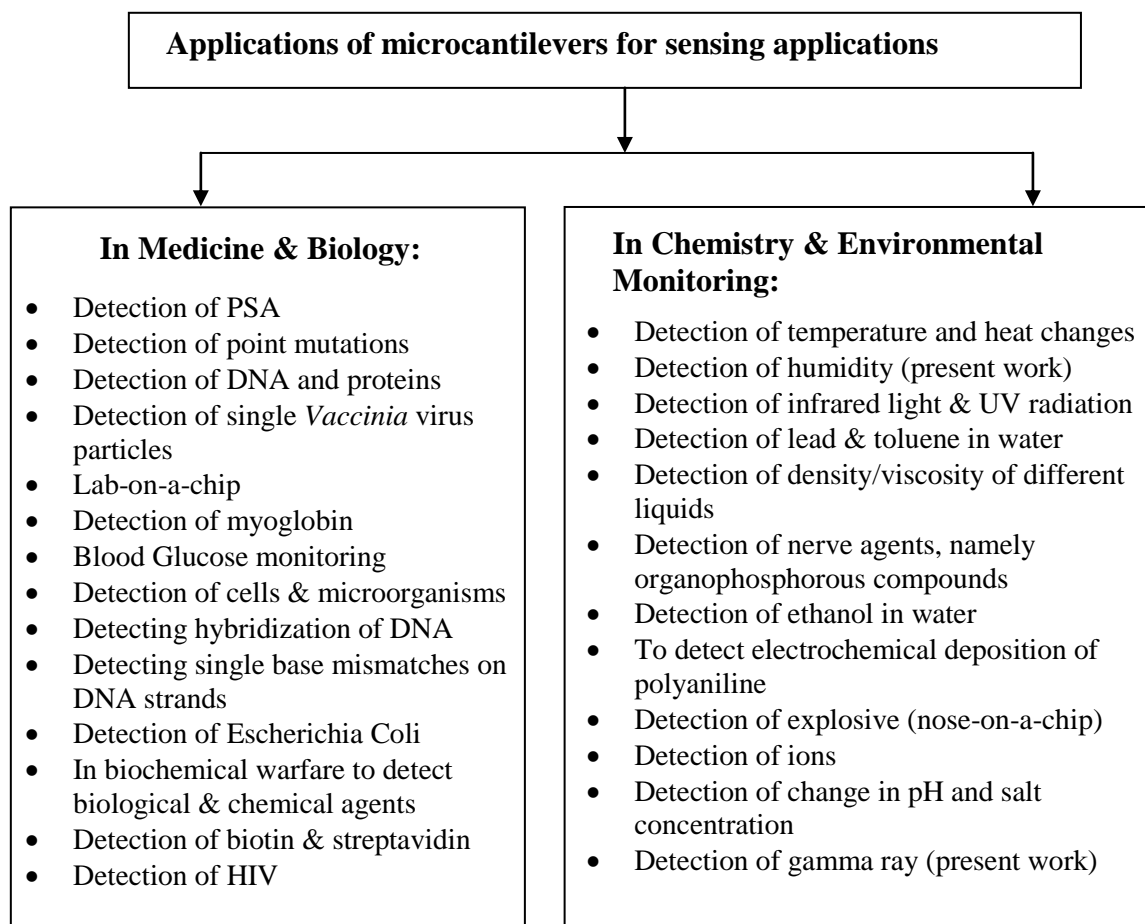
Micrometer-sized cantilevers became available with the invention of the atomic force microscope (AFM) in 1986 [27]. Once researchers began to use micromachined cantilevers as force probes in AFM, they became aware of the extreme sensitivity of the silicon and silicon nitride probes to a variety of environmental factors, such as acoustic noise, temperature, humidity, and ambient pressure [28]. It was found that a standard AFM cantilever could function as a microcalorimeter, offering femtojoule sensitivity and a substantial improvement over more traditional approaches. By measuring shifts in the resonance frequency of MCs, the researchers were able to show that MCs are mass-sensitive devices that perform more conventional piezoelectric gravimetric sensors [29–31]. The sensitivity of MCs to minute quantities of adsorbates was superior to that of traditional quartz crystal microbalance (QCM) and surface acoustic wave (SAW) transducers.

Simultaneously, Mark Welland group in Cambridge and the group around Jim Gimzewski and Christoph Gerber group at IBM, Zurich, started activities on MCs and both used the bimorph effect to perform sensitive photo thermal spectroscopy [32, 33]. Roberto Raiteri and Hans-Jurgen Butt from the Max-Planck-institute for Biophysics in Frankfurt reported on studies of surface stress changes induced electrochemically [34]. Unspecific binding of proteins to a hydrophobic surface was reported in 1996 [35]. The cantilever sensors can be used for online measurements of surface stress changes. This was demonstrated on a gold-coated cantilever exposed to alkanethiols [36]. These measurements illustrated that it is possible to follow the formation of a self-assembled monolayer (SAM) in real time, and the surface stress change was in this work seen to be related to the length of the alkane chain.

The aforementioned research, together with the wide availability of AFM instrumentation, generated substantial interest in cantilevers as a new platform for a variety of physical and chemical sensors. An increasing number of recent reports confirm the potential of MC sensors for environmental and biomedical applications, and the multifaceted functionality of MCs indicates their uniqueness as compared with more traditional sensor designs [1, 37]. Most common MC-based sensor applications are listed in Table.1.1. The main topics covered in the recent publications in the area of MC based sensing include the following: detection of vapours and volatile compounds (e.g., HF vapour) using individual MCs operated in beam deflection static mode [38-41], gas-phase sensing applications for solvents using piezo-resistive cantilevers [42-48], biochemical applications in static mode in liquids [49-51] (e.g., as a glucose sensor) and C-reactive protein detection using

dynamic-mode piezo-resistive MCs [18, 52]. Several efforts have investigated the usability of MC sensors as detectors for explosives [53-55] or Escherichia Coli bacteria [56, 57]. A pH sensor using hydrogel coatings [58, 59] has been suggested, as has the observation of electrochemical redox reactions using MCs [60]. Chemical sensor applications of resonant cantilevers have included humidity sensors [31, 61] or the detection of mercury vapors [30]. Complementary metal oxide semiconductor (CMOS) cantilevers coated with chemically sensitive polymers have previously been used for the detection of volatile organic compounds [31, 62-66]. A miniaturized system with an array of coated cantilevers for the simultaneous detection of hydrogen and mercury vapors was reported in [67].

Table 1.1 Summary of the microcantilever applications for medicine, biology, chemistry and environmental monitoring. [68]



The mass resolution of the cantilevers reported is in the range of a few picograms [31, 36, 62, 64, 69-71]. However, attogram detection with nano sized cantilevers in vacuum has been already reported [9]. From a scientific point of view, the challenge lies in optimizing cantilever sensors to improve their sensitivity until the ultimate limit is reached, which may be the nanomechanical detection of individual molecules. Torsional or lateral resonance modes are also exploited for improved mass sensing in dynamic mode [9, 72].

1.3 Modes of operation of microcantilevers

Cantilevers sensors are currently used in two fundamentally different ways, which may be denoted as static mode and dynamic resonant mode as shown in figure 1.2. In Static mode, bending due to surface stress change is measured and in dynamic mode shift in resonance frequency due to addition of mass is measured. Each of these modes, in turn, can be associated with different transduction scenarios, as shown figure 1.2. Analogous to contact and tapping modes of AFM, cantilever-based sensors also involve measurements of cantilever deflections, resonance frequencies and, in some cases, damping characteristics. However, the mechanisms that translate various components of a physical, chemical, or biological environment into these parameters are generally different from the mechanisms that are operative in AFM [73]. Static cantilever deflections can be caused by either external forces exerted on the cantilever (as in AFM) or intrinsic stresses generated on the cantilever surface or within the cantilever. While cantilever microfabrication technology is capable of producing nearly stress-free suspended beams, additional intrinsic stresses may subsequently originate from thermal expansion, interfacial processes

and physicochemical changes. Cantilever sensors operating in the dynamic mode are essentially mechanical oscillators, resonance characteristics of which depend upon the attached mass as well as viscoelastic properties of the medium. For instance, adsorption of analyte molecules onto a resonating cantilever results in lowering of its resonance frequency due to the increased suspended mass of the resonator.

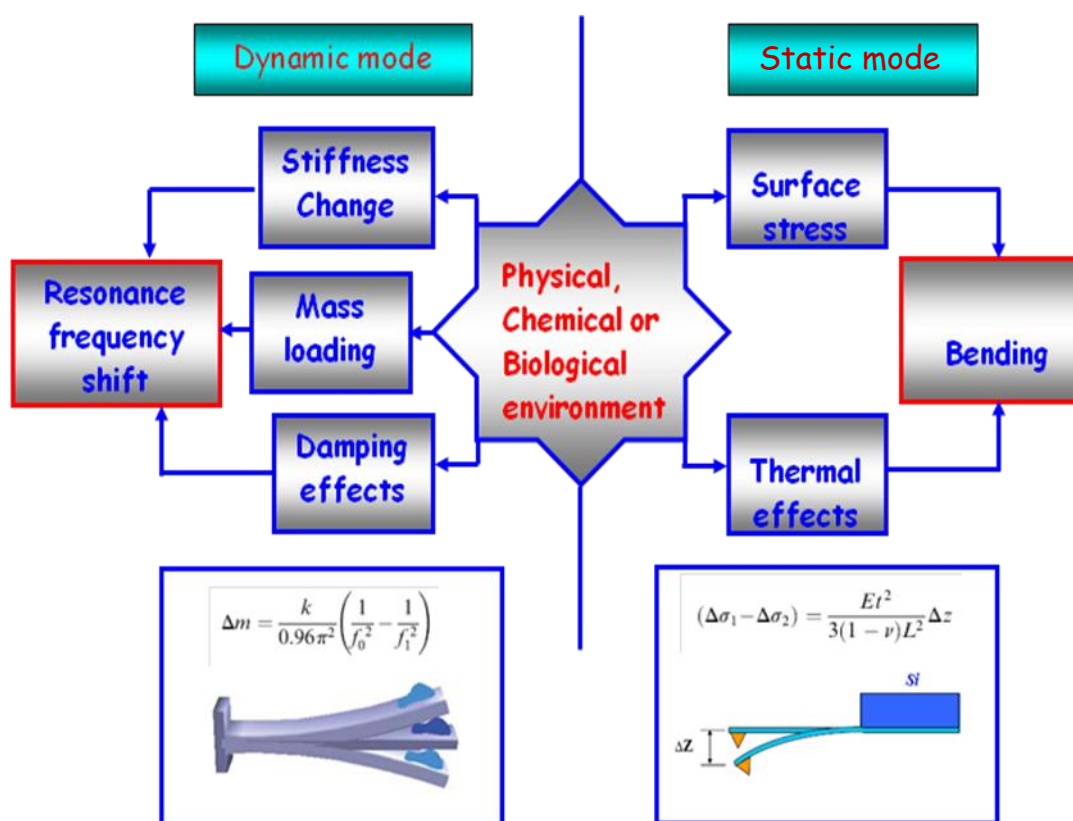


Figure 1.2 Microcantilevers are extensively studied as physical, chemical and biological sensors. These are operated in two modes, dynamic and static. In the dynamic mode, shift in resonance frequency (Δf) is measured before and after the addition of mass or environmental damping. In static mode, cantilever bending (Δz) due to differential surface stress is measured. Optical, piezoresistive, capacitance, or electron tunneling methods, are some of the known methods for detecting the cantilever vibrations or bending.

For example, when we use a cantilever with an added mass of 45 ng and a resonant frequency of 280 kHz, we obtained a mass sensitivity ($\Delta m / \Delta f$) of 320 fg / Hz. This value is 100 times greater than the sensitivity obtained with the quartz crystal microbalance method. To achieve high sensitivity in mass detection, it is necessary to use a cantilever with a small mass and a high resonant frequency. Recently systems capable of detecting masses in the zeptogram ranges have been reported [11] and the ultimate goal of single molecule detection seems to be within reach with nano cantilever based sensors.

1.4 Readout Techniques

The readout method plays an important role for detecting the mechanical state of a MC. There are various readout methods in use for MC sensors, and each method has different merits and limitations depend on any specific application. In this section we describe common readout methods.

1.4.1 Optical Lever method

The optical lever method, the most commonly used readout method of quantifying static and dynamic cantilever deflections is shown in figure 1.3. A laser beam focused on the MC tip is reflected to a position sensitive photo detector (PSD), where the reflected beam position is changed by the mechanical motion of the MC. Photodiodes, divided into two or four segments, transduce the light energy striking each segment into an electrical signal that can be compared, amplified, and displayed. Quadrant photodiodes can, in principle, measure all modes of deflection

(bending, lateral motion, and torsional) simultaneously. This optical method can detect ultra small changes in MC deflection as small as a few angstrom ($=10^{-10}$ m) and is currently the most sensitive readout method for MC sensor [74, 75]. Other advantages of the optical lever method are simplicity, linearity of response, and reliability. But some limitations of this technique are well known, i.e. interference from changes in the optical properties of the surrounding medium around the MC and nonlinear response of the photodetector. Also this technique does not scale well to a large number of MCs in an array [74, 76]. As a result, the number of MCs in an array is limited. Another limitation of the optical lever method is related to the bandwidth of PSDs, which typically on the order of several hundred kilohertz.

As the requirements of the high bandwidth become more critical in the case of smaller and stiffer cantilevers that operate in the resonant mode, alternatives to the optical lever readout were explored. More accurate high bandwidth optical measurements of cantilever deflections can be carried out using interferometric schemes. Interferometry is an optical technique where laser source illuminates the cantilever and the reflected light is either interferometrically coupled with a reference beam and detected by a charge-coupled device (CCD) used for measurements of cantilever deflections. Interferometry was revisited as MEMS readout and characterization tool more recently because of its potential for high-bandwidth high resolution mapping of nanometer scale motions of small cantilevers [77] arranged in large 2D arrays. Notably, Rugar et al. [78] used interferometry to measure sub nanometer deflections of the ultrasensitive cantilevers designed for ultrasensitive force measurements that could ultimately permit single-spin magnetic resonance microscopy.

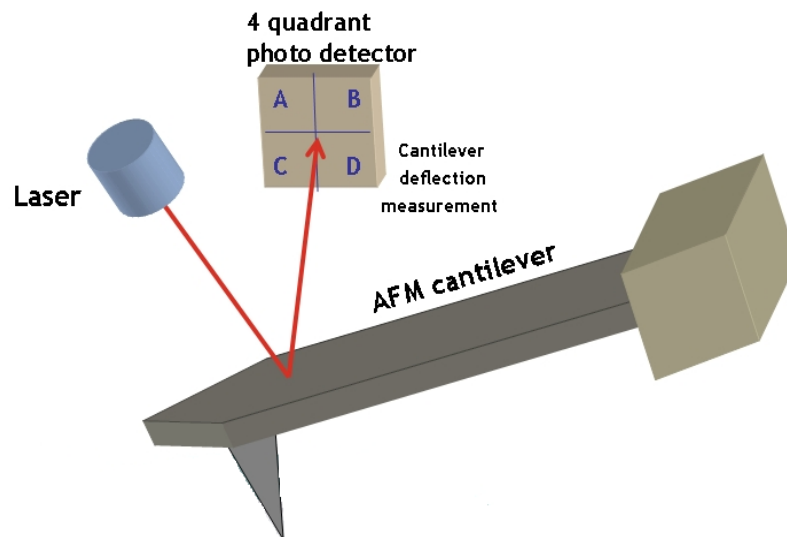


Figure 1.3 Schematic of optical readout method. The movement of the cantilever is detected by a reflected laser beam focused on cantilever and a position sensitive detector. This figure is adapted from reference [79]

1.4.2 Piezoresistive Method

Piezoresistivity is the phenomenon of changes in the bulk resistivity with applied stress. When a silicon cantilever with an appropriately shaped doped region is deformed, the change in the resistance of the doped region reflects the degree of the deformation. One of the most common materials that exhibit a strong piezoresistive effects is doped single crystal silicon [80, 81]. A piezoresistive cantilever array and a typical schematic diagram of piezoresistive detection are shown in figure 1.4. The variation in resistance is typically measured by including the cantilever into a dc-biased Wheatstone bridge. Typical resistance of a silicon MC with a boron doped channel is a few kilo Ohm. As the MC deflects, it undergoes a stress change that will create strain to the piezoresistor, thereby causing a change in resistance. When voltage V is applied to the Wheatstone bridge with resistors of identical initial

resistance R ($R_1=R_2$), the differential voltage across the bridge can be expressed as $\Delta V=V(\Delta R/4R)$. The output voltage can be acquired in a PC. The piezoresistive readout method is well-suited to measure a large number of MC arrays and to make a compact system such as a lab-on-a-chip device [80, 82]. The disadvantages of this technique are electronic, thermal and conductance fluctuation noise, nonlinear response, thermal drifts caused by temperature changes and poor sensitivity [76, 83]. Another major disadvantage of the piezoresistive technique is that it requires current to flow through the cantilever. This results in additional dissipation of heat and associated thermal drifts. When the cantilever is heated appreciably above the ambient temperature, any changes in the thermal conductivity of the environment will result in fluctuations of the cantilever temperature that, in turn, may lead to parasitic cantilever deflection and piezoresistance changes.

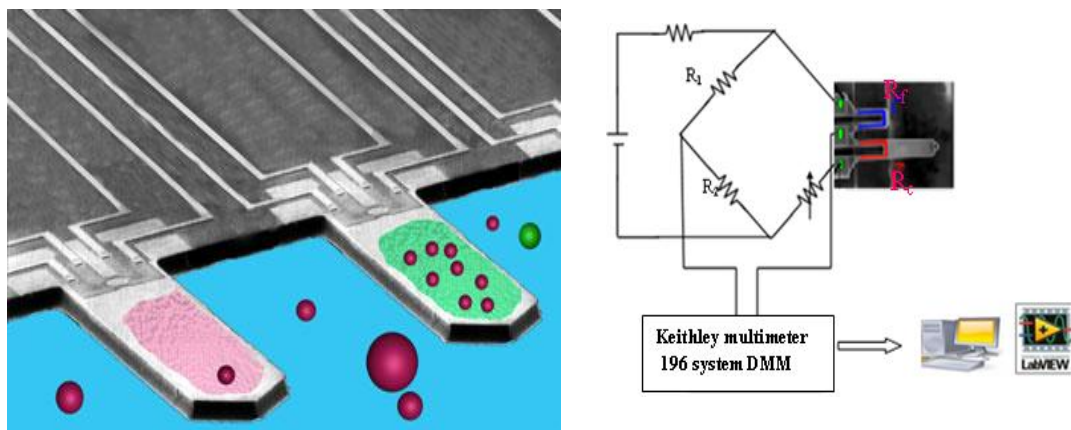


Figure 1.4 Schematic of array of Piezoresistive MC (adapted from [84]). The greatest advantage of this technique is read-out electronics can be integrated on the same silicon chip. Wheatstone bridge configuration is also shown in the figure.

1.4.3 Capacitive Method

A capacitive method is based on measuring the capacitance between an electrode on a MC and another electrode fixed on the substrate underneath the MC with a small separation [85]. Upon mechanical movement of the MC the capacitance between two electrodes changes and allows the deflection of the MC to be determined. Sensitivity of the capacitive method is dependent on the separation distance between the MC and the substrate because the capacitance is inversely proportional to the separation between two electrodes. This technique suffers from interference with changes in the effective dielectric constant of the medium around the electrodes and from stiction when parallel electrode plates are brought in too close proximity [86, 87]. As a result, the capacitive method is usually used in gaseous and not aqueous media. One of the main advantages of capacitance readout is that it can be used in integrated MEMS devices that are fully compliant with standard CMOS technology. Capacitive cantilever is mainly used for gaseous phase chemical sensing since it does not work in electrolyte solutions due to the faradic currents between the capacitive plates. For gas sensing, Amirolo and co-workers [85, 88] used capacitive detection of gaseous molecules and found the limit of detection to be 50 ppm for toluene and 10ppm for octane. Britton Jr. and co-workers demonstrated hydrogen detection using their capacitive cantilever array and the detection limit of the hydrogen was as low as 100 ppm [67].

1.4.4 Piezoelectric method

Piezoelectricity has been widely used for both cantilever actuation and for detection of cantilever deflection. Basically, a mechanical stress generates an electrical potential across a piezoelectric material and vice versa. For high resolution detection of the deflection it is necessary to operate the cantilever in the dynamic mode since the voltage produced by a static force cannot be maintained by the thin film piezoelectric material. Thus, the piezoelectric read-out is primarily utilized in resonance mode. The challenge of this technique is that most piezoelectric materials are difficult to work with and they are not all clean room compatible. The read-out has the advantage of being easily scalable and with low power consumption. It can withstand high environmental damping and it can operate in liquid. The detection scheme is all electric and the system can be easily made portable. The main disadvantage of the piezoelectric as well as piezoresistance readout is that they require electrical connections to the cantilever. An additional disadvantage of the piezoelectric technique is that in order to obtain large output signals it requires the thickness of the piezoelectric film to be well above the values that correspond to optimal mechanical characteristics.

1.5 Excitation methods

- **Piezo excitation:** In this method, MC is placed on a piezoactuator which in turn will be driven by a frequency generator.
- **Electrostatic excitation:** In this method, cantilever acts as electrode out of two electrodes. By applying an alternating voltage between the driver plate

and the cantilever, a periodic force is exerted on the cantilever, thus actuating it. This technique is very good when working in vacuum, since air would damp the motion on the resonator. Electrostatic excitation is especially attractive in combination with capacitive detection method.

- **Dielectric excitation:** It also uses two electrodes that are separated by a dielectric material, thus the whole structure is the cantilever. Here, just like with electrostatic actuation, one applies an alternating voltage between the upper and bottom layer electrodes. This voltage will pull the two layers together, thus deforming the dielectric layer causing lateral stress, which will actuate the cantilever.
- **Integrated piezoelectric excitation:** In this method a piezoelectric material, such as single-crystalline quartz is sandwiched between two metal contacts, which is then placed on a silicon cantilever. By applying an alternating voltage across the piezoelectric material, one can actuate the cantilever.
- **Resistive heating excitation:** In this method heating resistor integrated onto the cantilever. Expansion of the cantilever takes place due to the stress exerted by local rise of the temperature around the heating resistor.
- **Bimorph-effect excitation:** It is similar to the resistive heating, but the cantilever bends mostly because of the different thermal expansion coefficients of the cantilever material and the heater.

1.6 Microcantilever Theory

A cantilever is a simple beam structure in which one end is fixed and the other is free. A cantilever beam is usually subjected to loads laterally or transversely to its axis, and is commonly used in structures and machines. In order to understand the mechanical behavior of the MC as a cantilever beam, we briefly review cantilever beam theory.

The following sections describe the theory for mechanical behavior of a cantilever beam in vibration and bending modes.

1.6.1 Dynamic mode

1.6.1.1 Expression for natural frequency of cantilever beam

According to the mechanical vibration theory, after disturbing a cantilever beam, it vibrates at its natural frequency since the inertia of the beam causes it to oscillate. The governing differential equation of motion of a cantilever beam obtained using Hamilton's principle is given by [89],

$$\rho A \frac{\partial^2 u(x,t)}{\partial t^2} + EI \frac{\partial^4 u(x,t)}{\partial x^4} = f(x,t) \quad (1.1)$$

where, u is the displacement of vibration, ρ is density, A is the cross sectional area, E is the Young's modulus, I is the moment of inertia of the cantilever beam.

A cantilever beam is fixed at one end and is free on the other end so that at the fixed end both deflection and slope are zero and at the free end both shear force and bending moment are zero. This can be summarized as,

$$u = 0, \quad \frac{\partial u}{\partial x} = 0 \quad \text{for fixed end.}$$

$$\frac{\partial^2 u}{\partial x^2} = 0, \quad \frac{\partial^3 u}{\partial x^3} = 0 \quad \text{for free end} \quad (1.2)$$

As forming an initial boundary value problem, the differential equation can be solved using eigen function expansion and variable separation. In order to solve the differential equation of the motion, first we consider a homogenous problem by setting $f(x, t) = 0$. By applying variable separation with $u(x, t) = X(x)Y(t)$, where X is independent of time t and Y is independent of position x , the differential equation of motion can be separated into two ordinary differential equations,

$$\frac{d^2 Y}{dt^2} + \omega_0^2 Y(t) = 0 \quad (1.3)$$

$$\frac{d^4 X(x)}{dx^4} + \left(\frac{\lambda}{L}\right)^4 X(x) = 0 \quad (1.4)$$

Where, L is the length of the cantilever and the dimensionless parameter is λ , defined as;

$$\left(\frac{\lambda}{L}\right)^4 = \frac{\rho A}{EI} \omega_0^2 \quad (1.5)$$

Solutions of homogenous differential equations are

$$Y(t) = d_1 \sin \omega t + d_2 \cos \omega t \quad (1.6)$$

$$X(x) = c_1 \sin\left(\frac{\lambda}{L}x\right) + c_2 \cos\left(\frac{\lambda}{L}x\right) + c_3 \sinh\left(\frac{\lambda}{L}x\right) + c_4 \cosh\left(\frac{\lambda}{L}x\right) \quad (1.7)$$

By applying boundary conditions to spatial function $X(x)$, a characteristic frequency equation can be obtained as,

$$\cos \lambda \cosh \lambda + 1 = 0 \quad (1.8)$$

An unloaded freely vibrating in a bending mode in a vacuum will have a number of resonant frequencies.

The general expression of the i^{th} mode resonance of the beam, f_i is given by,

$$f_i = \frac{1}{2\pi} \left(\frac{\lambda_i}{L} \right)^2 \sqrt{\frac{EI}{\rho A}} = \frac{1}{2\pi} \left(\frac{\lambda_i}{L} \right)^2 T \sqrt{\frac{E}{12\rho}} \quad (1.9)$$

Where, n is mode number, λ_n dimensionless n^{th} mode eigenvalue, E – Young's modulus, ρ – density and h , L are thickness and length of the cantilever respectively.

Through numerical calculations, the lowest values of λ_n can be calculated as, $\lambda_1 = 1.8751$, $\lambda_2 = 4.6941$, $\lambda_3 = 7.8548$, $\lambda_4 = 10.9956$ and for $\lambda_n \gg 1$, $\lambda_n = \pi (n-1/2)$.

Equation (1.9) is commonly assimilated to a harmonic oscillator where it is assigned a spring constant (k) and effective mass (m^*)

$$f = \frac{1}{2\pi} \sqrt{\frac{k}{m^*}} \quad (1.10)$$

where, $k = \frac{ET^3W}{4L^3}$, $m^* = \frac{3m}{\lambda_n^4} = n_n m$, W and m are the width and mass of the cantilever beam and n_n is the geometrical factor for the n^{th} mode of vibration.

1.6.1.2 Higher modes vs microcantilever dimensions

For silicon cantilever with $L = 450 \mu\text{m}$ and $T = 2.5 \mu\text{m}$ first three eigenmodes in vacuum can be calculated as:

$$f_1 = \mathbf{13.463 \text{ kHz}},$$

$$f_2 = \mathbf{84.375 \text{ kHz}}, \text{ and}$$

$$f_3 = \mathbf{236.254 \text{ kHz}}.$$

Their ratios are independent on the cantilever dimensions, so that:

$$\frac{f_2}{f_1} = 6.2671, \text{ and } \frac{f_3}{f_1} = 17.548.$$

As only the first eigen frequency of a cantilever is experimentally measured, these values allow quick estimation of the higher modes position in the cantilever spectrum. It is helpful for experimental cantilever characterization, because time-consuming scan over the whole cantilever spectrum can be avoided. Figure 1.5 shows the plot of frequency with mode number of a typical MC. It is clear from figure that the frequency increases with increasing mode number.

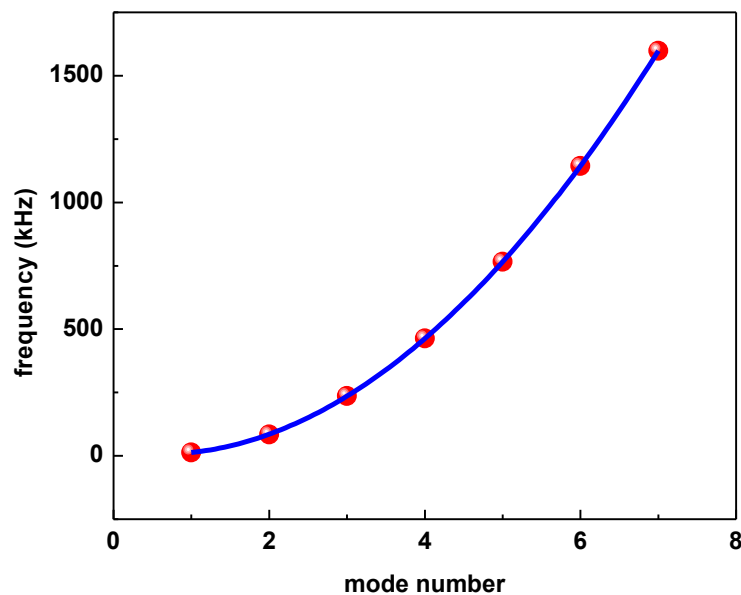


Figure 1.5 The natural frequency of MC with mode number. Frequency of MC is increasing with mode number as a function of parabola.

Similarly natural frequency of MC is dependent on its dimensions and in particular its length and thickness. Figure 1.6 shows the variation of a typical MC frequency with its length and thickness.

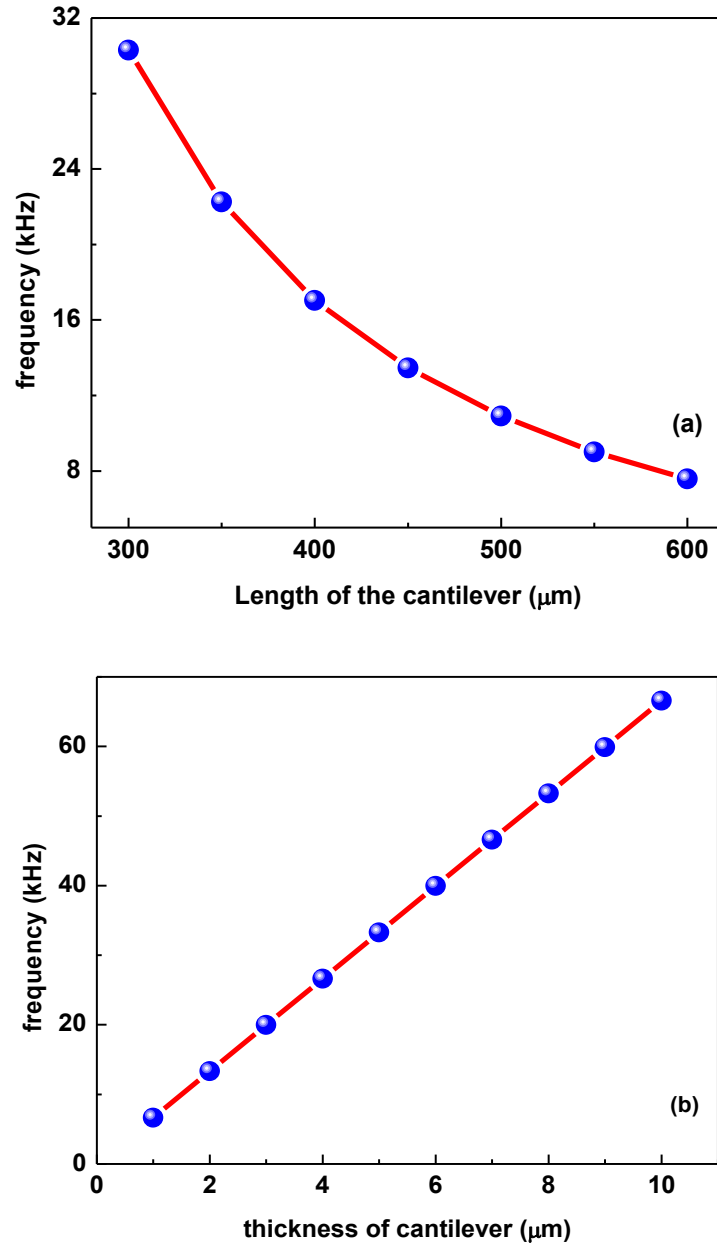


Figure 1.6 Variation of natural frequency with (a) cantilever length and (b) thickness. Frequency of MC is proportional to $1/L^2$ and thickness of MC.

It is evident from this figure that the frequency of the MC is varying as function of $1/L^2$ and it is linearly proportional to thickness T .

1.6.1.3 Mass estimation

If an additional mass Δm is added, then the resonant frequency decreases by,

$$f_2 = \frac{1}{2\pi} \sqrt{\frac{k}{m^* + \Delta m}} \quad (1.11)$$

Squaring, equation (1.10) and (1.11), we get,

$$(f_1)^2 = \frac{1}{4\pi^2} \left(\frac{k}{m^*} \right) \quad (1.12)$$

$$(f_2)^2 = \frac{1}{4\pi^2} \left(\frac{k}{m^* + \Delta m} \right) \quad (1.13)$$

Taking reciprocal of equation (1.12) & (1.13) and subtracting, we get

$$\left[\frac{1}{(f_1)^2} - \frac{1}{(f_2)^2} \right] = \frac{4\pi^2 n_n}{k} (-\Delta m)$$

where n_n is the geometrical factor for the n th mode of vibration.

Rearranging,

$$\Delta m = \frac{-k}{4\pi^2 n_n} \left[\frac{1}{(f_1)^2} - \frac{1}{(f_2)^2} \right] \quad (1.14)$$

This expression gives the value of additional mass on the cantilever.

Case1: When added mass is at the beam apex

If the added mass is much smaller than the mass of the cantilever beam and it is concentrated (Δm_{conc}) at the beam apex (e.g. functionalization pad is deposited near the cantilever apex), the total eigenmode-dependent effective mass of the oscillator is supposed to be:

$$(m^*)_n = n_n \rho \text{TWL} + \Delta m_{\text{conc}} \quad (1.15)$$

Then the corresponding eigenfrequency will be defined by

$$f_n^{\Delta m_{conc}} = \frac{1}{2\pi} \sqrt{\frac{k}{n_n \rho WTL + \Delta m_{conc}}} \quad (1.16)$$

By measuring the resonance frequencies before and after the mass change, the concentrated mass is then given by

$$\Delta m_{conc} = \frac{k}{4\pi^2} \left[\frac{1}{(f_n^{\Delta m_{conc}})^2} - \frac{1}{(f_n^o)^2} \right] \quad (1.17)$$

Eq (1.17) suggests that the minimum detectable mass of the cantilever is directly proportional to the spring constant and inversely proportional to the difference of the resonance frequency squared, before and after the mass change.

Case2: When added mass is uniformly distributed on the cantilever beam

In the case of uniformly distributed mass (Δm_{distr}), the effective modal mass can be approximated as:

$$(m^*)_n = n_n(\rho TWL + \Delta m_{distr}) \quad (1.18)$$

Eigenfrequencies of the cantilever loaded with a distributed mass in the absence of damping can be approximated as:

$$f_n^{\Delta m_{distr}} = \frac{1}{2\pi} \sqrt{\frac{k}{n_n \rho WTL + n_n \Delta m_{distr}}} \quad (1.19)$$

A total amount of the distributed mass, which influence on the elasticity of the cantilever, can be calculated according to:

$$\Delta m_{distr} = \frac{k}{4\pi^2 n_n} \left[\frac{1}{(f_n^{\Delta m_{distr}})^2} - \frac{1}{(f_n^o)^2} \right] \quad (1.20)$$

In the present work, mass sensitivities of MC when working at higher modes and reducing dimensions (i.e working at fundamental mode) are compared.

1.6.1.4 Factors effecting mass sensitivity

Mass sensitivity of MCs is influenced either due to variations in effective mass or resonance frequency instability. The former is dictated by the material and geometry of the resonator and the later is governed by fluctuations of quantum nature. It is shown that better mass sensitivity can be attained with lower effective mass of the resonator i.e. by reducing the dimensions of MC. However, in the case of nano cantilevers, there are other factors like thermomechanical, temperature fluctuations, adsorption-desorption and momentum exchange noises influence the mass sensitivity [1,7]. Sensing of single atoms would be hardly resolvable without device optimization to diminish intrinsic noise influence. Piezo-resistive cantilevers are much more susceptible to the read-out unit noises, such as Johnson noise and $1/f$ noise. $1/f$ noise can be neglected by operating the cantilever in dynamic mode at frequencies higher than 10 kHz. In its own turn, Johnson noise has the highest impact.

1.6.1.5 Q factor of microcantilevers

Q-factor is commonly used to quantify energy dissipation in MCs. The Q-factor is frequently used to characterize the degree of the resonance peak sharpness. This means that a large and sharp resonance peak denotes a high Q-factor. This signifies the importance of the Q-factor for chemical sensors, since a sharp resonance peak is needed to accurately measure a resonance frequency change for monitoring the sorption process. Q factor can be practically determined as resonance frequency f_{res} , which corresponds to the maximum oscillation amplitude A_{max} divided by the bandwidth Δf_{-3dB} determined at the $-3dB$ amplitude level $A_{max}/\sqrt{2}$.

Q-factor of MCs is mainly affected by:

- Viscous and acoustic damping, Q_a ;
- Clamping (or support) loss, Q_s ;
- Internal material loss, Q_i

The total Q-factor can be related to the individual energy dissipation sources by [12, 15]:

$$\frac{1}{Q_{tot}} = \frac{1}{Q_a} + \frac{1}{Q_s} + \frac{1}{Q_i}$$

Usually the lowest Q-factor, which determines the total Q-factor in the above equation is the one limited by viscous and acoustic damping Q_a . This means that the pressure and atmosphere in the vicinity of the cantilever has a large influence on the total Q-factor, and the Q-factor increases as the total ambient pressure decreases [15]. Clamping loss Q_s (to the chip substrate through the cantilever support) has an insignificant contribution to the total dissipation in the case of longer MC with high length-to-width and width-to-thickness ratios. Damping due to internal material parameters Q_i , such as crystal structure, lattice defects, etc. comprise internal material loss, Q_i .

1.6.2 Static mode

Static mode indicates static deflection such that a rectangular cantilever beam is bent under the action of applied forces on the axis of the straight beam.

The deflection (u) of the beam at the end is the displacement of the tip from the x -axis in the y -direction. The geometry is shown in figure 1.7.

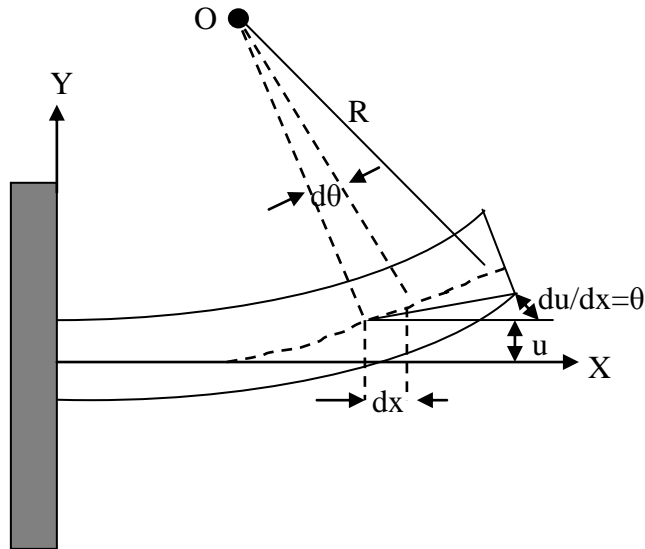


Figure 1.7 Schematic of cantilever beam deflection. The radius of curvature R is derived as a function of deflection of the beam.

The deflection of the curvature ζ at a distance x from the y axis is expressed as [89]

$$\zeta = \frac{1}{R} = \frac{\frac{d^2u}{dx^2}}{\left[1 + \left(\frac{du}{dx}\right)^2\right]^{3/2}} \quad (1.21)$$

where R is the radius of curvature.

The square of the slope, $(du/dx)^2$, may be negligible relative to unity since the assumption of the beam theory is the deflection of the beam is small compared with the length of the beam. Hence Equation 1.21 can be expressed as

$$\zeta = \frac{1}{R} = \frac{d^2u}{dx^2} \quad (1.22)$$

The curvature represents the rate at which the slope varies along the axis of the beam.

There is a neutral axis of the cross section of the rectangular beam which is located

at zero strain or stress. According to Hook's law of elasticity, the stress and strain relationship is denoted as

$$\sigma = \varepsilon E \quad (1.23)$$

Where σ is normal stress, ε is strain, and E is Young's modulus. The concept of stress is a measure of the internal forces in the unit area reacting to external forces.

When the bending moment is loaded onto a cantilever beam, it causes compression on one surface area and tension on the other. From the linear bending moment-curvature relationship, we can obtain

$$\zeta = \frac{1}{R} = \frac{M}{EI} \quad (1.24)$$

Where M is a bending moment, E is Young's modulus, and the moment of inertia I of the cross section about the centroid axis is defined as $I = \int y^2 dA$. The moment of inertia I for a rectangular cantilever beam is given by

$$I = \frac{WT^3}{12} \quad (1.25)$$

Where W is width and T is thickness shown in figure 1.8.

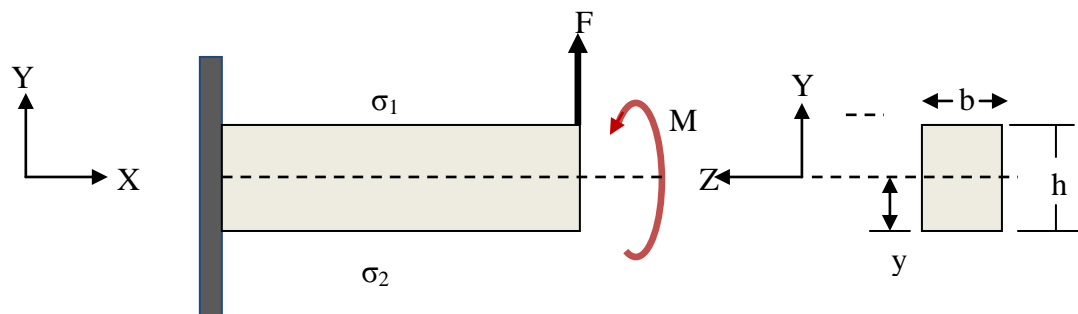


Figure 1.8 Cantilever beam geometry and bending moment diagram. σ_1 and σ_2 stresses in upper and lower surface of the beam respectively. M is the bending moment induced in the cantilever beam

To obtain a differential equation for the deflection curve, the Equations 1.22 and 1.24 are combined,

$$\zeta = \frac{1}{R} = \frac{d^2u}{dx^2} = \frac{M}{EI} \quad (1.26)$$

Solving Equation 1.26, the deflection angle and deflection can be expressed as

$$\begin{aligned} \theta &= \frac{Mx}{EI} \\ \delta &= \frac{Mx^2}{2EI} \end{aligned} \quad (1.27)$$

The maximum deflection angle and the maximum deflection at the free end of the cantilever beam due to the moment M can be calculated by substituting the length of the cantilever beam, L, into x with the results given by

$$\begin{aligned} \theta_{\max} &= \frac{ML}{EI} \\ \delta_{\max} &= \frac{ML^2}{2EI} \end{aligned} \quad (1.28)$$

Let's now consider a cantilever beam coated with a thin film on one surface. If the thin film is made of a different material from that of the cantilever, their mechanical properties and responses to stimuli will be different. As a result of the difference between the upper and lower stresses, σ_1 and σ_2 respectively, in the cantilever beam, a bending moment is induced which is described by

$$M = \frac{WT}{2} \Delta\sigma \quad (1.29)$$

where $\Delta\sigma = \sigma_1 - \sigma_2$ is the stress difference.

Inserting Equation 1.29 into 1.26, we can obtain one form of Stoney's formula: [90]

$$\frac{1}{R} = \frac{WT\Delta\sigma}{2EI} = \frac{6\Delta\sigma}{ET^2} \quad (1.30)$$

Stoney's formula has been modified by substituting E with $E/(1-\nu)$ since surface stress is isotropic in all directions in the film which is assumed to be isotropic [91].

Hence Equation 1.30 becomes

$$\frac{1}{R} = \frac{6\Delta\sigma}{E(1-\nu)T^2} \quad (1.31)$$

where ν is Poisson's ratio.

Deflection of the cantilever (u or Δz) is given by

$$\Delta z = \frac{L^2}{2R} \quad (1.32)$$

Combining Eqs. 1.31 and 1.32 gives

$$\Delta z = \frac{3L^2}{E(1-\nu)T^2} \Delta\sigma \quad (1.33)$$

This modified Stoney's formula is used to calculate the surface stress. From here it is seen that the deflection can be optimized by decreasing the thickness and increasing the length of the MC.

Stress changes in a thin film coated on the surface of a cantilever are illustrated in figure 1.9. In figure 1.9(a) the cantilever bends downwards and expands until the stress thus created in the cantilever balances the stress in the thin film on top. The stress in the film is compressive as the expansion is hindered by the supporting cantilever. The stress on the top side of the supporting cantilever is tensile. In the case of a contracting film the cantilever bends upwards and the stress in the thin film is said to be tensile (figure 1.9(b)).

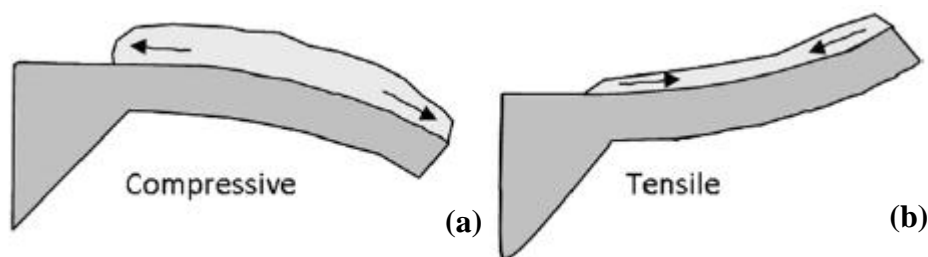


Figure 1.9 Stress in a thin film on a cantilever. (a) As the film expands the cantilever bends down. The resulting stress in the film is compressive as its expansion is hindered and balanced by the bending of the cantilever. (b) For a contracting film the cantilever bends up and the resulting stress in the film is tensile. This figure is adapted from reference [1]

The bending of MC has been a subject of study in the context of evolution of fundamental material parameters such as surface stress, adsorption on exposure to analytes etc [92, 93]. These experiments hinge strongly on the basis of Stoney's equation, where the bending of the MC is associated with the magnitude of change in surface stress [69, 94]. It is known that the bending response of a MC is greatly enhanced by passivating a layer [16] or by tailoring the surface topology [94]. One specific interest is the role of surface morphology on the MC deflection sensitivity. Lavrik et al [94] compared the deflection sensitivity of MCs with different surface roughness and concluded that it enhances when surface roughness increases. However, Godin et al [95] found that MC with rough surface deflects less compared to smooth surface and attributed it to the formation of incomplete mono layers during molecular adsorption. In a similar study, Desikan et al [96] did not observe any significant increase in surface stress and thus deflection of MC due to increase in surface roughness. In the present thesis, dependence of MC bending on roughness of MC surface is investigated and is presented in chapter 4.

1.7 Objectives of the present thesis

The objective of the present thesis is to study various methods to enhance the sensitivity of the cantilever based mass sensors and some fundamental aspects associated with MCs like adsorption induced stiffness changes, etc.

The specific objectives are:

To,

1. Detect the higher mode frequencies and shapes experimentally using AFM, Nano Vibration Analyzer (NVA) and compare with FEM simulations.
2. Compare experimentally the mass sensitivities of MC based mass sensors by working at higher modes and reducing dimensions.
3. Perform FEM simulations to study the various possible ways to enhance the sensitivity of nano cantilever based mass sensors by attaching various nanostructures.
4. Indigenously develop a precise dip coating setup for coating the MCs with the required polymer solution and to explore the possibility of using polymer coated MCs for gamma radiation detection.
5. Study the residual stress in uncoated MCs using Micro-Raman spectroscopy.
6. Address the adsorption induced stiffness changes in MC and its dependences on MC dimensions.
7. Study the possible mechanisms responsible for deflection of uncoated MC and to use it as an effective humidity sensor.

1.8 References

1. A. Boisen, S. Dohn, S. S. Keller, S. Schmid and M. Tenje, *Rep. Prog. Phys.* 74, (2011) p. 03610.
2. K.R. Buchapudi, Xin Huang, Xin Yang, Hai-Feng Ji and T. Thundat, *Analyst* 136, (2011) p.1539-1556
3. K.M. Hansen and T.Thundat, *Methods.* 37, (2005) p. 57-64
4. N. V. Lavrik, M. J. Sepaniak and P. G. Datskos, *Rev. Sci. Instrum.* 75, (2004) p.2229
5. Z. J. Davis, W. Svendsen and A. Boisen, *Micro Elec. Eng.* 84, (2007) p.1601
6. S. Hosaka, T. Chiyoma, A. Ikeuchi, H. Okano, H. Sone and T. Izumi, *Curr. Appl. Phys.* 6, (2006) p.384
7. M. K. Ghatkesar, V. Barwich, T. Braun, J.P. Ramseyer, C. Gerber, M. Hegner, H. P. Lang, U. Drechsler and M. Despont, *Nanotechnology* 18, (2007) p.445502
8. M. A. Spletzer, A. Raman, H. Sumali and J. P. Sullivan, *Appl. Phys. Lett.* 92, (2008) p.114102
9. B. Ilic, H. G. Craighead, S. Krylov, W. Senaratne, C. Ober and P. Neuzil, *J. Appl. Phys.* 95, (2004) p.3694
10. Y. T. Yang, C. Callegari, X. L. Feng, K. L. Ekinici and M. L. Roukes, *Nano Lett.* 6, (2006) p.583
11. M. Li, H. X. Tang and M. L. Roukes, *Nature Nanotechnol.* 2, (2006)p. 114
12. F. Lochon, I. Dufour and D. Rebiere, *Sensor Actuator B* 108, (2005)p. 979
13. S. Dohn, Cantilever based mass sensing alternative readout and operation schemes, Ph.D. thesis, Technical University of Denmark (2006)
14. H. Xie, J. Vitard, S. Haliyo and S. R'egnier, *Meas. Sci. Technol.* 19, (2008) p.055207
15. R. Sandberg, K. Mølhave, A. Boisen and W. Svendsen, *J. Micromech. Microeng.* 15, (2005) p.2249
16. G.Y. Chen, T. Thundat, E.A. Wachter and R.J. Warmack, *J. Appl. Phys.* 77, (1995) p.3618-3622
17. S. Cherian and T. Thundat, *Appl. Phys. Lett.* 80, (2002) p.2219-2221
18. J.H. Lee, T.S. Kim, and K.H. Yoon, *Appl. Phys. Lett.* 84, (2004) p.3187

19. K.S. Hwang, K. Eom, J.H. Lee, D.W. Chun, B.H. Cha, D.S. Yoon, T.S. Kim and J.H. Park, *Appl. Phys. Lett.* 89, (2006) p.173905
20. J. Lagowski, H.C. Gatos and E.S. Sproles, Jr., *Appl. Phys. Lett.* 26, (1975) p.493
21. R. B. Karabalin, L. G. Villanueva, M. H. Matheny, J. E. Sader and M. L. Roukes, *Phys. Rev. Lett.* 108, (2012) p.236101
22. L.Feng, F. Gao, M.Lie, S.Wang, L.Li, M.Shen and Z.Wang, *J. Appl. Phys.* 112, (2012) p.013501
23. X. Yi, H.L Duan, *J. Mech. & Phys. Soild.* 57, (2009) p.1254-66
24. P. Lu, H. P. Lee, C. Lu, and S. J. O’Shea, *Phys. Rev. B* 72, (2005) p.085405
25. M. J. Lachut and J. E. Sader, *Phys. Rev. Lett.* 99, (2007)p. 206102 :
M.J.Lachut and J.E.Sader, *Phys.Rev.B* 85, (2012) p.085440
26. B.N. Johnson and Raj Mutharasan, *Biosensors and Bioelectronics* 32, (2012) p.1-18
27. G. Binnig, C.F. Quate and C. Gerber, *Phys. Rev. Lett.* 56, (1986)p. 930
28. T. Thundat, R.J. Warmack, G.Y. Chen and D.P. Allison, *Appl. Phys. Lett.* 64, (1994) p.2894
29. E.A. Wachter, T. Thundat, *Rev. Sci. Instrum.* 66, (1995) p.3662–3671
30. T. Thundat, E.A. Wachter, S.L. Sharp, R.J. Warmack, *Appl. Phys. Lett.* 66, (1995) p.1695–1697
31. T. Thundat, G.Y. Chen, R.J. Warmack, D.P. Allison, E.A. Wachter, *Anal. Chem.* 67, (1995)p. 519–521
32. J.R. Barnes, R.J. Stephenson, C.N. Woodburn, S.J. O’Shea, M.E. Welland, T. Rayment, J.K. Gimzewski and C. Gerber, *Rev. Sci. Instrum.* 65, (1994) p.3793
33. J.R. Barnes, R.J. Stephenson, M.E. Welland, C. Gerber and J.K. Gimzewski, *Nature* 372, (1994) p.79
34. R. Raiteri and H.J Butt, *J. Phys. Chem.* 99, (1995) p.15728
35. H.J Butt, *J. Colloid Interface Sci.* 180, (1996) p.251
36. R. Berger, E. Delamarche, H.P. Lang, C. Gerber, J.K. Gimzewski, E. Meyer and H.J. Guntherodt, *Science* 276, (1997) p.2021
37. P.G. Datskos, I. Sauers, *Sens. Actuators, B* 61, (1999) p.75–82

38. Y.J. Tang, J. Fang, Xi. Xu, Hai-Feng Ji, G.M. Brown and T. Thundat, *Anal. Chem.* 76, (2004) p.2478-2481
39. J. Mertens, E. Finot, M.H. Nadal, V. Eyraud, O. Heintz and E. Bourillot, *Sens. Actuators B.* 99, (2004) p.58-65
40. X.D. Yan, Y.J. Tang, Haifeng Ji, Y. Lvov and T. Thundat, *Instrumentation Science & Technology* 32, (2004) p.175-183
41. M. Alvarez, L.G. Carrascosa, M. Moreno, A. Calle, A. Zaballos, L.M. Lechuga, C. Martinez-A and J. Tamayo, *Langmuir* 20, (2004) p.9663-9668
42. B. Monchev, D. Filenko, N. Nikolov, C. Popov, T. Ivanov, P. Petkov and I.W. Rangelow, *Appl. Phys. A* 87, (2007) p.31-36
43. D. Filenko and I.W. Rangelow, *Nano-electronic sensor elements for chemical recognition systems.* 2004, Kassel, 91B1.
44. N. Abedinov, P. Grabiec, T. Gotszalk, Tz. Ivanov, J. Voigt and I.W. Rangelow, *J. Vac. Sci. Technol. A* 19, (2001)p. 2884
45. L.M. Zambov, C. Popov, N. Abedinov, M.F. Plass, W. Kulisch, T. Gotszalk, P. Grabiec, I.W. Rangelow and R. Kassing, *Advanced Materials* 12, (2000) p.656-660
46. K. Yum, Z. Wang, A.P. Suryavanshi and M.F. Yu, *J. Appl. Phys.* 96, (2004) p.3933-3938
47. A. Kooser, R.L. Gunter, W.D. Delinger, T.L. Porter and M.P. Eastman, *Sens. Actuators B* 99, (2004) p.474-479
48. L. Fadel, F. Lochon, I. Dufour and O. Francais, *J. Micromech. Microeng.* 14, (2004) p.S23- S30
49. J.H. Pei, F. Tian and T. Thundat, *Anal. Chem.* 76, (2004) p.292-297
50. X.D. Yan, H.F. Ji and Y. Lvov, *Chem. Phys. Lett.* 396, (2004) p.34-37
51. Y.F. Zhang, S.P. Venkatachalan, H. Xu, Xi. Xu, P. Joshi, H.F. Ji and M. Schulte, *Biosens. Bioelectron.* 19, (2004) p.1473-1478
52. J.H. Lee, K.H. Yoon, K.S. Hwang, J. Park, S. Ahn and T.S. Kim, *Biosens. Bioelectron.* 20, (2004) p.269-275
53. J. Yinon, *Anal. Chem.* 75, (2003) p.99A-105A

54. L.A. Pinnaduwege, T. Thundat, J.E. Hawk, D.L. Hedden, P.F. Britt, E.J. Houser, S. Stepnowski, R.A. McGill and D. Bubb, *Sens. Actuators B* 99, (2004) p.223-229
55. L.A. Pinnaduwege, A. Wig, D.L. Hedden, A. Gehl and D. Yi, *J. Appl. Phys.* 95, (2004) p.5871-5875
56. J. Zhang and H.F. Ji, *Anal. Sci.* 20, (2004) p.585-587
57. K.Y. Gfeller, N. Nugaeva and M. Hegner, *Biosens Bioelectron.* 21, (2005) p.528-533
58. K. Liu and H.F. Ji, *Anal. Sci.* 20, 2004.
59. Y.F. Zhang, H.F. Ji, D. Snow, R. Sterling and G.M. Brown, *Instrumentation Science & Technology.* 32, (2004) p.361-369
60. F. Tian, J.H. Pei, D.L. Hedden, G.M. Brown and T. Thundat, *Ultramicroscopy.* 100, (2004) p.217-223
61. T. Boltshauser, M. Schonholzer, O. Brand and H. Baltes, *J. Micromech. Microeng.* 2, (1992) p.205-207
62. A. Hierlemann, D. Lange, C. Hagleitner, N. Kerness, A. Koll, O. Brand and H. Baltes, *Sens. Actuators B.* 70, (2000) p.2-11
63. M. Maute, S. Raible, F.E. Prins, D.P. Kern, H. Ulmer, U. Weimar and W. Gopel, *Sens. Actuators B.* 58, (1999) p.505-511
64. D. Lange, C. Hagleitner, O. Brand and H. Baltes, Digest of Technical Papers TRANSDUCERS, Sendai, Japan 1020-1023 (1999)
65. D. Lange, A. Koll, O. Brand and H. Baltes, *Proc. SPIE.* 3224, (1998)p. 233-243
66. D. Lange, C. Hagleitner, O. Brand and H. Baltes, Proc. IEEE MEMS, Myazaki, Japan, (2000) p.547-552
67. C.L Britton Jr, R.L. Jones, P.I. Oden, Z. Hu, R.J. Warmack, S.F. Smith, W.L. Bryan and J.M. Rochelle, *Ultramicroscopy.* 82, (2000) p.17-21
68. S.K. Vashist, *Journal of Nanotechnology Online*, 2007
69. J. Fritz, M.K. Baller, H.P. Lang, H. Rothuizen, P. Vettiger, E. Meyer, H.J. Guntherodt, Ch. Gerber and J.K. Gimzewski, *Science* 288, (2000) p.316-318
70. J.K. Gimzewski, Ch. Gerber, E. Meyer and R.R. Schlittler, *Chem. Phys. Lett.* 217, (1994) p.589-594

71. H. Baltes, D. Lange and A. Koll, *IEEE Spectrum* 9, (1998) p.35-38
72. L.B. Sharos, A. Raman, S. Crittenden and R. Reifenberger, *Appl. Phys. Lett.* 84, (2004) p.4638-4640
73. R. Pedrak, Tzv. Ivanov, K. Ivanova, T. Gotszalk, N. Abedinov, I.W. Rangelow, K. Edinger, E. Tomerov, T. Schenkel and P. Hudek, *J. Vac. Sci. Technol. B.* 21, (2003) p.3102-3107
74. L.G. Carrascosa, M. Moreno, M. Alarez and L.M. Lechuga, *TrAC Trends in Anal. Chem.* 25, (2006) p.196-206
75. M. Nordstrom, D.A. Zauner, M. Calleja, J. Hubner, and A. Boisen, *Appl. Phys. Lett.* 91, (2007) p.103512-103513
76. G. Shekhawat, S.H. Tark, and V.P. Dravid, *Science.* 1122588 (2006)
77. H. J. Mamin and D. Rugar, *Appl. Phys. Lett.* 79, (2001) p.3358
78. D. Rugar, C. S. Yannoni, and J. A. Sidles, *Nature (London)* 360, (1992) p.563
79. en.wikipedia.org/wiki/Portal:Nanotechnology/selected_article
80. M. Tortonese, R. C. Barrett, and C. F. Quate, *Appl. Phys. Lett.* 62, (1993) p.834
81. P. I. Oden, P. G. Datskos, T. Thundat, and R. J. Warmack, *Appl. Phys. Lett.* 69, (1996) p.3277
82. P.A. Rasmussen, J. Thaysen, O. Hansen, S.C. Eriksen, and A. Boisen, *Ultramicroscopy* 97, (2003) p.371-376
83. J. Thaysen, A. Boisen, O. Hansen, and S. Bouwstra, *Sens. Actuators A* 83, (2000) p.47-53
84. D. Filenko, "Chemical gas sensors based on functionalized self-actuated Piezo-resistive cantilevers" Ph.D. Thesis 2008.
85. J. Amirola, A. Rodriguez, L. Castaner, J.P. Santos, J. Gutierrez, and M.C. Horrillo, *Sens. Actuators B.* 111-112, (2005) p.247-253
86. R. Raiteri, M. Grattarola, and R. Berger, *Materials Today* 5, (2002) p. 22-29
87. K.M. goeders, J.S. Colton, and L.A. Bottomley, *Chem. Reviews* 108, (2008) p.522-542
88. Amirola, J., A. Rodriquez, and L. Castaner. in *Smart Sensor, Actuator, and MEMS.* 2003. Maspalomas, Gran canaria, Spain: SPIE.

89. S.S.Rao, *Mechanical vibrations*, fourth edition, pearson education
90. C. Ziegler, *Anal.Bioanal.Chem.* 379, (2004) p.946-959
91. R.J.Jacodine and W.A.Schlegel, *J. Appl. Phys.* 37, (1966) p.2429-2434
92. H. Ibach, *Surf. Sci. Rep.* 29, (1997)p. 195
93. N. Vasiljevic, T. Trimble, N. Dimitrov and K. Sieradzki, *Langmuir* 20, (2004)p.6639
94. N.V. Lavrik, C.A. Tipple, M.J. Sepaniak, P.G. Datskos, *Chem. Phys. Lett.* 336, (2001)p. 371
95. M. Godin, P. J. Williams, V. Tabard-Cossa, O. Laroche, L. Y. Beaulieu, R. B. Lennox, and P. Grutter, *Langmuir* 20, (2004) p.7090–7096
96. R. Desikan, I. Lee, and T. Thundat, *Ultramicroscopy* 106, (2006)p.795–799

Chapter 2 - Experimental Techniques

In this chapter, details of microcantilevers (MCs) used in the present work are given. Handling and cleaning of the MCs are discussed initially. Various experimental setups developed to detect the MC deflection and resonance frequency using Atomic force microscopy (AFM) head and Nano vibration analyzer (NVA) are detailed. This includes an environmental chamber used for water adsorption / desorption studies and the setup used for mapping the mode shape of MCs using NVA. Apart from this, the details about the synthesis of polymer solutions and the indigenously designed dip coating setup using three-axis micromanipulators are presented. Preliminary studies undertaken for identification of higher modes of MCs using AFM, NVA and FEM simulation are given. This chapter ends with the details of micro-Raman spectroscopy used for measuring residual stress in MCs.

2.1 Microcantilevers used in the present work

Four different MCs used in the present thesis are from commercial sources [1] and is made of single crystal n-type silicon with antimony doping. The MCs are labeled as MC1, MC2, MC3 and MC4 whose dimensions, natural frequencies and spring constant (k) values are shown in Table 2.1. MC4 is an array of cantilevers consisting of two MCs with each having the dimensions as shown. Resonance frequency of these MCs was measured using AFM head and NVA (discussed later in this chapter). The spring constant (k) is estimated using the resonance frequency and quality factor values, using Sader's method [2]. The equation used for estimation of spring

constant (k) is given by $k = 0.1906\rho_f W^2 L Q_f \Gamma_i(\omega_f)\omega_f^2$ where ρ_f is the density of the fluid (medium in which the MC exist), Q_f is the quality factor of fundamental mode of MC, W and L are the width and length of the MC, Γ is hydrodynamic function and ω_f is the fundamental resonant frequency in fluid. A typical scanning electron microscope (SEM) image and surface morphology of the MC used in this study is shown in Fig 2.1. The average roughness was estimated to be 0.85 nm on front side of MC.

Table 2.1 Details of four different microcantilevers used in the present study. The natural frequency was measured using AFM head and spring constant values are estimated using Sader's method [2].

Name	Dimensions			Resonance frequency (f) (kHz)	Spring constant (k) (N/m)
	Length (L) (μm)	Width (W) (μm)	Thickness (T) (μm)		
MC1	450	40	2.5	12.101	0.121
MC2	225	30	3	66.85	2.5
MC3	125	35	4.5	332.19	28.6
MC4	500	98	1	3-4	0.023

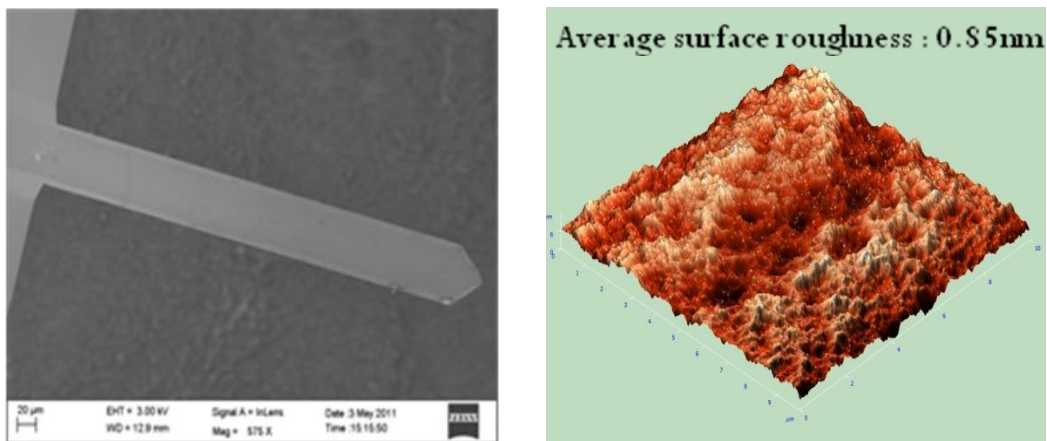


Figure 2.1 SEM and AFM images of MC1 used in this study. Average roughness of MC1 is about 0.85nm

2.2 Handling and *Piranha* cleaning of the microcantilevers

Commercially, MCs are shipped in gel pack boxes as shown in figure 2.2 (a) in order to avoid moisture environment. Generally it is very difficult to handle these MCs. Usually MCs are attached to a small substrate wafer. Using a tweezer, one can hold the substrate chip and can move around it, as shown in figure 2.2 (b).

It is reported that a common shipping and packaging material like poly(dimethylsiloxane) (PDMS), causes a thin layer of silicone oil contamination on AFM cantilever tips [3]. Thin layers of contaminants may change the reactivity or adsorptivity of surfaces so that the desired modifications may not really be carried out on surfaces [3]. It is known that *Piranha* cleaning removes the organic contamination on MCs and a native oxide of about 5nm is grown [4]. *Piranha* solution, also known as *Piranha* etch, is a 3 :1 mixture of sulfuric acid (H_2SO_4) and hydrogen peroxide (H_2O_2) used to clean organic residues off substrates. Because the mixture is a strong oxidizing agent, it will remove most organic matter, and it will also hydroxylate most surfaces (add OH groups), making them highly hydrophilic (water compatible).

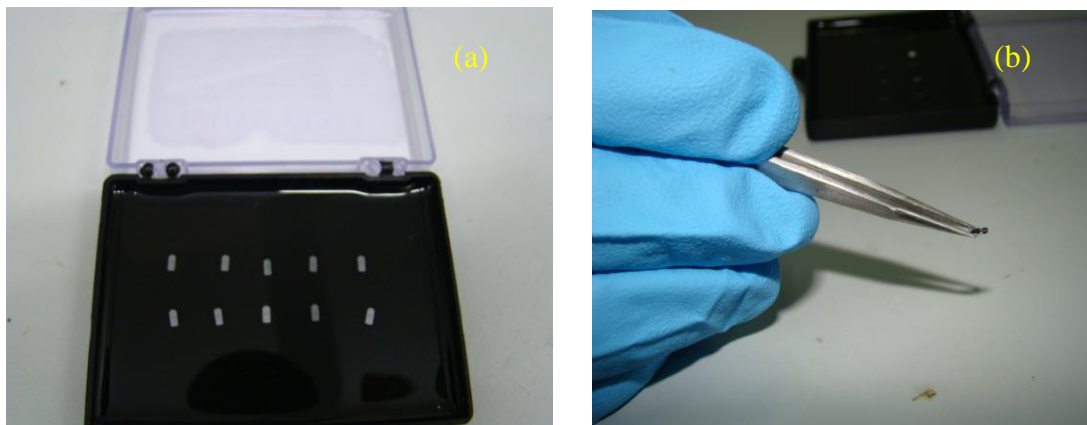


Figure 2.2 (a) Commercially available gel pack box in which usually MCs are shipped (b) handling of the MCs using a tweezer.

In the present work, MCs were cleaned using a *Piranha* solution for 30 minutes and then rinsed immediately in triply distilled water for five minutes and finally dried in nitrogen. MCs were loaded into the experimental chamber immediately after *Piranha* cleaning. Contact angle measurements were performed using a standard contact-angle goniometer (M/s HOLMARC, HO-IAD-CAM-01, India) on MC chip before and after *Piranha* cleaning. Contact angle measurements were performed using a standard contact-angle goniometer (M/s HOLMARC, HO-IAD-CAM-01, India) on MC chip before and after *Piranha* cleaning and are shown in figure 2.3. The contact angle was found to reduce from 95° to $\sim 29^\circ$ after *Piranha* cleaning. It is clear from this observation that *Piranha* cleaning makes the silicon surface hydrophilic.

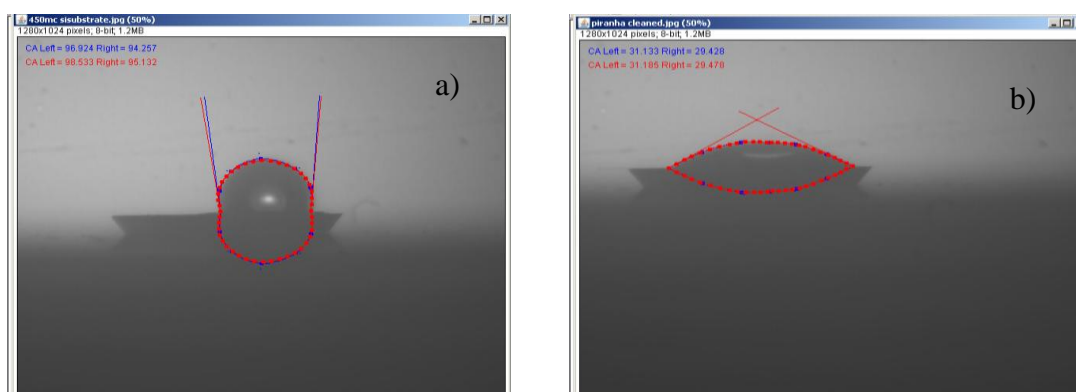


Figure 2.3 Contact angle measurements on a) before and b) after *Piranha* cleaning of MCs. The contact angle was found to reduce from 95° to $\sim 29^\circ$ after *Piranha* cleaning.

2.3 AFM head

Static and dynamic measurements on MCs are performed using the laser photodiode arrangement of an AFM head (NT-MDT, Russia). Figure 2.4 shows the photograph of AFM head used and the schematic of measurement panel. This head consists of a laser ($\lambda = 650$ nm) beam which is focused on the MC and reflected back on a four quadrant photo diode (ABCD). MC was placed on a piezo actuator which is swept using a lock-in-amplifier. The laser beam of the AFM head is

reflected from the oscillating probe in the vertical direction. These oscillations of the probe result in oscillations of the laser beam spot with respect to the top and bottom halves of the photodiode. This induces a variable electrical signal, at the probe oscillation frequency, at the output of the registration system. The amplitude of this signal is proportional to the oscillation amplitude of the probe. Therefore the registration system measures the probe oscillation amplitude and converts it into an electrical signal. The variable component of the electrical signal can be applied to the input of Lock-In amplifier, RMS detector and Phase detector.

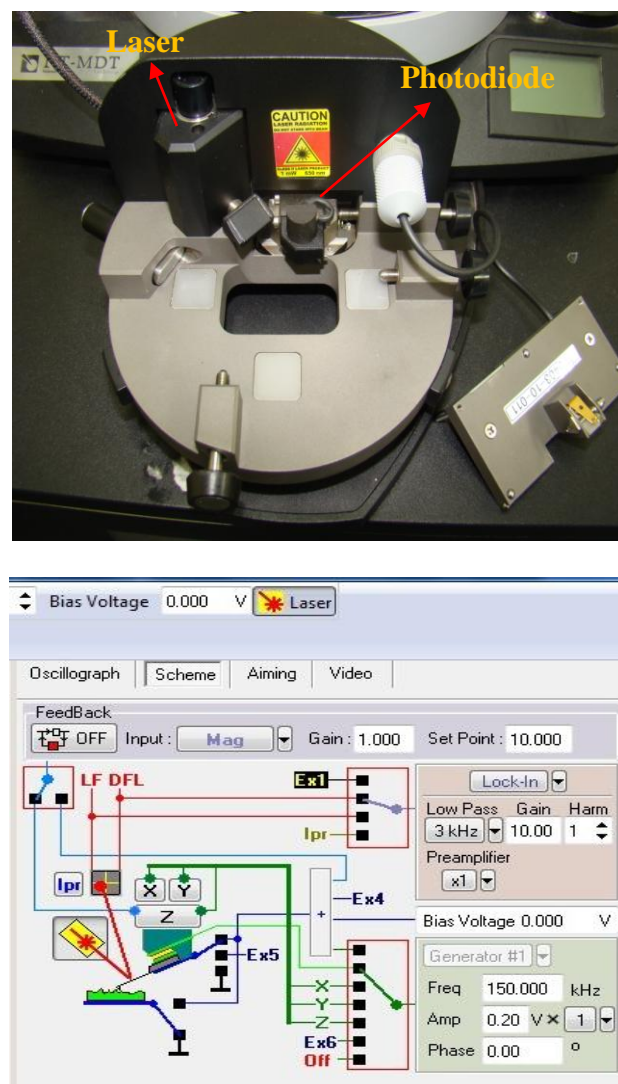


Figure 2.4 Photograph of AFM head and schematic of control electronics panel.

For vertical bending vibrations, the difference of AB and CD photo diode signal (DFL) was monitored and for torsional and lateral vibrations AD and BC difference signal (LF) was recorded as shown in figure 2.5. The device electronics is controlled by the commercial software “NOVA” program. Typical vertical and lateral bending vibrations of MC1 obtained using AFM head shown in figure 2.6 (a) and (b). First vertical bending (VB1) and Lateral bending mode (LB1) is obtained by monitoring DFL and LF signals. The direction of vibration of each mode is shown as inset. It may be noted that the vibration amplitude of VB1 is higher than the LB1 mode for a same piezo excitation.

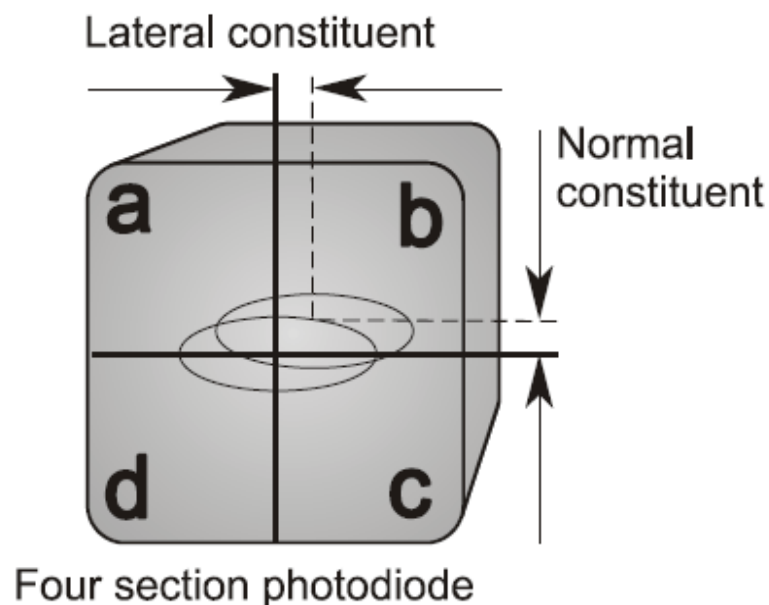


Figure 2.5 The four quadrant photo diode system in AFM. Normal constituent corresponds to difference of AB and CD photo diode signal and it gives information about vertical vibrations. Lateral constituent corresponds to difference of AD and BC signals and it gives information about lateral and torsional vibrations.

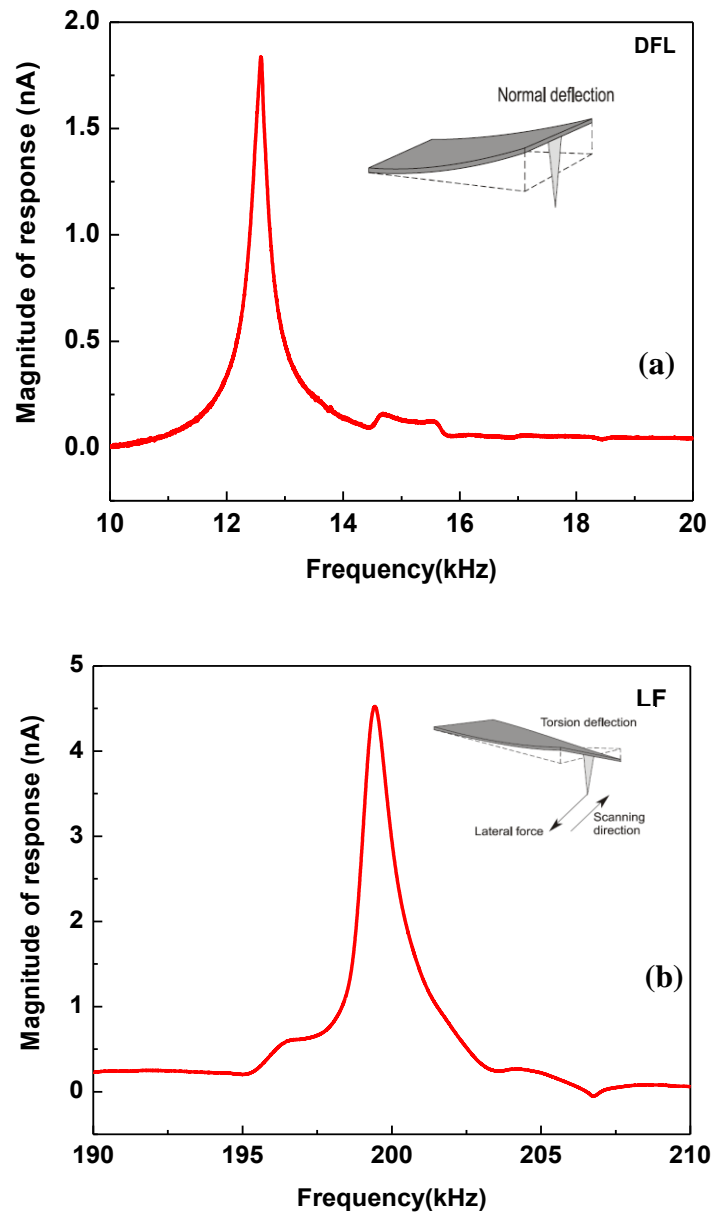


Figure 2.6 First vertical bending (VB1) and lateral bending (LB1) modes of MC1 obtained using AFM shown in (a) and (b) respectively. Amplitude of vibrations is in nA. The direction of vibration for VB1 and LB1 is shown as inset.

For static measurements, the DFL signal was monitored with time. In this case, MC was not excited by piezo. Figure 2.7 shows a typical deflection response of MC with time when relative humidity is reduced from 50% to 6%.

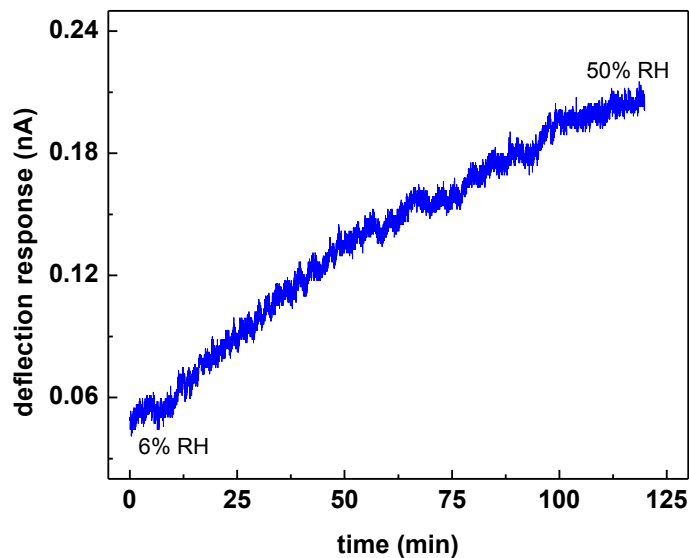


Figure 2.7 Deflection response of MC1 with time when relative humidity is reduced from 50% to 6%.

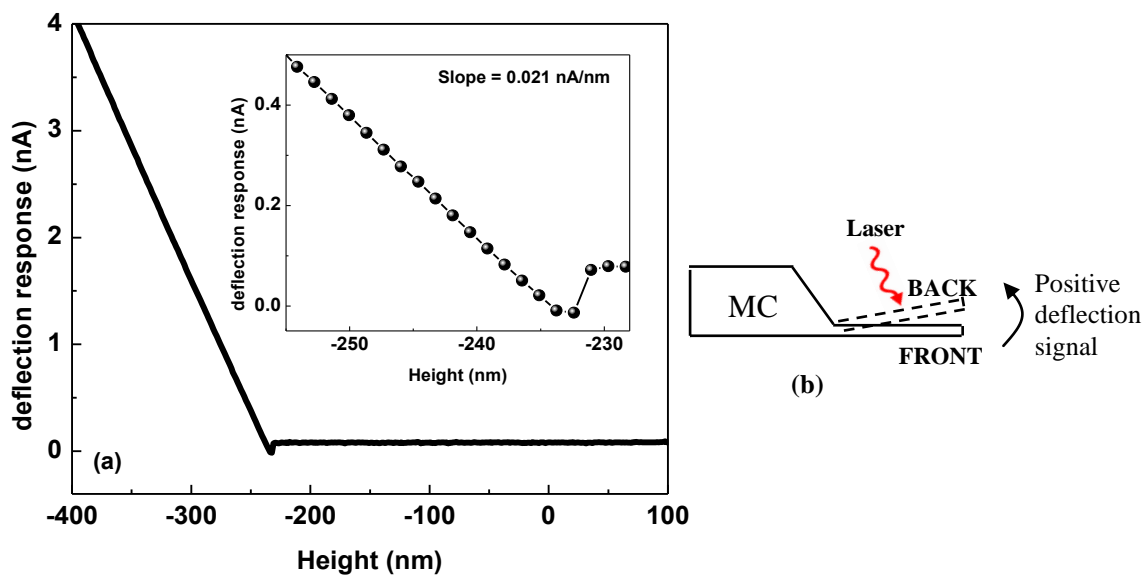


Figure 2.8 Calibration curve obtained by performing force distance curve on hard Si surface in motion. From linear contact part, slope was found to be 20 pA/nm shown in inset. (b) Deflection direction of MC towards back during positive deflection signal of MC.

Deflection response (nA) can be converted into deflection (nm) by dividing with the calibration slope. To obtain calibration slope, force curve on a hard Si surface was measured by pushing the end of the MC to a defined distance upward by a piezoelectric crystal [5] and is shown in figure 2.8. Force curve is a measure of the photodiode current (I_{PSD}) versus height position of hard surface placed on the piezoelectric translator (Z_p). From the linearly increasing contact part (see inset of figure 2.8), deflection sensitivity $\Delta I_{\text{PSD}}/\Delta Z_p$ was obtained and was found to be 20 pA/nm. Now, MC deflection (Δz) was obtained using the formula $\Delta z = I_{\text{PSD}} / (\Delta I_{\text{PSD}}/\Delta Z_p)$. A positive deflection signal implies MC is bending in the direction of laser focusing i.e. towards back (see figure 2.8(b)) and vice versa.

2.4 Experimental set up for water adsorption studies on microcantilevers

A schematic diagram of the apparatus and photograph of experimental set up used for water adsorption studies is shown in figure 2.9 (a) and (b). For adsorption of water molecules, experiments are performed by placing the AFM head along with the MC, inside an airtight chamber purged with dry nitrogen (N_2) gas which reduces the Relative Humidity (RH) to 6% over a period of 2 Hrs. The flow rate of the gas inside the chamber was in the range of 100-500 ml min^{-1} . For increasing the RH, N_2 is bubbled through DI water. RH in the chamber is measured using a standard RH meter with an accuracy of $\pm 3.5\%$ RH. Shift in different resonant mode frequencies (VB, LB and TB) and deflection response during RH increase and decrease was also studied using this setup.

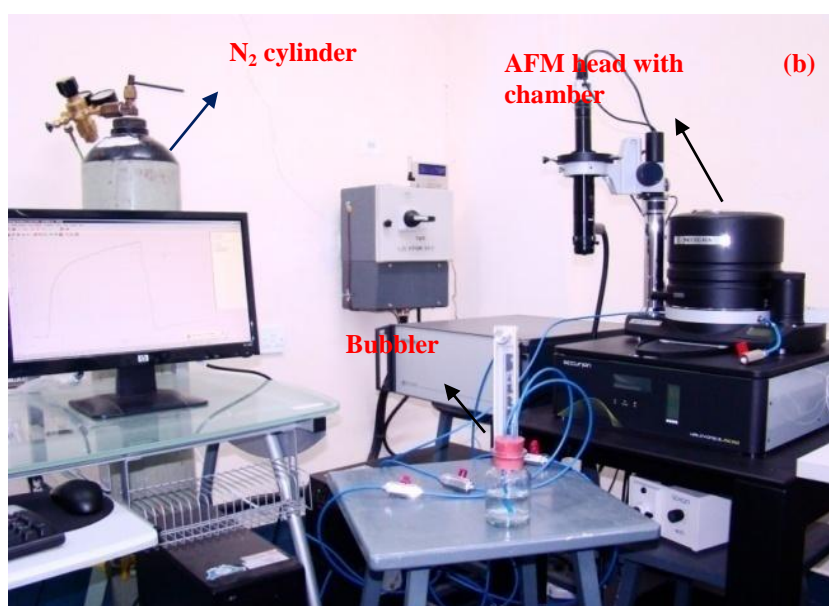
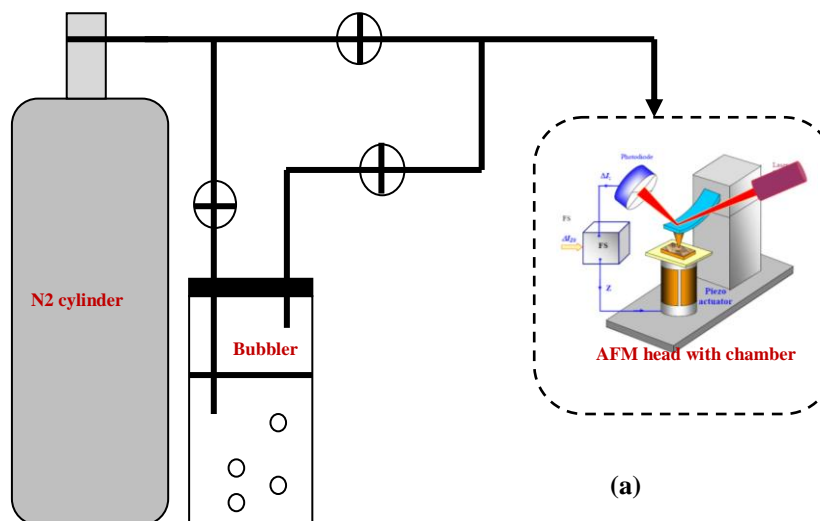


Figure 2.9 (a) Schematic diagram and (b) Photograph of the experimental set up used for water adsorption studies. Dry/wet N_2 gas is purged into chamber to reduce/increase relative humidity in the chamber.

2.5 Nano vibration analyzer

Apart from AFM head, Nano Vibration Analyzer (NVA) was also used to measure the natural frequency of MCs. The NVA (M/s SIOS, Germany) is a fiber-coupled laser interferometric vibrometer integrated in a precision technical microscope. It is

excellently suitable for measurements of dynamic properties and static displacements of microstructures, MEMS and microcantilevers.

The working principle of the interferometer measuring system is based on the application of a classic Michelson interferometer with plane-mirror reflectors utilizing the interference effect. The scale is based on the extremely exact wavelength of a He-Ne laser. All optical parts of the interferometer are located within the sensor head and balanced. The sensors are designed so that they can work on optically rough surfaces. This means that they do not require an additional reflector. The measuring beam emitted by the He-Ne laser passes through optics which focuses the beam on the object to be measured. The sensor head contains a miniature interferometer, which transforms the motion of the measurement reflector into an optical signal. This quantized, optical measuring signal is transformed in the sensor head into electrical signals, which are then transmitted to the modular supply and evaluation unit. There the signals are completely preprocessed up to the signal normalization with respect to amplitude and offset [6].

The block diagram and the photograph of the experimental setup used to measure the natural frequency of MCs using NVA are shown in figure 2.10 (a) and (b). MC was glued on a piezo actuator, which was excited using a function generator. The measuring laser beam ($\lambda = 632.8\text{nm}$) was focused on the MC with a microscope objective of focal length of 35 mm and the back reflected signal interferes with the reference signal inside the interferometer. This optical signal is transformed into electrical signal using a photo diode, which is then transferred into the electronic unit where it is amplified and is fed into a PC interfaced. Position of the laser beam on MC was also monitored using a USB based digital camera with CMOS sensor

which is mounted on microscope and was connected to a separate PC. By varying the function generator frequency in steps of 100 Hz amplitude of vibration was recorded at each frequency and resonance frequency was estimated from the peak of the plot of frequency v/s amplitude and is shown in figure 2.10 (c). To perform this task a software routine in commercial software *InfasVIBRO* was written (see Appendix A 1). The advantage of this technique is one can obtain the mode shapes of the vibrating cantilever experimentally by scanning the MC area.

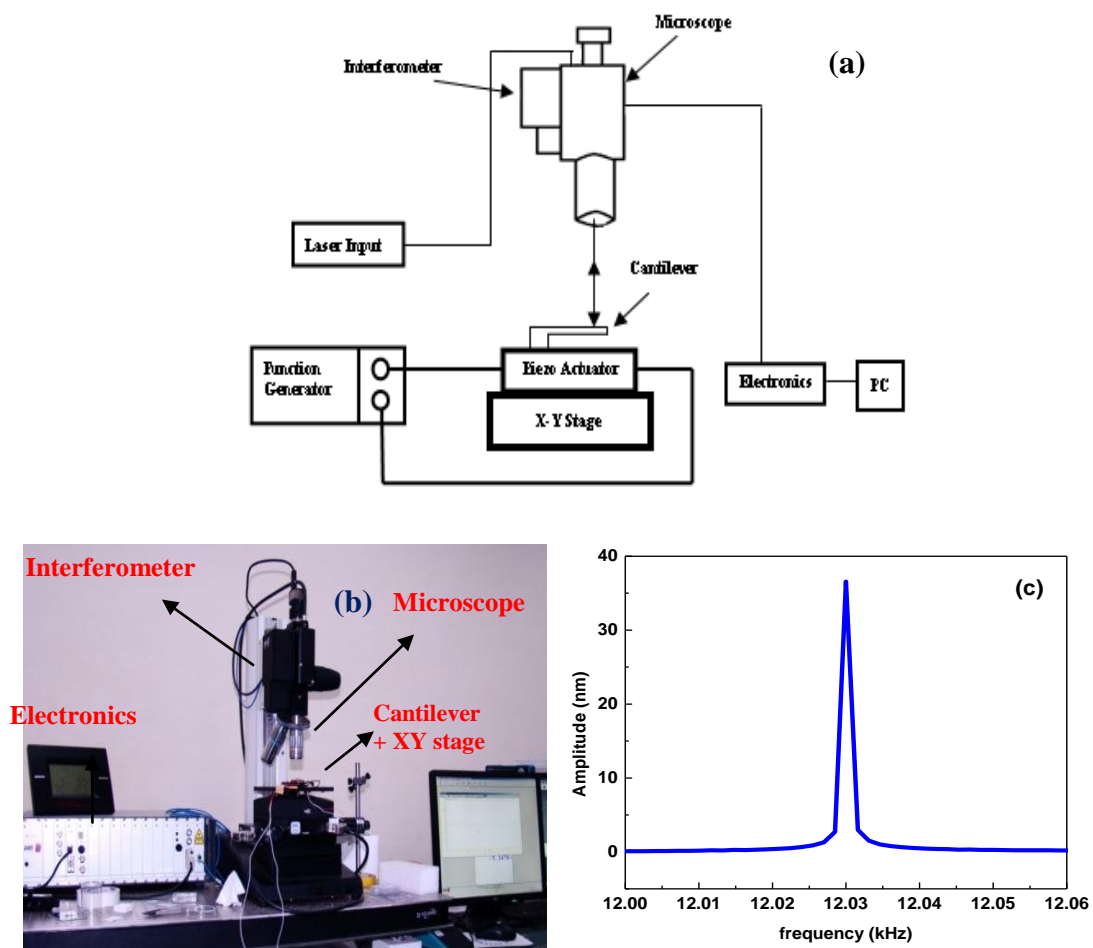


Figure 2.10 (a) Block diagram and (b) photograph of experimental setup used for estimating the natural frequency of the cantilever using NVA. (c) Resonance spectrum of MC1 obtained using NVA.

2.6 FEM analysis

Finite element modeling (FEM) analysis is performed using a commercial MEMS CAD tool (*Intellisuite*). FEM is a practical approach to simulate MEMS behavior under different types of loads such as mechanical and thermal. To estimate the natural frequency of MC, the cantilever of desired dimensions (MC1, MC2 and MC3) is designed by specifying the dimensions in the *3d builder* module of the *Intellisuite* software. Then the same is imported to the *thermo electromechanical* (TEM) module and the simulations are performed by setting static and dynamic analysis. Mesh size is selected and then the material properties are selected from material database of the software. One end of the MC is fixed by boundary condition and the simulation was performed. In the simulation, MC with the asymmetric corner notches at the free end of the MC was taken into account.

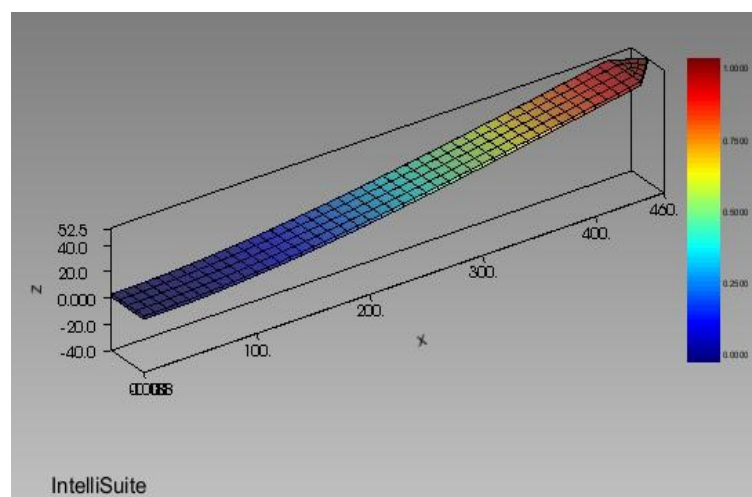


Figure 2.11 Mode shape of first vertical bending mode of MC1. Mesh used was 3nm. Normalized amplitude of vibration of mode is shown.

The material and geometric properties used for the model are: Young's modulus (E) = 106 GPa, Density (ρ) = 2328 kg/m³. These dimensions were adopted from the technical data sheet provided by the supplier [1]. After estimating the natural

frequency of the desired MC, mode shapes were obtained using *Visual ease* module. Figure 2.11 shows the mode shape of first vertical bending mode of MC1 obtained using FEM.

2.7 Functionalization of microcantilevers with polymers

2.7.1 Synthesis of PAAm and PVP polymer solutions

For addition of mass on MC, Polyacrylamide (PAAm) was prepared by chemical route [7]. Aqueous solution of acrylamide (AAm) is prepared by dissolving 0.6M of AAm and 2.5mM of potassium persulfate (KPS) in 15mL of water. The AAm solution is de-aerated by argon gas purging for 5 minutes. 36 μ L of N,N,N',N'-Tetramethylethylenediamine (TEMED) is added to the AAm solution and vortexed it for 2 minutes. The AAm solution is allowed to stand for 10 minutes during the course of which AAm polymerized to polyacrylamide (PAAm).

For gamma dosimeter studies, Polyvinyl pyrrolidone (PVP) was coated on MCs. It was prepared by dissolving 30mg of PVP in 1 ml of Ethanol solution.

2.7.2 Dip coating set up

Figure 2.12 shows the experimental setup used to add the polymer mass on MC by dip coating. Both MC and polymer solution (in a container) were mounted on two different 3-axis manipulators to allow the precise movement of the both. Now, by carefully observing through a digital microscope (200x magnification), MC was slowly dipped inside the polymer solution (see inset of figure 2.10), kept for 20 minutes, removed slowly and was allowed to dry over night. The mass added on

MC was determined by the shift in the fundamental resonance frequency and was used to estimate the mass sensitivity.

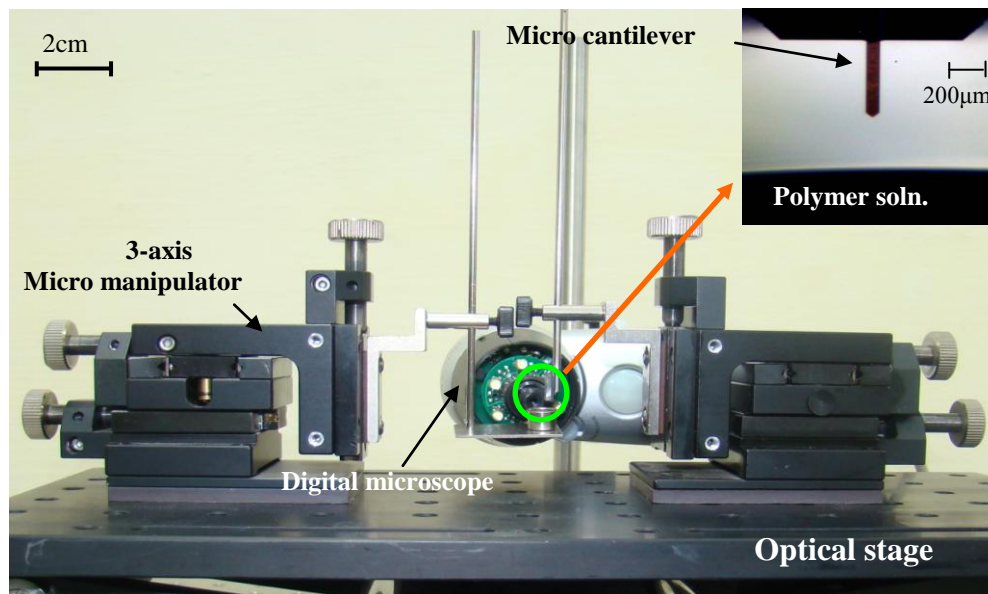


Figure 2.12 MCs are coated with polymer solution using this dip coating setup. MC and polymer solution in a container are mounted on two 3-axis micro manipulators, and by carefully observing through a digital microscope, MC was dipped into the solution (see inset), kept for 20 minutes and removed.

2.8 Preliminary studies on identifying the higher modes of vibration of microcantilevers

In the present thesis, the mass sensitivities of higher modes of MCs are compared. AFM head is used to obtain frequency spectra of MCs. The frequency sweep was done initially in the range of 5 kHz to 2 MHz with a step of ~ 200 Hz, and after identifying the modes it was repeated with a high resolution step of 2 Hz at every mode. While doing this, piezo drive voltage was increased accordingly to excite the mode efficiently. Figure 2.13 shows the VB signal between 5 kHz to 1500 kHz of MC1 obtained using AFM head. Each peak in this figure represents a mode and are

numbered from 1 to 7 accordingly. By comparing FEM results, modes 1 to 7 are identified as VB modes VB1 to VB7. These are indexed in figure and some of mode shapes with the normalized amplitude are shown in inset. It may be interesting to note that the mode assignment is only based on frequency and no significance is ascribed to the amplitude of peaks in figure 2.13.

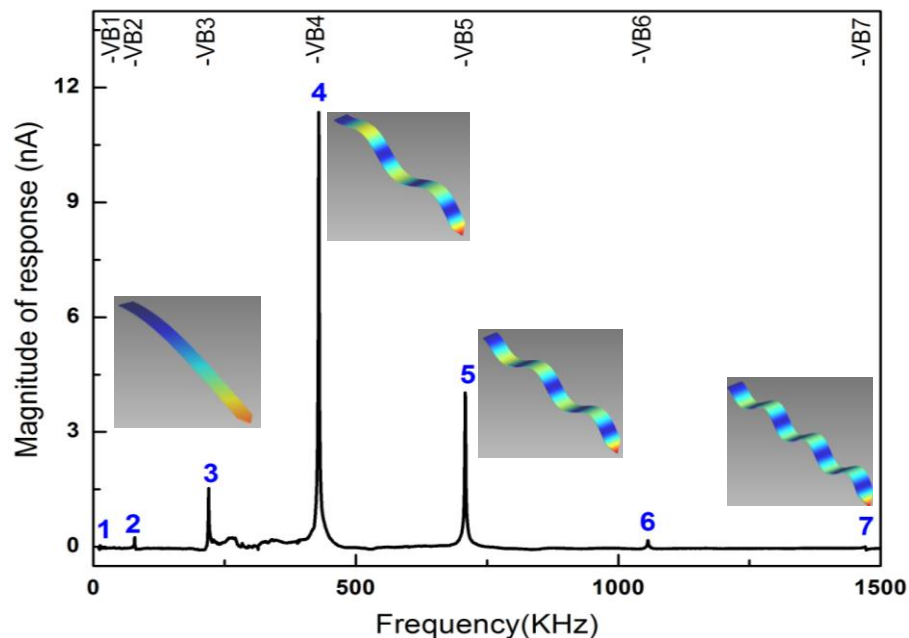


Figure 2.13 Experimental results of vertical bending (VB) signals of the microcantilever studied in the present work using AFM head. Seven unique modes of vibration are identified and assigned from FEM simulations (shown as stick). Some of the mode shapes are shown as inset.

It is seen that the peak between 300 kHz to 500 kHz has highest amplitude for a given piezo excitation in the MC as compared to other modes. This arises due to the complex resonance associated with the piezo actuator, spring clamp used to hold the MC and MC chip used in the present experimental setup. This complex resonance is not seen when the frequency spectra was obtained using NVA. Figure 2.14 shows the frequency spectra of MC1 obtained using Nano Vibration Analyzer (NVA). Initially the frequency sweep was done for individual mode of vibration with a step

of 100 Hz and finally all the modes of vibrations are plotted as the frequency spectra shown. It is clear from the figure that fundamental mode of vibration has large amplitude as compared to other modes of vibration for a given piezo excitation.

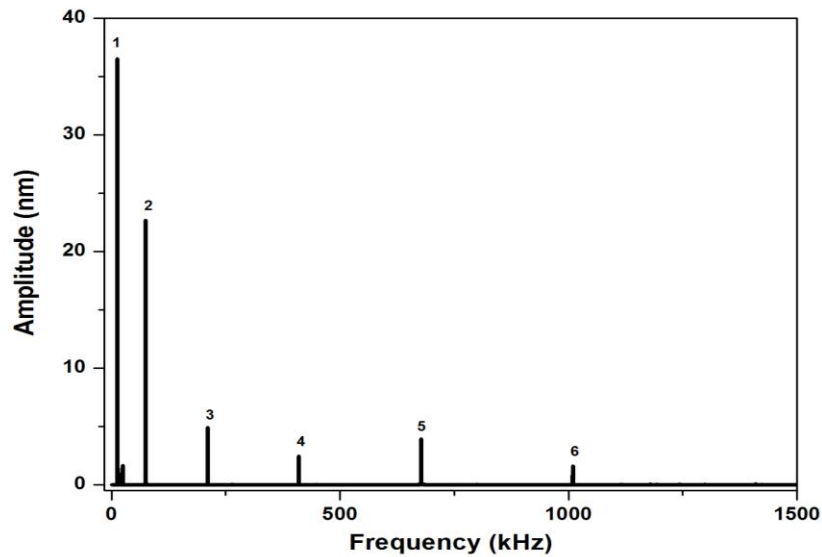


Figure 2.14 Frequency spectra of MC1 obtained using NVA. The peaks in the spectrum corresponding to vertical bending modes. VB1 has higher amplitude of vibration as compared to other higher modes.

Apart from VB signals, lateral (LB) and torsional bending (TB) signals are also recorded for MC1 using AFM head. Figure 2.15 shows the LF signals of MC1 between 5 kHz to 1500 kHz. LB signal apart from the peaks at the same position as VB signal, four unique peaks are identified and are numbered from mode 8 to mode 11. From FEM analysis, the peaks are identified as lateral and torsional bending vibrations. The appearance of vertical bending signals in torsional bending signals and vice versa (not seen here) is due to reasons like improper coupling of the piezo actuator vibrations to MC, geometric imperfection of MC and MC chip, etc., This also explains the very fact that why for a vertically excited cantilever, torsional bending modes of the MC arise [8].

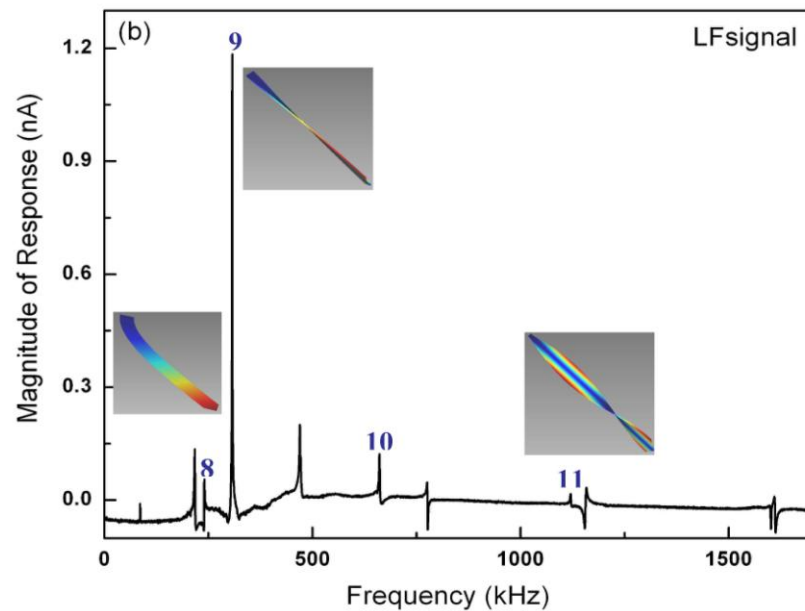


Figure 2.15 LF signal of MC1 obtained using AFM. This signal shows both Lateral (LB) and torsional bending (TB) of MC1. The peaks 8 and 9 corresponds to LB1 and TB1 modes of MC1.

2.9 Mapping of mode shape of microcantilever vibrations

In this work, mode shapes of microcantilever are mapped experimentally using NVA. To map the mode shape of any vibration one needs both amplitude and phase information of the vibrating structure. The phase of the excitation signal from function generator was given as a trigger to NVA. With this, NVA records at each position the amplitude of vibration and phase difference between excitation and MC vibration signal. To perform this task a software routine in commercial software *InfasVIBRO* was written and is given in Appendix – A 2. Script controlled software enables the laser beam to scan the object surface along the length and width direction (XY stage) and provides the amplitude of vibration and phase information with a resolution of $2\mu\text{m}$ on the surface of MC. Initially vibration and phase was recorded along the length of MC for three different modes and are shown in figure

2.16. The solid line in this figure is the polynomial fit. It is clear from the figure that as we move from fixed end to free end along the length of MC, the amplitude of vibration changes and becomes almost zero at certain points including fixed end also at certain points it becomes almost maximum which depends on excitation frequency and mode number.

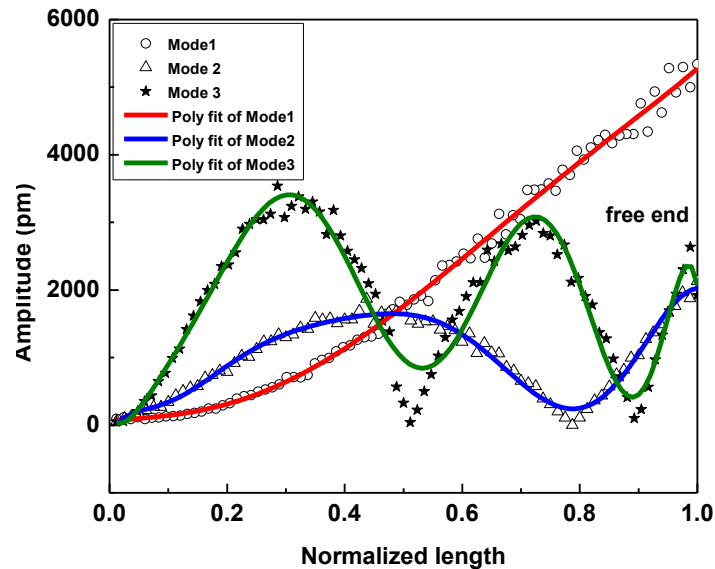


Figure 2.16 Mode shape of vibrations along the length of MC for its first three VB modes. The data is fitted to polynomial fit.

After the line shape analysis, more detailed scan in both XY direction was performed for various modes. The recorded data was imported into 3d imaging software for post processing. The first four vibrational mode shapes obtained by NVA are compared with the mode shapes of vibration obtained by FEM analysis of same dimensional MC shown in figure 2.17. It is clear from these figure that mode shape obtained experimentally matches well with simulation results. It is interesting to note that maximum amplitude recorded for fourth mode is only 0.4 nm.

The frequency values of MC1 for all modes of vibrations obtained using AFM head, NVA, Analytically and FEM analysis are compared and are given in table 2.2 and the difference between experiment and simulation is $< 2\%$.

Table 2.2 Frequency values of MC1 for all modes of vibrations obtained using AFM, NVA (experimental), Analytically and FEM analysis (simulation).

Modes	AFM (kHz)	NVA (kHz)	Analytical value (kHz)	FEM (kHz)
VB1	12.5945	12.030	13.46	12.5943
VB2	78.471	74.951	84.378	78.8322
VB3	219.36	209.901	219.36	220.479
VB4	429.272	409.302	462.98	431.514
VB5	708.084	677.490	764.55	712.387
VB6	1056.398	1008.591	1142.11	1062.7
VB7	1471.146	1409.507	1595.18	1482.06
LB1	199.446	-----	-----	214.925
TB1	313.458	-----	-----	314.046

2.10 Micro Raman studies on microcantilevers

MCs used in the present work are commercially available and apriori knowledge of residual stress present in these devices is crucial for the studies undertaken in the present thesis. Several techniques are reported in the literature for measuring stresses in microscale structures. One commonly used method is X-ray diffraction [9], but the lateral dimensions of the film are required to be greater than the spot size of the beam. Other techniques, such as bulge tests, bending tests and resonant tests,

are utilized in micro devices, but are limited by their lateral spatial resolution which exceeds tens of microns [10].

Micro-Raman spectroscopy is an interesting alternative technique to study stress in micro systems. The combination of Raman spectroscopy with optical microscope systems enables the incident beam to be focused to a spot with a diameter of 1 μm . It is capable of analyzing the local stress on a micrometer scale, and is extensively used for local stress evaluation in silicon microstructures [10-14]. This method is non-destructive, fast and accurate enough.

The Raman signal originates from interaction of light (photons) with lattice vibrations (phonons in a crystal). When monochromatic radiation is incident on the surface of a solid can undergo transmission, absorption, and scattering. In general, two properties can be defined by the electronic distribution within a crystal lattice in equilibrium, namely, the dipole moment, and electric polarizability. These properties will change with deviation in equilibrium interatomic spacing of the lattice or time-dependent vibrational motions around these equilibrium positions. In Stokes–Raman scattering, the incident photons interact with vibrating crystal (phonon), which induces changes in the polarizability of the solid, causing the scattered photons to lose a quantum of lattice energy or phonon relative to the incident photons. Frequency (ω) of the excited phonons is given by [15]

$$\omega = \left[\frac{1}{\lambda_i} - \frac{1}{\lambda_s} \right] \quad (2.1)$$

Where λ_i and λ_s are the wavelength of the incident and scattered radiation, respectively. The quantity ω is called the Raman shift in units of cm^{-1} . The Raman

spectrum contains information about the physical and chemical characteristics of the solid [15].

Mechanical stress and strain may affect the frequencies of the Raman modes. Stress or strain in Raman measurements can be obtained via so-called phonon deformation potentials (DPs), which are linear coefficients linking the change in the phonon frequency and the strain or stress in the material. For silicon, using the phonon deformation potentials of Chandrasekhar et al., [16] the stress (σ) is estimated as,

$$\sigma \cong -518\Delta\omega \quad (2.2)$$

In the equation, $\Delta\omega$ is difference between Raman shift measured with and without stress and expressed in cm^{-1} and σ is expressed in MPa.

Mechanical stress measurements of MC1 have been carried out using a Renishaw micro-Raman spectrometer. All spectra were excited with visible (514.5nm) laser light with power 2 mW and collected in the backscattering configuration. The spectra were recorded with a 3000 lines/mm grating. 50 \times objective was used to focus the excitation laser light on the right spot of the MC1. The exposed time was taken 1 s. First the experiment was performed on the substrate of the MC1 at room temperature (24 $^{\circ}$ C). Experiments were performed at three different positions on MC1 namely free, fixed end and middle of the MC1 with same experimental condition. The experimental results of Raman peak shift and broadening due to laser heating at various positions on MC1 are studied. Effect of laser power on Raman shift at various positions on a free standing MC is studied. Raman shift along the length of the MC in free standing position, front and back resting on a substrate is also presented. Careful experiments were performed to measure this residual stress in three different configurations along the length of the microcantilever. Measured

Raman shift was converted into Stress using equation (2.2) with respect to Raman shift measured on the substrate.

Figure 2.18 shows the Raman shift (RS) at room temperature on the substrate of MC with Lorentzian fit. The observed RS and width are 520.95 cm^{-1} and 8.1685 cm^{-1} respectively which is close to ideal value.

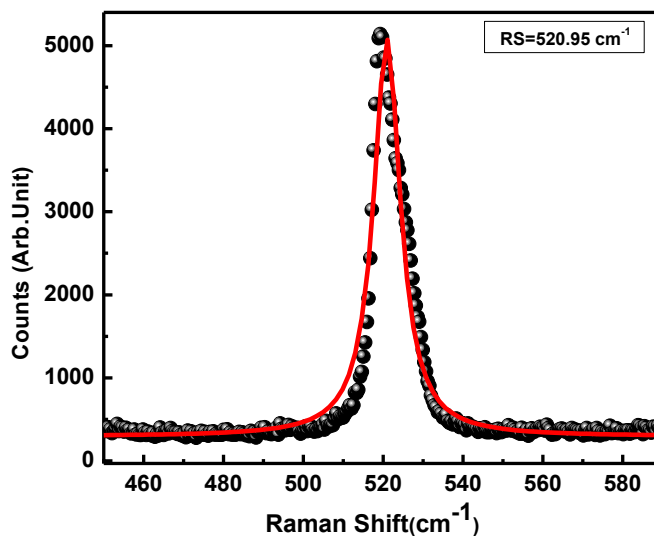


Figure 2.18 Raman shift at room temperature on the substrate of the cantilever with Lorentzian fit.

2.10.1 Effect of Laser power

Figure 2.19 (a) shows the variation of Raman shift on the substrate and at three different positions of micro cantilever namely fixed, middle and free end of the cantilever with increasing power. Figure 2.19 (b) shows these three different positions on a free standing MC during the experiment. From this figure following observations can be made. In general with increasing laser power there is a negative shift in Raman peak at all the positions indicating the rise in temperature due to localized heating. It is known when the crystal lattice is heated, the equilibrium positions of the atoms are displaced, resulting in an overall volumetric expansion of the lattice and a change in interatomic forces. These changes in the interatomic

forces modify the phonon vibrational frequencies which results in red shift in the resulting Raman phonon spectra [14, 17]. Difference in Raman shift is maximum of 6.87 cm^{-1} at free end of the cantilever for 40 mW laser power. This is because of small thermal mass of the microcantilever and also because the heat generated at free end can not readily dissipate into to the surround air. This is due to the large difference between thermal conductivities of silicon (150 W/mK) and air ($\sim 0.024 \text{ W/mK}$). Therefore the only way of removing the heat will be via the fixed end and substrate which can be considered as an infinite sink. This is evident from figure 2.19 where the observed shift is proportional to the distance from the fixed end. Based on these observations, for stress estimation in these devices 2mW laser power was chosen. It may be noted this is only the laser power at the source and sample will be exposed to about one fourth of it due to optical losses throughout the beam path [18]. At laser powers lesser than 2 mW, Raman count rate becomes very less and the stress profiles on the cantilever are not repeatable.

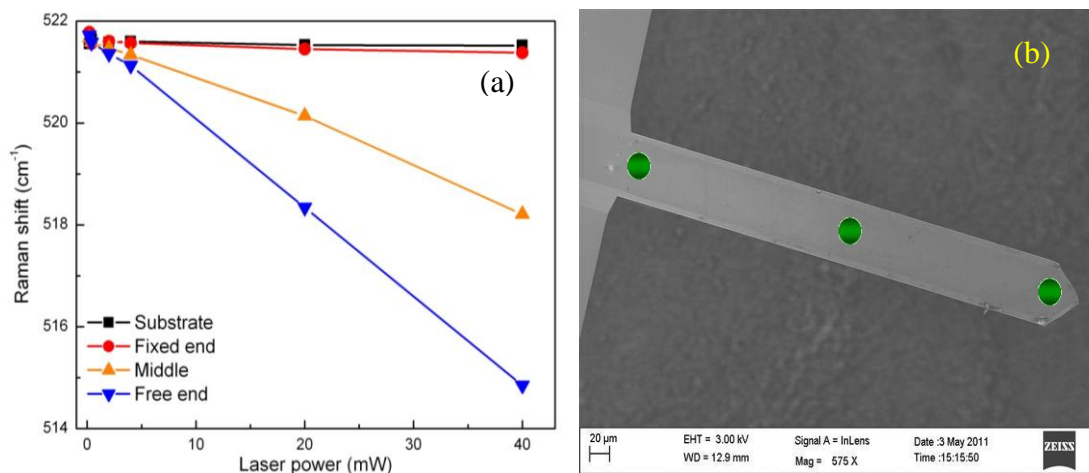


Figure 2.19 (a) Variation of Raman shift with increasing laser power at three different positions namely free end, middle and fixed end of the MC1 (b) Three different positions on a free standing MC1.

2.10.2 Residual stress in microcantilever

It is well known that the general uniaxial residual stress field in a thin film may be approximated to a polynomial [18, 19];

$$\sigma(z) \approx \sigma_0 + \sigma_z \left(\frac{z}{t/2} \right) \quad (2.3)$$

Where $z \in [-t/2, t/2]$ is the coordinate along the thickness with origin on the symmetry plane. In this first approximation, σ_0 represents the constant mean stress which is symmetric about the mid plane and σ_z represents the gradient stress and is anti-symmetric. The gradient stress is due to localized effects including atomic diffusion through thickness of micro cantilever, interstitial or substitutional defects and atomic penning [18]. The stress gradients contribute to axial load and bending moment, cause the structural stiffness change and out of plane deformation of micro cantilever [20]. The stress gradient profile responsible for the cantilever bending is obtained in the present work using micro-Raman. Careful experiments were performed to measure this residual stress in three different configurations along the length of the microcantilever. Measured Raman shift was converted into Stress using equation (2.2) with respect to Raman shift measured on the substrate.

Figure 2.20 shows the Raman shift and the estimated stress variation along the length of the microcantilever for three different experimental configurations i.e when it is front, back and back resting on substrate (as shown in inset) estimated. Following observations can be made from this figure. Stress is tensile and maximum at about 200 μm from fixed end on the front side, whereas on back side and back touching cases stress is compressive and the trend is opposite compared to front side. The opposite sign of stress on front and back side under no load

conditions indicate the cantilever bending induced by the presence of residual stress. At the fixed end the stress was maximum and was found to decrease when going towards free end. Although the trend is same, when compared to back side in back touching configuration stress reduces to 50 percent and might be due to stress relaxation as it is resting on a plane surface. This opposite trend also proves that the observed Raman shift is due to the stress and not due to local temperature rise due to probing laser. In that case, irrespective of the configuration, the Raman shift would have been more at free end compared to fixed end.

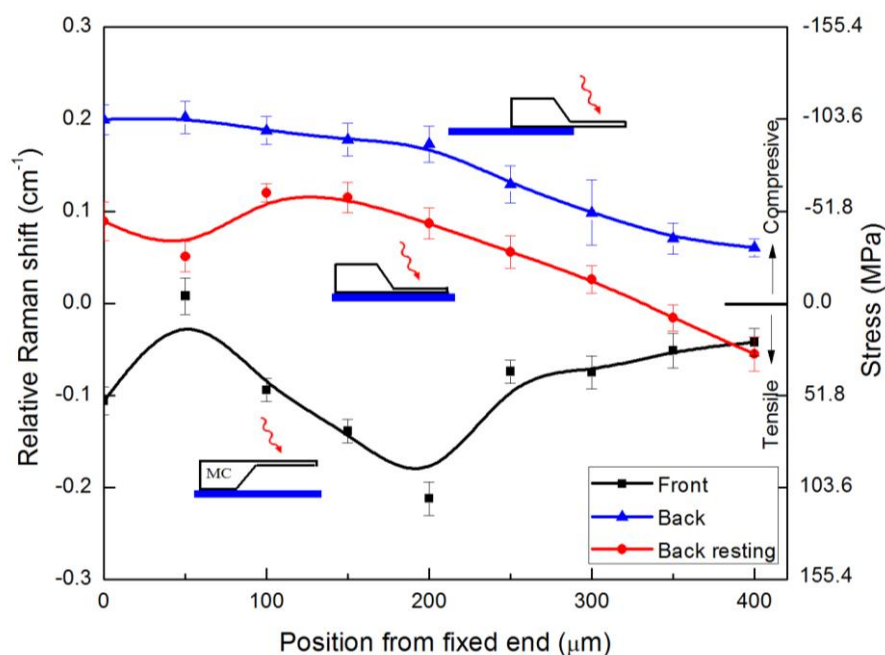


Figure 2.20 Raman shift along the length of the microcantilever in free standing position and resting on a substrate as shown inset. Stress calculated from Raman shift using equation 2.2 is shown in right axis of the figure. Arrow shows the laser probing direction and for these experiments 2 mW laser is used.

Raman spectroscopy is an effective technique to study the residual stress in microcantilevers with a good spatial resolution. Measured stress is tensile on the front side and is compressive on the back side. The opposite trend on front and back side clearly proved the microcantilever bending due to the presence of residual stress.

It is pointed out that while using micro Raman for stress measurements in microcantilevers, lowest laser power must be used to avoid the local heating induced Raman shift especially at free end.

2.11 References

1. Tipless micro cantilevers, M/s Appnano, USA and Duo 500 from M/s micromotive microtechnology, germany
2. J.E. Sader, J.W. Chon and P. Mulvaney, *Rev. Sci. Instrum.* 70, (1999)p. 3967–3969
3. Y.S. Lo, N.D. Huefner, W.S. Chan, P. Dryden, B. Hagenhoff, and Thomas P. Beebe, Jr., *Langmuir* 15, (1999) p.6522-6526
4. S.A. Syed Asif, K.J. Wahl and R.J. Colton, *J.Mater.Res.* 15, (2000)p.546-553
5. H.J. Butt, B. Cappella, M. Kappl, *Surface Science Reports* 59, (2005) p.1-152
6. Laserinterferometric vibrometer Series SP-S and LSV user's guide
7. J. Gao, B.J. Frisken, *Langmuir.* 19, (2003) p. 5212-5216
8. L. B. Sharos, A. Raman, S. Crittenden, and R. Reifenberger, *Appl. Phys. Lett.*, 84, (2004) p.4638
9. M. James, J. Lu, and G. Roy, *Handbook of Measurement of Residual Stress: Englewood Cliffs, NJ: Prentice Hall; 1996*
10. Wu. Xiaoming, Yu. Jianyuan, Ren Tianlin, Liu Litan, *Microelectronics Journal* 38, (2007) p.87–90
11. I. De Wolf, *Semicond. Sci. Technol.* 11 (2), (1996) p.139–154
12. M. Siakavellas, E. Anastassakis, G. Kaltsas, A. G. Nassiopoulos, *Microelectronic Engineering* 41/42, (1998) p.469-472
13. V.T. Srikar, A.K. Swan, M.S. Unlu, B.B. Goldberg, S.M. Spearing, *Microelectromech. Syst.* 12 (6), (2003) p.779–787
14. T. Beechem, S. Graham, S. P. Kearney, L. M. Phinney, and J. R. Serrano, *Rev. Sci. Instrum.* 78, (2007)p. 061301
15. M. J. Pelletier, *Analytical Applications of Raman Spectroscopy*, Oxford, U.K.: Blackwell Science, 1999.

16. M. Chandrasekhar, J. B. Renucci, and M. Cardona, *Phys. Rev. B.* 17, (1978) p.1623–1633
17. Mark Richard Abel, “Thermal metrology of polysilicon mems using raman spectroscopy”, Ph.D. Thesis, Georgia Institute of technology, August 2005.
18. W. Fang and J. A. Wickert, *J. Micromech. Microeng.* 6, (1996) p.301–309
19. J.A. Thornton and D.W. Hoffman, *Thin Solid Films* 171, (1989) p.5-31
20. Y. Zhang, Ya-pu Zhao, *Microsyst Technol* 12, (2006) p.357–364

Chapter 3 - Microcantilever based mass sensors

In this chapter, methods to enhance the mass sensitivity of microcantilever (MC) based sensors are presented. Working at higher modes and reducing the dimensions of MC are compared. It is shown that mass sensitivity increases linearly with increase of eigenvalue (λ_n^2) and decreasing dimensions (T/L^2) where T is thickness and L is length of MC, that is, effectively by increasing the base frequency of the resonator. Using, FEM simulations, mass sensitivities for various nanostructures like nanobelt, nanowire and nanotube attached to a conventional MC are studied. Simulation results predict that mass sensitivity can be enhanced by two orders even by tailoring the shape of the given structure. It is found that a millimeter sized cantilever can be effectively used as sensitive mass sensor over a wide dynamic range of 10 μg to 10 mg. Finally, polymer coated MCs are explored for gamma radiation dosimeter application. It is pointed out that PVP coated MCs can be used for gamma dosimetry.

3.1 Enhancing the sensitivity of microcantilever based mass sensors

Silicon-based MCs are widely used in Atomic Force Microscopy (AFM) and have been used in many sensing studies [1-3]. These sensors offer improved dynamic response, greatly reduced size, high precision, and increased reliability compared with conventional sensors. When mass adsorbs on the MC surface, the resonance frequency of MC will shift, which can be monitored and the detected mass measured quantitatively. MC based mass sensors benefit from two distinct advantages over

other resonant mass sensors (eg. Quartz crystal microbalance (QCM) and surface acoustic wave (SAW) [4, 5]) namely, higher sensitivity and the possibility of implementation in arrays. The smaller mass of the cantilever ensures the advantage of higher sensitivity, while the smaller size of the cantilevers makes it possible to implement arrays of cantilevers in a limited area, especially when the readout is integrated with the sensors, as in the case of piezoresistive cantilevers [6].

In all of these mass sensors, the vibratory mass of the resonator, its resonance frequency, and quality factor (Q) are central in establishing its mass sensitivity. The aim is to reach maximum sensitivity (maximum frequency shift for a given mass change) and resolution (minimum detectable mass). In this pursuit, zeptogram (10^{-21} g) sensitivity obtained in vacuum has been recently reported [7]. A general approach to gain higher sensitivity is to reduce the inertial mass of the resonating sensor itself. Mass sensitivity increase from picogram (pg) to femto gram (fg) was achieved by reducing the volume of the device by ~ 1000 times [8]. Different sensor geometries and various materials are also reported to measure small masses [9-11].

3.1.1 Mass sensitivity

The amount of added mass on the MC can be determined from the changes in the resonance frequency of MC and is given by equation 1.14 in chapter 1. When absorbents are uniformly distributed on the cantilever surface assuming the spring constant of a MC remains unchanged, the mass change Δm is obtained from the resonance frequency shift Δf , given by,

$$\Delta f = -\left(\frac{f_n}{2m^*}\right)\Delta m \quad (3.1)$$

and mass sensitivity (S) is defined as [14],

$$S = \left(\frac{\Delta f}{\Delta m} \right) = - \frac{f_n}{2m^*} \quad (3.2)$$

Therefore, to achieve high sensitivity in mass detection, it is necessary to use a cantilever with a small mass and a high resonant frequency. Nano cantilevers are therefore promising in extending the detection limit down to a few molecules [12].

By combining equation (1.9) and (3.2) we find that,

$$S \propto (\lambda_n^2) \left(\frac{T}{L^2} \right) \quad (3.3)$$

It is clear from equation (3.3) that S can be enhanced either working at higher modes or by reducing the dimensions i.e. as mentioned earlier, by increasing the base frequency of the resonator. Note that the above discussion is under assumption that the added mass do not affect the spring constant i.e. it will not rigidly bond to the surface of MC. Apart from vertical bending modes, other higher modes like torsional and lateral modes were also shown to enhance the mass sensitivity [13-15]. Several workers have compared the two methods viz., working at higher modes and reducing the dimensions of MC for improving the mass sensitivity. Jeong Woo Yi et al [16] studied the effect of eigenvalue of nth mode (v_n), length (L) and width (w) on mass sensitivity of centimeter sized piezoelectric unimorph cantilevers and found that it is proportional to $(v^2 / L^3 w)$. They also validated their findings to MCs with dimensions down to 100 μm . Ghatkesar *et al* [17] studied the mass sensitivity of higher modes of MCs of different thickness. They reported that increase in mass sensitivity is linear with the square of the mode number and pointed out that working at higher mode, keeps the larger surface area of the MC which is required for biological sensing. Lochon et al [18] reported that mass sensitivity can be

enhanced either by reducing the dimensions of MC or by using higher modes. They opined that working at higher modes, instead of reducing the dimensions to enhance the sensitivity will circumvent the difficulties of reproducible sensitive coating on very small surfaces and integrating deflection measurement of very small microstructures. They also theoretically compared various factors affecting Q-factor in both the cases and concluded that only when support losses play a role, then higher mode is better compared to reducing the dimensions case. Recently, Narducci et al [19] compared the mass sensitivity of higher modes vs reducing the dimension of a piezoresistive MC and found a gain of 4.1 using higher mode and 16.8 using reducing the dimensions. But, they did not discuss the effect of mass addition on Q-factor of their resonators.

3.1.2 Quality factor

Sensitivity of the MC when used as a mass sensor also depends on the spectral resolution, which is directly related to the Q-factor of the resonant mode as discussed in chapter 1 [20]. The Q-factor is an important parameter of a vibrating body. It describes the quality or the width of the resonance frequency peak. The narrower the resonance frequency peak, the easier and more distinct the peak is to detect. The Q-factor is dependent on the damping and, since the damping plays an important role in the calculations, it is necessary to measure it.

Q-factor of a resonant mode is estimated using

$$Q = f_n / \delta f \quad (3.4)$$

where δf is bandwidth of the resonance measured at 3 dB points shown in figure 3.1. The bandwidth, appearing in equation is the width of the frequency curve, at half power point. The half power point is defined to be $\frac{A}{\sqrt{2}}$ of the peak value of the resonance frequency curve, where A is the maximum amplitude of the vibration at a specific frequency [21]. Q-factor reflects the losses that take place when resonating MC is immersed in a fluid. Some of the known loss mechanisms associated MCs are: thermoelastic losses, viscous and acoustic losses in surrounding medium and support losses due to radiation of elastic waves [18].

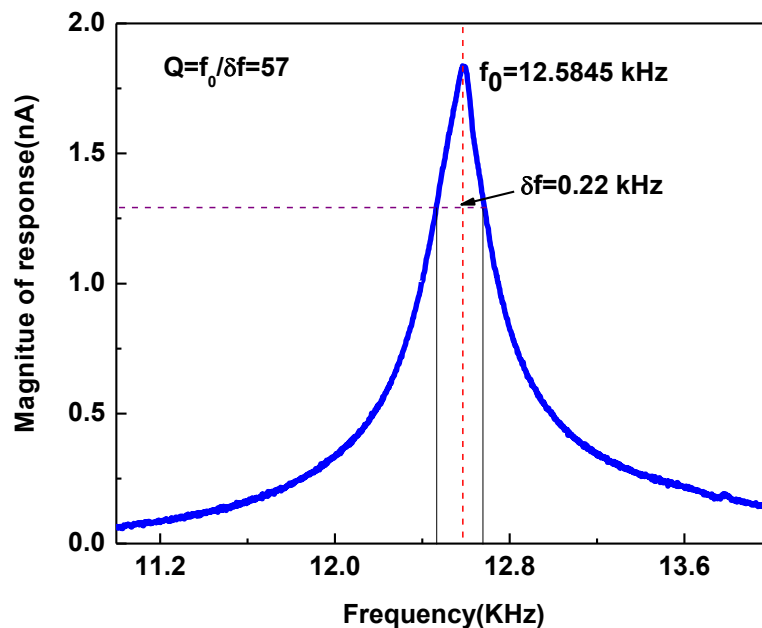


Figure 3.1 Estimation of quality factor from resonance spectrum (VB1) of MC1.

In the present work, the enhanced sensitivity and quality factor of polymer-coated MC when working at higher modes and reducing the dimensions are compared. We find that Q factor decreases after the addition of polymer mass especially at higher modes, and suggest that reducing the dimensions is better compared with working at higher modes.

3.1.3 Comparison of mass sensitivities of microcantilever when working at higher modes and reducing dimensions

Figure 3.2 shows the resonance frequency of the VB1 of MC1 before (f_1) and after dip coating the polymer (f_2) and it shifts from 12.5945 kHz to 12.490 kHz ($\Delta f = -104.5$ Hz) indicating the mass loading. Details of the frequency measurements and dip coating setup are given in chapter 2. The added mass was estimated to be 1.62 ng using equation (3.1) which gives a mass sensitivity ($\Delta f / \Delta m$) of 0.0645 Hz/pg. In this calculation, we have used the spring constant of MC as 0.149 N/m, calculated by Sader's method [22] for a cantilever vibrating in air as discussed in section 2.1 in chapter 2.

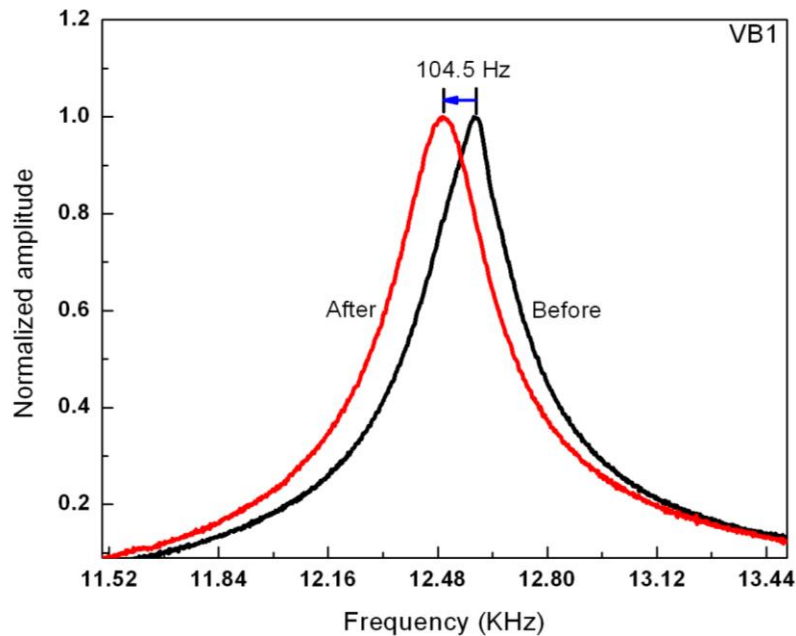


Figure 3.2 Shift in natural frequency of first vertical bending mode (VB1) of MC1 for an added mass of 1.62 ng.

Analytically the polymer mass was estimated to be 1.83 ng from the volume of the polymer film (thickness was estimated using AFM) and known density (1.302 g/cm^3) [23].

Similar analysis was done for all the modes and the mass sensitivity estimated along with frequency shift and Q-factor for all the modes is shown in table-3.1.

Table 3.1 Resonance frequencies before (f_1) and after coating polymer (f_2), Q-factor before (Q_1) and after addition of mass (Q_2), shift in frequency due to added mass (Δf) and estimated mass sensitivity (S) for MC1, MC2 and MC3.

S.No	Mode	f_1 (kHz)	Q_1	f_2 (kHz)	Q_2	Δf (kHz) (f_2-f_1)	$S = \Delta f / \Delta m$ (Hz / pg)
MC1							
1	VB1	12.5945	55.699	12.490	61.821	-0.1045	0.0645
2	VB2	78.471	134.327	77.896	137.599	-0.575	0.3547
3	VB3	219.36	247.015	217.12	182.144	-2.24	1.3817
4	VB4	429.272	376.549	426.18	339.852	-3.092	1.9072
5	VB5	708.084	261.653	702.35	260.52	-5.734	3.5369
6	VB6	1056.398	590.809	1047.79	444.355	-8.608	5.3096
7	VB7	1471.146	651.501	1458.25	474.359	-12.896	7.9546
MC2							
8	VB1	65.188	146.152	63.791	128.1	-1.393	0.8453
MC3							
9	VB1	329.105	443.404	327.827	473.581	-1.278	5.4779

This table also shows the results obtained for MC2 and MC3. From this table following observations can be made. With the added mass, natural frequency decreases in all the modes and is as expected according to equation (3.1). In the case of MC1, as reported in literature [16, 17, 19], with increasing mode number sensitivity increases by about two orders from VB1 to VB7. Further, the mass sensitivity also enhances by two orders from MC1 to MC3, i.e. by reducing the dimensions, for the fundamental mode. Figures 3.3 (a) and (b) shows the variation

of mass sensitivity with square of Eigenvalue (λ_n^2) and decreasing dimensions (T/L^2) respectively. From this figure it is clear that mass sensitivity increases linearly in both the cases, as expected from equation 3.3.

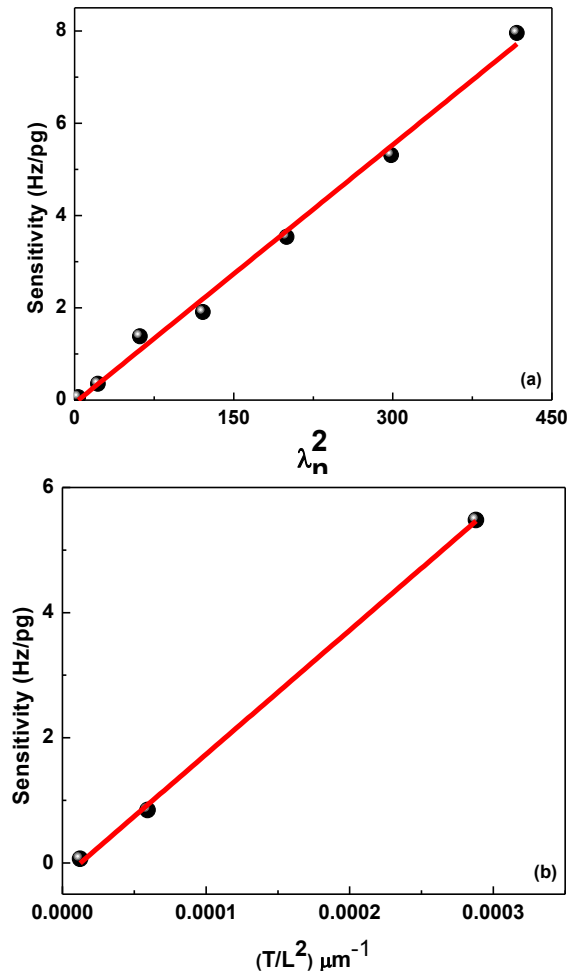


Figure 3.3 Variation of mass sensitivity with (a) square of Eigen value for MC1 and (b) T/L^2 of MC1, MC2 and MC3 at VB1

For 1.62ng added mass on the MC1, the frequency shift of 13 kHz at mode 7 is two orders of magnitude larger than 104 Hz at mode1. The corresponding mass sensitivity values are 7.95 Hz/pg at mode 7 and 0.06 Hz/pg at mode1. This indicates an unprecedented increase in sensitivity by two orders of magnitude at higher modes compared to lower modes for the same amount of added mass. This fact yields the

advantage to exploit large frequency changes from higher modes and increase the sensitivity of the cantilever to measure smaller masses.

These observations lead to an important conclusion that the mass sensitivity of cantilever sensors can be increased by working at higher modes without changing their physical parameters. Furthermore, larger physical dimensions give an added advantage of larger surface area for adding more mass and increase mass response. Since the sensitivity is inversely proportional to the squared length, a reduction of the length will increase the sensitivity. But care must be taken while reducing the length, because the length must remain greater than the thickness for model validity, and for actuation and detection issues. Indeed, the higher stiffness of short MCs may compromise efficient actuation, and the movement detection may be difficult for short MCs. Moreover, the reduction of the microcantilever length may also be limited by considerations about the sensitive coating deposition, as a minimal surface must be available for the deposition [19].

As mentioned earlier, sensitivity of any MC also depends on Q-factor. Figure 3.4 (a) and (b) shows the variation of Q-factor before and after the addition of mass with the increase of mode number and for the fundamental mode with reducing the dimensions.

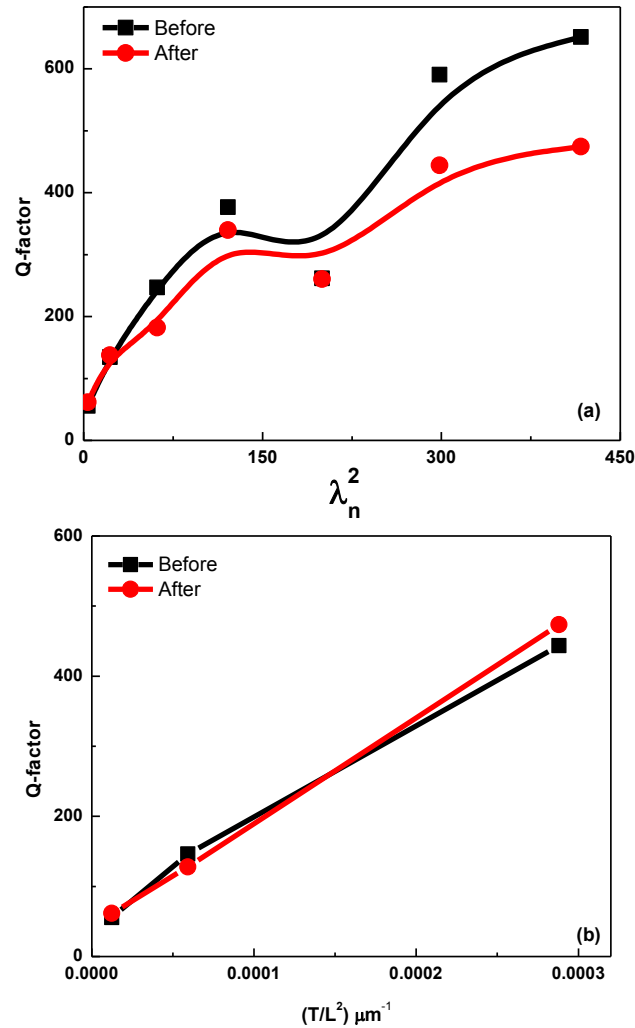


Figure 3.4 Variation of Q-factor before and after addition of polymer mass with (a) square of eigenvalue for MC1 and (b) T/L^2 of MC1, MC2 and MC3 at VB1

From figure 3.4 (a) it is clear that, Q-factor reduces after the addition of mass, compared to unloaded MC especially at higher modes. This is attributed to the losses associated with the viscoelastic nature of the polymer coating. These losses increases with increasing polymer coating thickness and there exists an optimum thickness for a given MC dimensions [24]. But in the case of reducing dimensions (figure 3.4(b)), there is no significant difference between the Q-factor of the loaded and unloaded MC.

3.1.3.1 Discussions

The advantages and disadvantages of both these methods to enhance the mass sensitivity are given in table 3.2.

Table 3.2 Advantages and disadvantages of the each method i.e. working at higher modes and reducing the dimensions of MC

Parameter	Working at higher modes	Reducing the dimensions
Mass sensitivity	Enhanced by two orders by working at 7 th bending mode	Enhanced by two orders
Surface area available for addition of mass	Large	Minimum
Repeatability of mass addition	Possible	Difficult
Support losses	No	Plays a role
Q-factor after coating with polymer	Decreases	Does not change

It is clear from the above table that although mass sensitivity can be enhanced by either method, quality factor, which is an important parameter for sensor characterization, reduces after the addition of polymer mass at higher modes.

Apart from VB modes, mass sensitivities of Lateral (LB) and Torsional bending (TB) modes also studied in the present thesis. LB and TB modes are obtained by detecting LF signal as mentioned in chapter 2. Figure 3.5 shows the variation of mass sensitivities of VB, LB and TB modes with square of the mode number. It is clear

from the figure that the mass sensitivities of TB modes are higher as compared to VB modes.

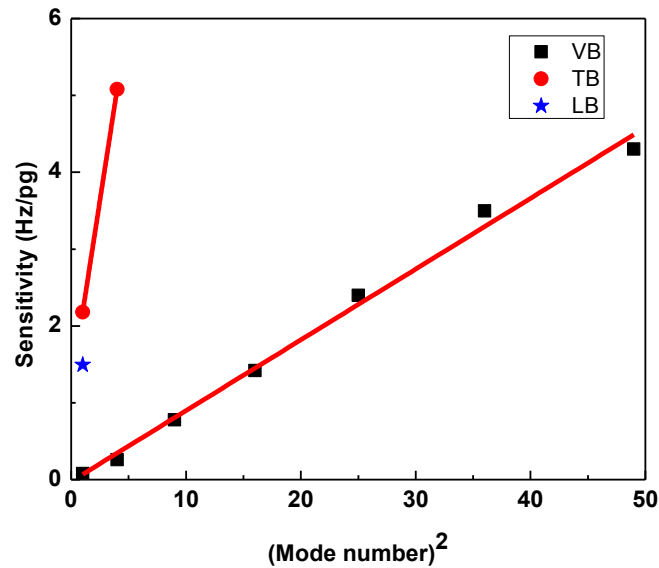


Figure 3.5 Variation of mass sensitivities of VB, LB and TB modes with square of the mode number.

3.2 Tailoring the cantilever for enhanced mass sensitivity – FEM simulation studies

In the present thesis, apart from MCs, mass sensitivity of nanocantilevers also studied through FEM simulation. Nanocantilevers are extensively studied as an alternative to mass spectrometry where the true mass of the molecules can be determined without ionizing the molecules [25-27]. It also has the potential to work with extremely small sample volumes and to be miniaturized to make portable devices for identifying molecules. In this technique, mass detection is performed by measuring the resonant frequency shift of a resonator due to the added mass. Mass sensitivity (S) is given by equation 1.14. As pointed out earlier, the interest is to reach maximum sensitivity (maximum frequency shift for a given mass change) and resolution (minimum detectable mass) [28, 29]. To ensure this, natural frequency

and quality factor of the resonator has to be high [7]. In the nanomechanical regime, it is possible to attain extremely high fundamental frequencies approaching those of vibrational molecular modes. The small dimensions of nanowires and carbon nanotubes (CNT) and their extraordinary mechanical properties (tensile strength of CNT = 200 GPa, Young's Modulus = 1 TPa) [30, 31] take these structures potential candidates as a mass detectors [32, 33]. Apart from working at higher modes and reducing the dimensions, one can also physically tailor these cantilevers for enhancing the sensitivity because sensitivity also depends on effective mass. In the present thesis, modal analysis is performed using finite element modeling on tailored nanocantilevers for the possibility of enhancing the mass sensitivity compared to its conventional rectangular shaped ones.

Dynamic vibrational mode simulations have been performed on three different nano structures namely nanocantilever (NC), nanowire (NW) and nanotube (NT) were performed with the dimensions mentioned in insets of figure 3.6. Applied driving pressure was 10 MPa and a damping factor of 0.00125 (air). The material for all the three structures was selected as silicon with density (ρ) = 2.3 g/cc, Young's modulus (E) = 160 GPa. The 3D mesh generated for the calculations consists of cuboids with the dimensions of 20nm x 20nm x 20nm along the length direction of the structures. One end of the structure was fixed by selecting the boundary condition.

Fig. 3.6 shows the frequency response of the three structures in its first bending mode. This figure also shows the phase angle behavior at resonance. The resonance frequency and Q-factor of three structures namely NC, NW and NT are 371 MHz, 398, 668 MHz, 403 and 788 MHz and 399 respectively.

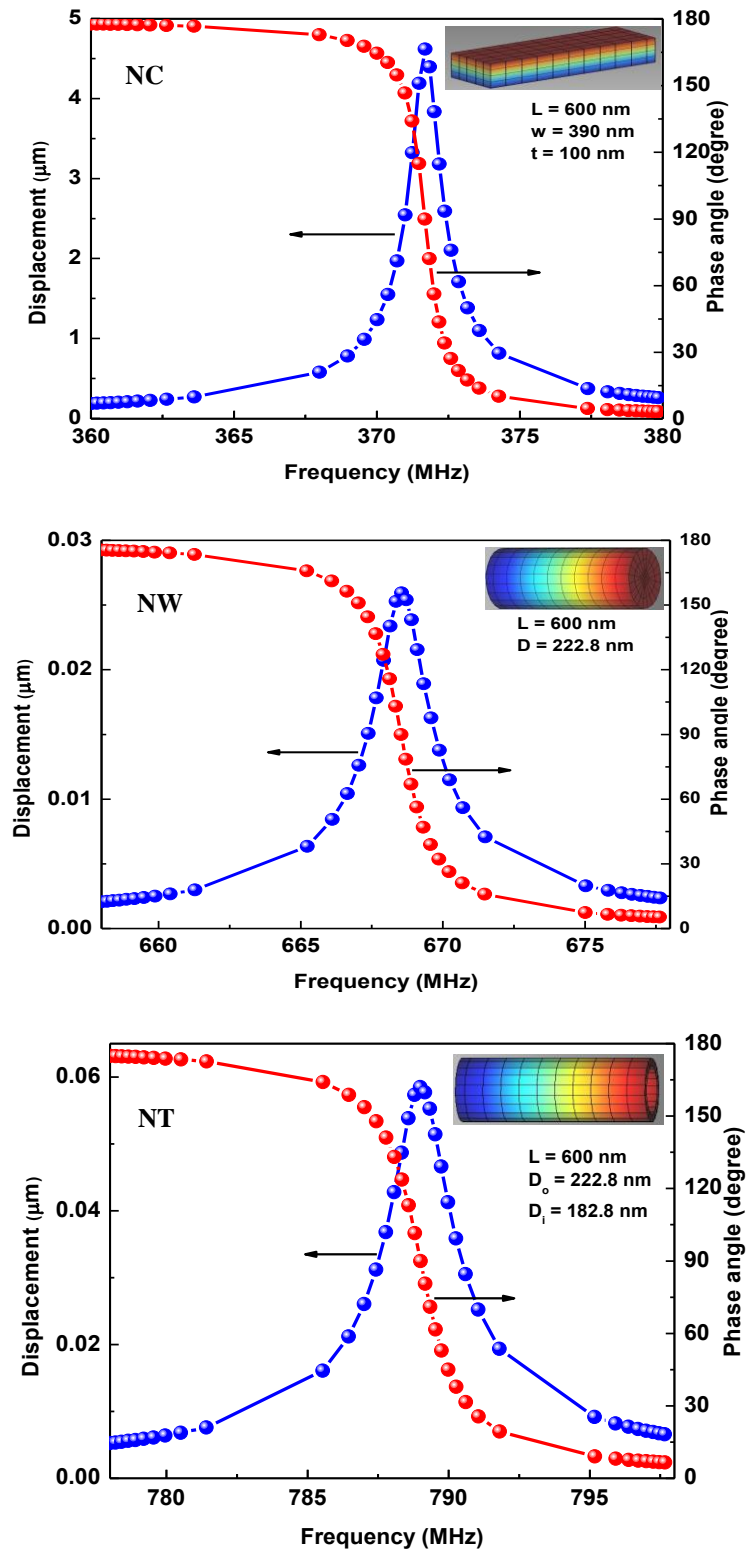


Figure 3.6 Frequency – displacement and phase angle curve for three different nanostructures namely NC, NW and NT. Right axis shows the corresponding phase angle behavior at resonance. Inset of these figures shows the geometry and dimensions of NC, NW and NT used for simulations.

The Q-factor obtained for NC is comparable to the experimental values obtained by Mo Li et al [12]. They reported a natural frequency of NC with a similar dimension as 127 MHz and Q-factor as 400. The difference in natural frequency may be due to different cantilever material used in the experiment.

Now, by placing a gold cube at the free end of these structures, mass sensitivity was estimated using equation 3.2. The obtained sensitivities for NC, NW and NT are 13 Hz/zg, 24 Hz/zg and 80 Hz/zg respectively. It is clear that for a given mass, NT gives higher sensitivity compared to other two structures. This is because, for a given length and a material (with same density and young's Modulus), resonant frequency depends on ratio of second moment of area (I) to mass (m) of beam under consideration. Compared to NC and NW, NT has highest I/m ratio and hence highest resonance frequency. If the young's modulus of Nanotube is 1000 Gpa, the structure would be CNT and sensitivity would further increase to 199 Hz/zg.

Initially a study was carried out to verify the accuracy of the FEM calculations. Carbon Nanotubes of given dimensions in table 3.3 are created and frequency analysis are performed using FEM software. Theoretically, the resonant frequency of a CNT depends on the NT outer diameter (D_o), the inner diameter (D_i), the length(L), the density(ρ) and the bending modulus of the nanotube (E) [34] is given

by $f_i = \frac{\beta_i^2}{8\pi} \frac{1}{L^2} \sqrt{\frac{(D_o^2 + D_i^2)E}{\rho}}$ where $\beta_1 = 1.875$ for the first harmonic. The natural

frequencies obtained By FEM simulations are compared with the theoretical and experimental results reported by D.H. Wu et al [35] and is shown in table.3.3.

Table 3.3 Comparison of FEM values with theoretical and experimental values of three different single walled CNTs

D₀ (nm)	D_i (nm)	L (μm)	E (GPa)	Theoretical (MHz)	Experimental (MHz)	Present study (MHz)
32	17.8	5.55	28.4	0.7684	0.658	----
49	26.1	4.65	28.6	1.6655	1.42	1.5943
63	26.8	5.75	20.3	1.1316	0.968	1.0824

A 3-10% difference can be observed between FEM values and experimental values reported. This discrepancy can likely be attributed to defects of the nanotube material arising from the manufacturing process.

Simulations were repeated by varying length, inner diameter and outer diameter of the CNT. As expected, by decreasing the length or increasing the inner diameter of the NT mass sensitivity was found to increase. Whereas reducing the outer diameter from (for a constant length and inner diameter) sensitivity was found to decrease. This is due to the fact that natural frequency of CNT is directly proportional to inner and outer diameter. It is well known that the mass sensitivity also depends on the actual position of mass loading on the cantilever [36]. To study this effect, mass sensitivity simulations were repeated by placing gold cube at various positions along the length axis for the three structures. Figure 3.7 shows the variation of sensitivity of CNT with varying the position of gold from the fixed end. It is clear from this figure that sensitivity is maximum at free end and it decreases as the gold position approaches the fixed end. This is since the mass response of the cantilever will

change with the actual position of the added mass since the vibration velocity of the cantilever surface varies with position [37].

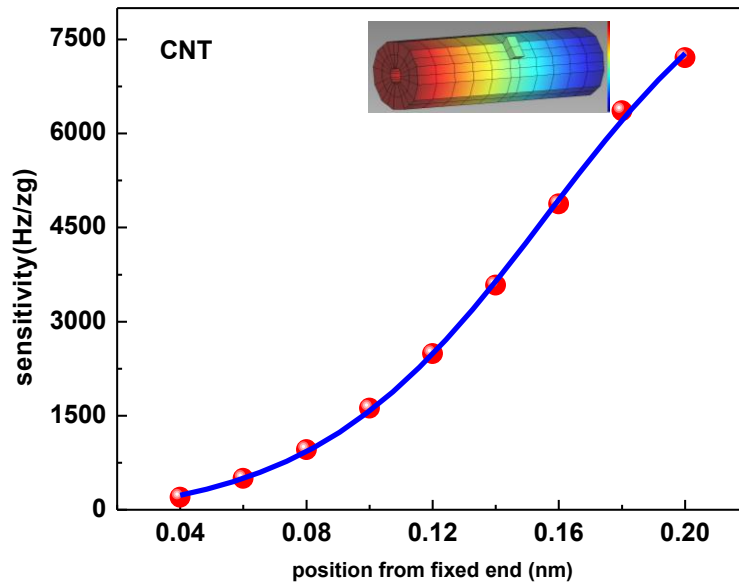


Figure 3.7 Variation of mass sensitivity of CNT with varying the position of gold from the fixed end

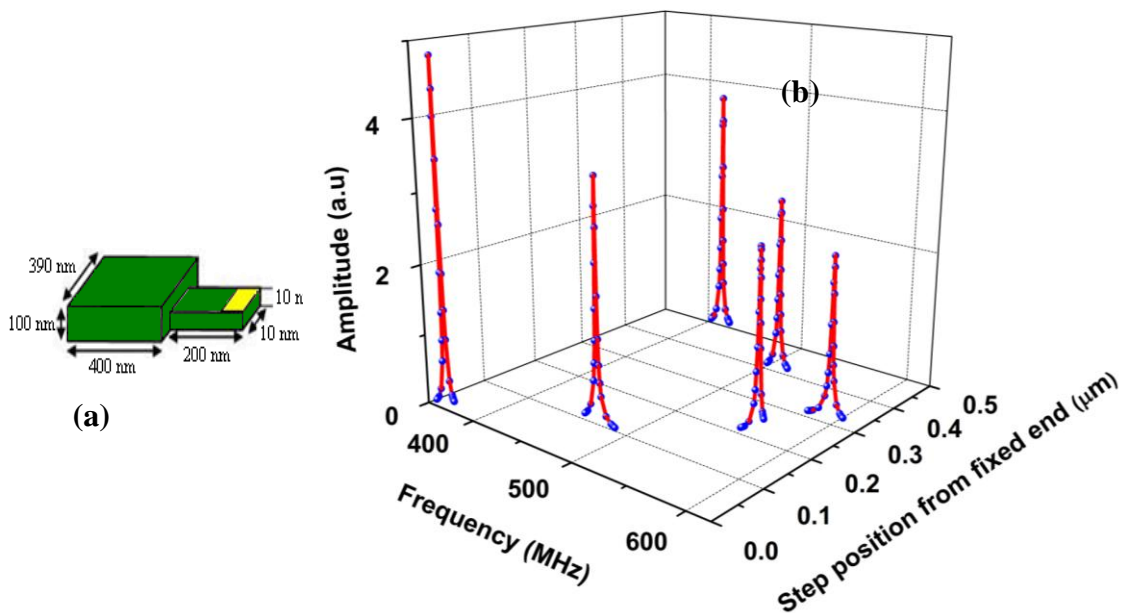


Figure 3.8 (a) Step position introduced at 200nm from fixed end of the NC (b) Variation of the resonance frequency of NC with position of step discontinuity along its length

Further to explore the possibility of enhancing the sensitivity of given length of the structure without reducing dimensions, a step discontinuity along the length of the cantilever was introduced at various positions from fixed end as shown in figure 3.8 (a). The calculated natural frequencies with step position are shown in figure 3.8 (b). From this figure it is clear that when the step is at 300nm from fixed end the natural frequency is maximum and thus maximum mass sensitive. Simulations were repeated to study the effect of the length and thickness of the step on the sensitivity. When step thickness and width was reduced to 10 nm the sensitivity of this new cantilever was 5117 Hz/zg. From this result it is clear that by introducing the step discontinuity sensitivity increases by 2 orders [38].

In a vibrating structure, such as a cantilever beam, the inertial property or the effective mass of the beam, stiffness of the beam and the damping parameters vary with time and with respect to their spatial locations. By modifying any one of these parameters one can vary the natural frequency and hence enhance the mass sensitivity of the cantilever. The introduced step discontinuity along the length will essentially modify the effective mass at the free end and fixed end there by moment of Inertia.

In conclusion, this study compared the mass sensitivity of three different nano structures. For a given length and material, sensitivity for rectangular, solid tube and hollow tube shapes were 13 Hz/zg, 24 Hz/zg and 80 Hz/zg, respectively. If the hollow tube structure is CNT, the sensitivity would further enhances to 199 Hz/zg. It is also proved that mass sensitivity is dependent on the position of mass loading in CNT based mass sensors. This study points to the possibility of enhancing the mass sensitivity of NC by physical tailoring. It is found that mass sensitivity of a

conventional rectangular NC enhances from 13 Hz/zg to 5117 Hz/zg when a step discontinuity along the length at 300nm is introduced.

3.3 Estimation of dynamic range of mass using millimeter sized cantilever

Dynamic range of mass sensor is studied using a millimeter sized cantilever in the present work. When absorbents are uniformly deposited on the cantilever surface, the resultant shift in mass Δm can be calculated using equation 1.14 of chapter 1. The same equation can be expressed in terms of shift in resonance frequency (Δf),

$$\Delta f = f_1 - f_1 \left[\frac{1}{\sqrt{1 + \left(\frac{\Delta m}{m_1} \right)}} \right] = f_1 \left[1 - \left(\sqrt{\frac{m_1}{m_1 + \Delta m}} \right) \right] \quad (3.5)$$

where f_1 , m_1 are the natural frequency and mass of the cantilever beam. To study the effect of reducing dimensions on the estimation of added mass, cantilevers with varying length from 4 mm to 10 mm are chosen. The frequency shift of these cantilevers is estimated theoretically using equation 3.5 by adding wide range of mass on them. Figure 3.9 shows the frequency shift of cantilever whose length L is varied from 4mm to 10mm for wide range of added mass. From the figure it is clear that as the cantilever dimension reduces, shift in resonance frequency increases but at a cost of linear range of the cantilever.

Theoretically there are no upper and lower limits of mass detection but experimentally lower limits of mass detection depend on the factors like thermo mechanical fluctuations, temperature fluctuations, adsorption-desorption noise and momentum exchange noise, and also depends on quality factor [39]. And upper

limits of mass detection depends on the mechanical properties (stiffness of beam) of cantilever beam, loading of mass must be in elastic limits. The theoretical plots are also verified with experiments. Cantilever used in this study is a piece of precisely cut single crystal n-type silicon wafer. Physical dimension of the cantilever are 8.3 mm (Length) x 2.1 mm (Width) x 0.43 mm (Thickness). The Young's modulus and the density of the silicon wafer are 156 GPa and 1766 kgm^{-3} respectively.

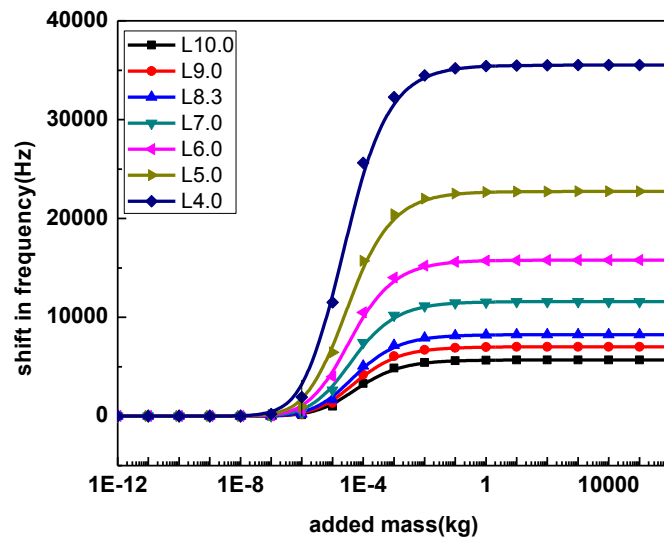


Figure 3.9 Frequency shift of cantilevers whose length is varied from 4 mm to 10 mm for the addition of wide range of mass

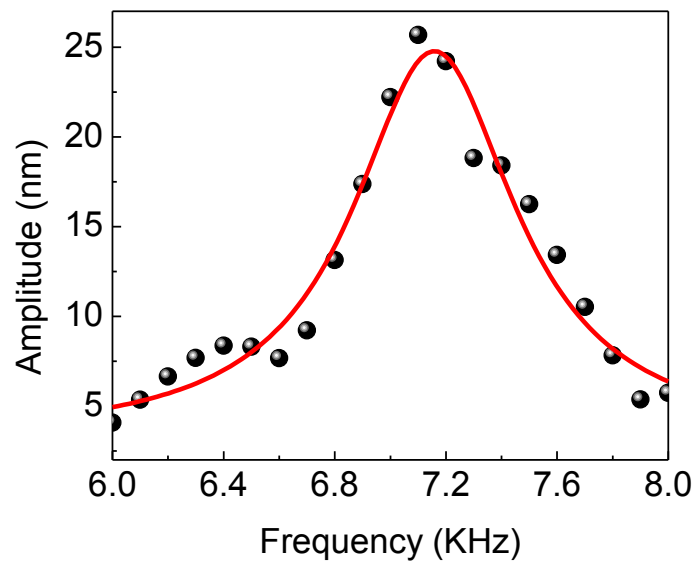


Figure 3.10 Resonance spectrum of the cantilever used obtained using NVA. Resonance spectrum is fitted to Lorentzian fit.

Natural frequency of the cantilever (with and without mass) was estimated using NVA as mentioned in chapter 2. The resonance frequency was estimated from the peak of the plot of frequency vs amplitude as shown in figure 3.10.

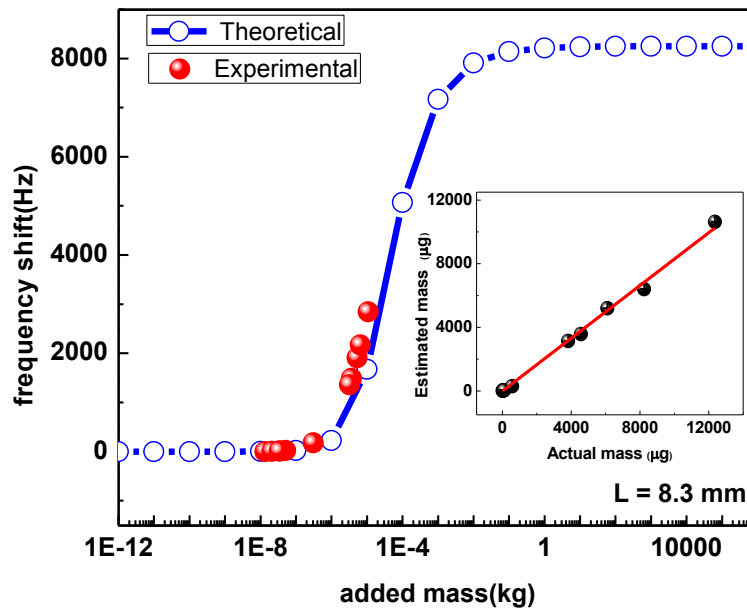


Figure 3.11 Variation of frequency shift of cantilever of length 8.3 mm with the addition of mass is compared theoretically and experimentally. The open circle shows the theoretical values and solid circle shows the experimental values. Inset of figure shows the linear variation between actual mass (calculated from volume and density of copper wire pieces) and estimated mass using NVA.

Experiment was repeated for various dimensions of copper wire pieces. The added mass (Δm) was estimated using the equation 1.14. Using this cantilever, mass of thin copper wire pieces were measured and are compared with theoretical values. Figure 3.11 shows the variation of frequency shift of cantilever of length 8.3mm with added mass. This plot compares the both theoretical and experimentally obtained values of frequency shift for the added mass. The open circles (blue color) show the theoretically obtained frequency shift and solid circles (red color) show the experimentally obtained values. The experimentally obtained values are following

the theoretical values. The inset of figure shows the graph between actual mass (calculated from volume and density of copper wire pieces) and estimated mass using the NVA as explained in chapter 2.

From this figure it can be concluded that, cantilever can be effectively used as sensitive mass sensor over a wide dynamic range of 10 μg to 10 mg.

3.4 Polymer coated microcantilevers for gamma radiation detection

Apart from mass detection, polymer coated MC's can be effectively used for photon detection. Thundat et al [40] demonstrated micromechanical detection of ultraviolet (UV) radiation of pJ levels using MCs coated with an UV sensitive polymer. They found that upon exposure to UV, a treated cantilever bends due to stress and its resonance frequency increases due to stiffening. They also anticipated that coating with a suitable polymer MCs can be used for gamma radiation. Datskos et al. [41, 42] demonstrated the remote detection of IR photons (with wavelengths ranging from 1 to 15 μm) using Piezoresistive MCs. Piezoresistive MC was coated with ~ 50 nm of gold, which served as the IR absorbing material and transfer the energy to the MC as heat, which causes bending due to bimetallic effect. They also attributed bending to the generation of photon absorption induced electronic stress in semiconductor material. Steinbock and Helm [43] studied the deflection of gold coated silicon nitride MC upon irradiation with light in the UV and visible wavelength range. They found a fast deflection upon UV exposure followed by a slower bending with relaxation-like characteristics. They further explained that, when exposed to UV, photons of sufficient energy promote electrons across the Schottky barrier to the

conduction band, thus creating free charge carriers, which induce a mechanical strain and result in bending of the cantilever. Stephan et al [44] used a MC as charged-particle flux detector. The principle of the detection is as follows. Alpha particles impinging on an insulated metallic charge collector plate deposit an electric charge on it. The resonance response of a MC positioned around 200 nm away varies due to electrostatic interaction, thereby detecting the charge on the collector plate. Herbert R Shea [45] reviewed on effect of radiation on performance of micromechanical devices. They concluded that dielectric based MEMS are more prone to degradation due to radiation induced trapped charge in dielectrics and in general silicon based MEMS do not fail until megarad dose.

In the present thesis, the possibility of using polymer coated MCs as gamma radiation dosimeter is explored. Four different polymer solutions (PAAM, PMMA, P3HT, and PVP) are prepared and are coated on MC4 using dip coating setup as discussed in chapter 2.

It is found that among four polymers, PVP coated MC4 alone was responding to the gamma dose and hence it will be discussed further. Figure 3.12 show the typical image of PVP coated MC. It may be noted, polymer film was coated only at the free end of MC to avoid the stiffening effect.

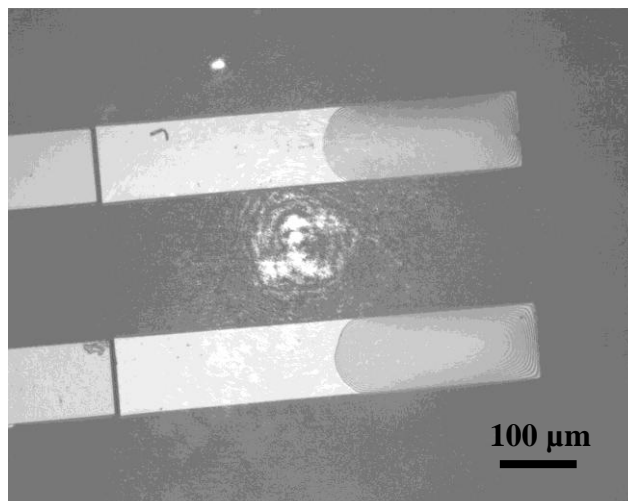


Figure 3.12 Optical photograph of the PVP coated MC. Polymer solution is coated only at the free end to avoid stiffening effect.

The polymer coated MC's were irradiated with gamma radiation using Cobalt – 60 source (M/s BRIT, India). The dose rate provided by the source as given by the supplier is 0.06 krad/sec. Change in natural frequency of the MC's at regular intervals of gamma dose is recorded using the NVA explained in section 2.5 in chapter 2. The experiments are conducted at ambient conditions. The prepared polymer solution was also coated on a silicon wafer and was irradiated along with MCs for other studies like surface morphology and force curve measurements by AFM. For the AFM study, the PVP coated Si wafer was mounted as a sample in AFM (NTegra Prima, Russia) and images were recorded in semicontact mode on AFM. A gold coated silicon tip with spring constant of 4.201 N/m was used for scanning the surface of PVP coated Si wafer after every gamma dosage.

Figure 3.13 shows the resonance spectrum of the virgin, polymer coated (PVP) MC measured using NVA as explained earlier. From the observed negative frequency shift (1.82 kHz), added mass on MC was estimated to be 31pg using equation 1.14.

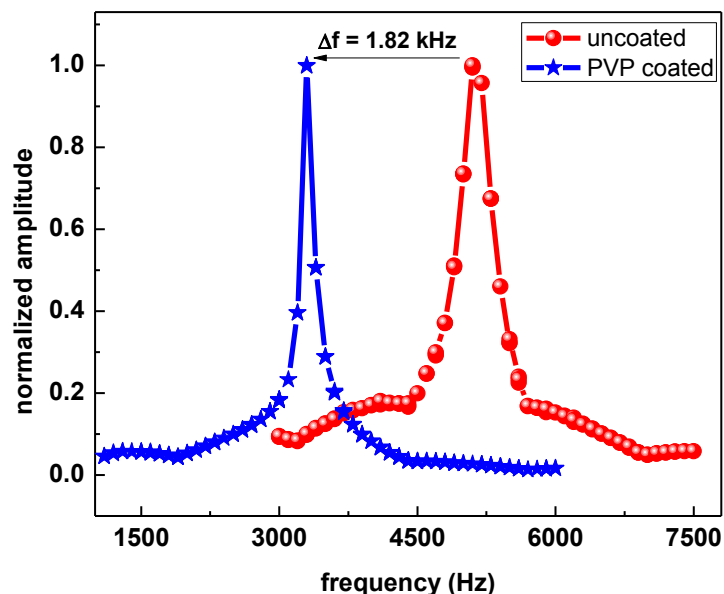


Figure 3.13 Shift in resonance spectrum of MC due to added polymer. The estimated mass due to PVP coating on MC is about 31pg using equation 1.14.

Figure 3.14 shows the change in frequency (Δf) of PVP coated and uncoated MC when irradiated to a gamma dose till 125 krad. In the case of uncoated MC, no frequency shift is observed where as in the case of PVP coated MC decrease in frequency was seen with increasing gamma dose. The frequency shift of 241.3 Hz is observed for PVP coated MC when it is exposed to 80 krad dose. The observed decrease in the resonance frequency of the PVP coated MC is related to the change in the effective Young's modulus of the PVP and silicon MC due to gamma irradiation. It was also observed that the frequency shift remains same even after several days indicating that the damage created in polymers is permanent. Q factor is also estimated from resonance frequency spectrum of PVP coated and uncoated MC at each gamma dose. The estimated Q factor with gamma irradiation is shown in figure 3.15. As expected there is no change in Q-factor for uncoated MC. Where as in PVP coated MC, Q factor slightly decreases. The decrease in Q-factor in PVP

coated MC can be corroborated to viscoelastic losses in PVP coated MC due to exposure of gamma radiation [25].

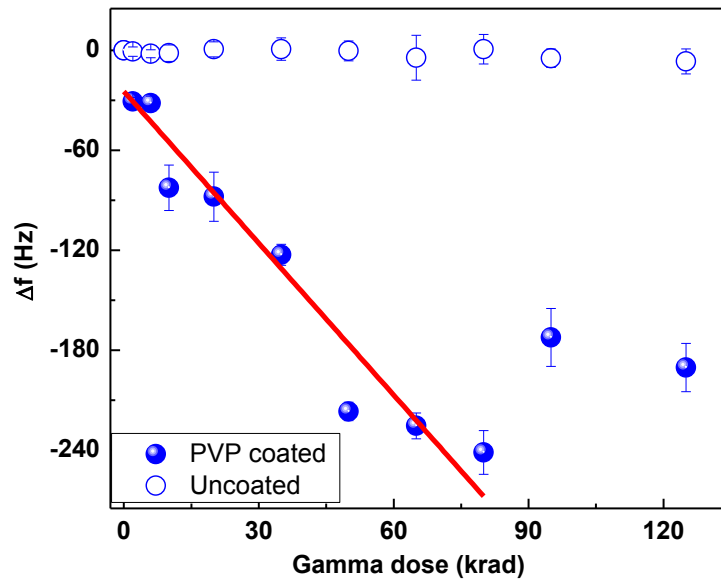


Figure 3.14 Comparison of frequency shift of PVP coated and uncoated MC when exposed to different gamma doses.

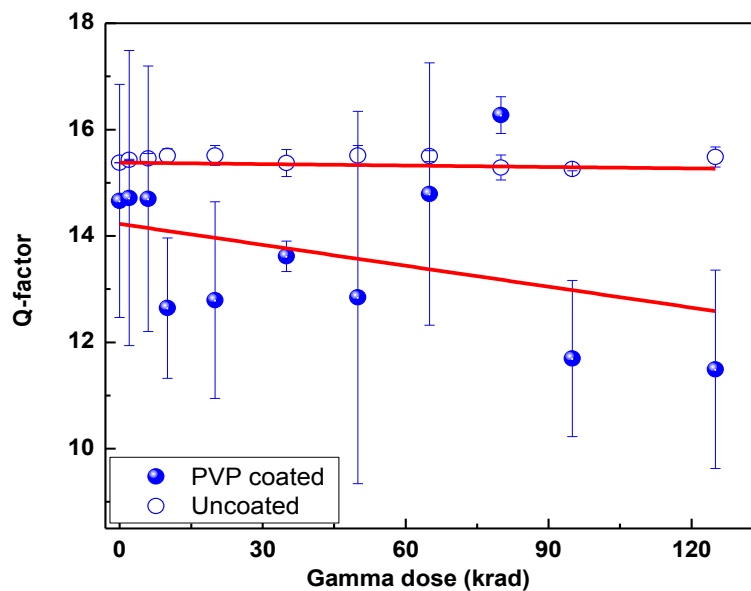


Figure 3.15 Q-factor of PVP coated and uncoated MC when irradiated to different gamma doses.

Figure 3.16 shows the AFM images of PVP after 2krad, 20krad, 50krad and 80krad gamma irradiation. The estimated RMS roughness at these doses is 0.2094 nm,

0.2211 nm, 0.2604 nm and 0.2371 nm respectively. It is evident from these values that there is slight increase in surface roughness of PVP with gamma irradiation till 120 krad.

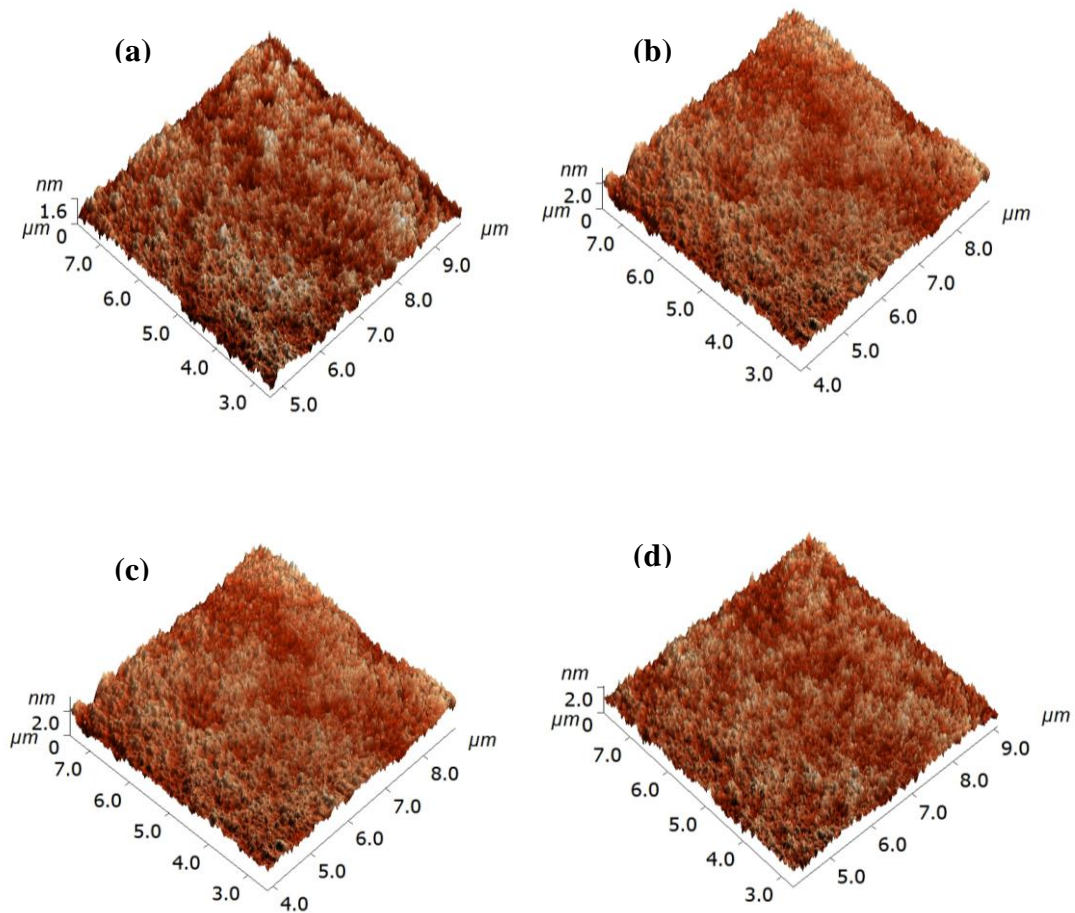


Figure 3.16 PVP surface after (a) 2 krad (b) 20 krad (c) 50 krad (d) 80 krad gamma irradiation.

In conclusion, PVP coated MC was found to show a linear decrease in natural frequency with the increasing gamma dose till 80 krad. It is to be noted that the damage created in polymers is permanent and the frequency shift remains same even after several days. It is pointed out that as there is no change in uncoated MCs with

irradiation, MC's can be reused by simply cleaning the exposed polymer and coating fresh PVP.

3.5 Conclusions

This chapter discussed some of the important aspects of cantilever based mass sensors and major conclusions are summarized below.

- It is found that mass sensitivity is proportional to the base frequency of the resonator which can be increased either by reducing the dimensions or by working at higher modes.
- Compared to fundamental mode, 7th bending mode was found to enhance the mass sensitivity from 0.0645 Hz/pg to 7.95 Hz/pg. alternatively, by reducing the dimensions of the microcantilever, 5.47 Hz/pg was achieved at fundamental mode.
- It is found that mass sensitivity increases with increase of eigen value (λ_n^2) and decreasing dimensions (T/L^2) of MC, where T and L are thickness and length of MC, respectively. It is pointed out that although mass sensitivity can be enhanced by either method, quality factor, which is an important parameter for sensor characterization, reduces after the addition of polymer mass at higher modes.
- A study based on FEM analysis, compares the mass sensitivity of three different nano structures. For given length and material, sensitivity for rectangular, solid tube and hollow tube shapes were 13 Hz/zg, 24 Hz/zg and

80 Hz/zg respectively. If the hollow tube structure would be CNT, the sensitivity would further enhance to 199 Hz/zg.

- It is also proved that mass sensitivity is dependent on the position of mass loading in CNT based mass sensors. This study points to the possibility of enhancing the mass sensitivity of nano cantilevers by physical tailoring. It is found that mass sensitivity of a conventional rectangular nanocantilever (600nm x 390nm x 100nm) enhances from 13 Hz/zg to 5117 Hz/zg when a step discontinuity along the length at 300nm is introduced.
- A millimeter sized cantilever is explored for estimating the dynamic mass range. It is found that cantilever can be effectively used as sensitive mass sensor over a wide dynamic range of 10 μ g to 10 mg.
- Demonstrated that PVP coated MC can be effectively used as gamma radiation dosimeters. Since the damage occurs only in PVP, the same Si MC can be re-used by once again coating with a fresh PVP.

3.6 References

1. T. Thundat, E.A. Wachter, S.L. Sharp and R.J. Warmack, *Appl. Phys. Lett.* 66(13), 1695-1697 (1995)
2. J. Zhang, H.F. Ji, *Analytical Sciences* 20, 585-587 (2004)
3. M. Ara, A. Sasahara, H. Onishi, Hi. Tada, *Nanotechnology* 15, S65–S68 (2004)
4. J.W. Grate, S.J. Martin, and R.M. White, “Acoustic wave microsensors,” *Analytical Chemistry*, Vol. 65, pp.940-948, 1993.
5. J.W. Grate, S.J. Martin, and R.M. White, “Acoustic wave microsensors. Part II,” *Analytical Chemistry*, Vol. 65, pp.987-996, 1993

6. I.W. Rangelow, T. Ivanov, K. Ivanova, B.E. Volland, P. Grabiec, Y. Sarov, A. Persaud, T. Gotszalk, P. Zawierucha, M. Zielony, D. Dontzov, B. Schmidt, M. Zier, N. Nikolov, I. Kostic, W. Engl, T. Sulzbach, J. Mielczarski, S. Kolb, D.P. Latimier, R. Pedreau, V. Djakov, S.E. Huq, K. Edinger, O. Fortagne, A. Almansa, and H.O. Blom, *Microelectronic Engineering*, 84, 1260-1264 (2007)
7. Y.T. Yang, C. Callegari, X.L. Feng, K.L. Ekinci, and M.L. Roukes. *Nano Letters*, 6 (4), 583-586 (2006)
8. K.L. Ekinci, and M.L. Roukes, *Rev. Sci. Instrum.* 76, 061101 (2005)
9. B. Ilic, H.G. Craighead, S. Krylov, W. Senaratne, C. Ober, and P. Neuzil, *J.Appl. Phys.* 95, 3694-3703 (2004)
10. H.G. Craighead, *Science* 290, 1532-1535 (2000)
11. M. Calleja, M. Nordstro, M.A. Ivarez, J. Tamayo, L. Lechugaa and A. Boisen, *Ultramicroscopy*, 105, 215-222 (2005)
12. Mo Li, H.X Tang and M.L Roukes, *Nature Nanotechnol.* 2, 114-120 (2007)
13. Xiaoyuan Xia, Xinxin Li, *Rev. Sci. Instrum.* 79, 074301 (2008)
14. Yihan Tao, Xinxin Li, Tiegang Xu, Haitao Yu, Pengcheng Xu, Bin Xiong, Changzheng Wei, *Sens. Actuators B* 157, 606-614 (2011)
15. L. B. Sharos, A. Raman, S. Crittenden, and R. Reifenberger, *Appl. Phys. Lett.*, 84, 4638 (2004)
16. J. W. Yi, W. Y. Shih and W.H. Shih, *J. Appl. Phys.* 91, 1680-1686.
17. M. K. Ghatkesar, V. Barwich, T. Braun, J.-P. Ramseyer, C. Gerber, M. Hegner, H. P. Lang, U. Drechsler, M. Despont, *Nanotechnology* 18, 445502 (2007)
18. F. Lochon , I. Dufour and D. Rebiere, *Sens. Actuator B*, 108, 979-985 (2005)
19. M. Narducci, E Figueras, M.J. Lopez, I. Gracia, J. Santander, P. Ivanov, L. Fonseca, C. Cane, *Microelectronic Engineering* 86, 1187-1189 (2009).
20. R Sandberg, K Molhave, A Boisen and WSvendsen, *J. Micromech. Microeng.* 15, 2249-2253 (2005)
21. S. S. Rao, *Mechanical Vibrations*, Pierson publications, Fourth edition, 2004.
22. J. E. Sader, J. W. Chon and P. Mulvaney, *Rev. Sci. Instrum* 70, 3967–3969 (1999).

23. N. Yin and K. Chen, *Polymer* 45, 3587-3594 (2004)
24. I. Dufour, F. Lochon, S. Heinrich, F. Josse, and D. Rebiere, *IEEE Sensors J.*, 7, 230–236 (2007).
25. A. K. Naik, M. S. Hanay, W. K. Hiebert, X. L. Feng and M. L. Roukes, *Nat. Nanotechnol.* 4, 445 (2009)
26. M. Li, E. B. Myers, H. X. Tang, S. J. Aldridge, H. C. McCaig, J. J. Whiting, R. J. Simonson, N. S. Lewis and M. L. Roukes, *Nano Lett.* 10, 3899 (2010)
27. S. Schmid, S. Dohn and A. Boisen, *Sensors* 10, 8092 (2010)
28. K. L. Ekinici and M. L. Roukes, *Rev. Sci. Instrum.* 76, 061101 (2005)
29. B. Ilic, H. G. Craighead, S. Krylov, W. Senarantne, C. Ober and P. Neuzil, *J. Appl. Phys.* 95, 3694 (2004)
30. S. Iijima, *Nature* 354, 56-58 (1991)
31. R. S. Ruoff, D. Qian, W. K. Liu et al., *C. R. Physique* 4, 993-1008 (2003)
32. A. Y. Joshi, S. C. Sharma and S. P. Harsha, *Sens. Actuator A* 168, 275 (2011)
33. I. Mehdipoura, A. Bararib and G. Domairryc, *Comput. Mater. Sci.* 50, 1830 (2011)
34. X. Y. Wang and X. Wang, *Composites B* 35, 79 (2004).
35. D. H. Wu, W. T. Chien, C. S. Chen and H. H. Chen, *Sens. Actuator A* 126, 117 (2006)
36. S. Dohn, W. Svendsen, A. Boisen and O. Hansen, *Rev. Sci. Instr.* 78, 103303 (2007)
37. S. Dohn, R. Sandberg, W. Svendsen and A. Boisen, *Appl. Phys. Lett.* 86, 233501 (2005)
38. K. Prabakar, J. Jayapandian, A. K. Tyagi, C. S. Sundar and B. Raj, *Nano* 5, 25 (2010).
39. N Kacem, J Arcamone, F Perez-Murano and S Hentz, *J. Micromech. Microeng.* 20, (2010) p. 045023
40. T. Thundat, S.L. Sharp, W.G. Fisher, R.J. Warmack, and E.A. Wachter, *Appl. Phys. Lett.* 66 (12), 1563 (1995)
41. P. G. Datskos, S.Rajic, and I. Datskou, *Ultramicroscopy* 82, 49-56 (2000)
42. E.A. Wachter, T. Thundat, P.I. Oden, R.J. Warmack, P.G. Datskos, and S.L. Sharp, *Rev. Sci. Instru* 67, 3434–3439 (1996)

43. J. Steinbock Lorenz, and Mark Helm, *Sensors* 8, 23-34 (2008)
44. A.C. Stephan, T. Gaulden, A.D. Brown, and M. Smith, L. F. Miller and T. Thundat, *Rev. Sci. Instrum.* 73, 1 (2002)
45. H.R. Shea, *J. Micro/Nanolith. MEMS MOEMS* 8(3), 031303 (2009)

Chapter 4 - Adsorption of water molecules on uncoated Si microcantilevers

This chapter investigates the static and dynamic response of uncoated silicon microcantilever (MC) during adsorption of water molecules. The resonance frequency shift upon adsorption of water molecules in MCs with reducing dimensions is investigated. AFM head placed inside an air tight chamber, purged with dry/wet N₂ was used for these studies. Experimental evidence is presented to show that the effect of dimensions of MC leads to negative or positive frequency shift during adsorption, clearly depicting the competition between mass loading and stiffness changes. The relative change in stiffness of MC is seen to increase linearly with the surface stress scaled with cube of width to height ratio of MCs, confirming the dimensional dependence of adsorption induced stiffness change. Adsorption and desorption kinetics of water molecules on MC surface is studied. Apart from this, various possible mechanisms responsible for deflection of uncoated Si MC when exposed to water molecules is discussed. It is shown that the bending is a consequence of difference in surface roughness on front and back side of uncoated MCs. The results are explained in terms of the large number of “stress concentrators” on the back side compared to front side of MC in accordance with the recent theoretical models [1, 2]. Finally it is demonstrated that uncoated MCs can be effectively used as a humidity sensor both in static and dynamic mode.

4.1 Influence of adsorption induced surface stress on stiffness changes of microcantilevers

4.1.1 Literature survey

Measurement of adsorbed mass on microcantilevers results in resonance frequency decrease, and this offers one of the most sensitive mass sensing techniques, approaching single molecule detection [3]. Although, naively one would expect the frequency shift to be proportional to the square root of the added mass, there are several other mechanisms like non-uniform mass loading [4], flexural rigidity of the adsorbate [5], surface stress [6], surface elasticity [7], etc which will influence the stiffness of the cantilever, making the mass measurement qualitative.

Resonance frequency shifts in MCs are known to depend sensitively on both mass and stiffness variations induced by the adsorbed atoms/molecules [8]. The role of surface stress on the resonance behavior of a structure was studied experimentally and theoretically [9, 10]. However, there is minimal understanding of how surface stress influences the resonance frequency of a cantilever. Numerous studies over the past 35 years have claimed that surface stress can cause significant variations in device stiffness [5, 11, 12 - 16]. Bashir and coworkers [7] first showed that biomolecular adsorption increases the resonant frequency of an ultrathin cantilever, which had a thickness of less than 100 nm. This finding contradicts the conventional detection principle [11, 17-19] for mass sensing, and is attributed to the fact that the resonant frequency shift is controlled by the elastic stiffness of adsorbed biomolecular monolayer rather than the added mass. Tamayo et al [5] reported that the frequency response of a MC depends on the flexural rigidity change that results from stiffness of the adsorbate. Their model predicts that if thickness ratio of

adsorbate to MC is less than 0.04 the resonance frequency decreases approximately linearly, indicating that mass effect dominates for small thickness of adsorbate. It is found that, when the adsorption occurs at the clamped end, the resonant frequency shift is determined by the stiffness of adsorbed molecules (or virus or a single cell), whereas the mass effect is dominant in the frequency shift for the adsorption at the free end. This is consistent with theoretical model proposed by them. Various microbeam models have been proposed to explain adsorption-induced surface stress change and its resultant resonance frequency shift or deflection of a microbeam in vacuum or in gaseous environment [20-23]. Although many theoretical models have been proposed to explain this phenomenon [23-26], the influence of MC dimensions on the same are complicated and needs more comprehensive understanding. Only few investigators have addressed this problem [27, 28]. Lachut et al [28] developed a 3D model relating stiffness changes in MC with different dimensions and total strain independent surface stress (σ_T^s) generated. According to this model, MC generates a net in plane stress in the immediate vicinity of the supporting clamp during adsorption thereby affecting the stiffness. This effect will be dominant when length by width ratio of the MC reduces. But, as pointed out by Qiao et al [29] this model does not consider strain dependent surface stress and may not explain the experimental results. In yet another interesting work, McFarland et al [12] developed a model to predict the effect of surface stress upon resonant frequencies for higher modes of MC and validated with their theory with experimental results. However, no experimental work is reported in the literature on the effect of MC dimensions on its stiffness changes during adsorption.

In the present work, experimental evidence is presented to show that the effect of dimensions of MC leads to three distinct behaviors clearly depicting the competition between mass loading and stiffness changes. The expected frequency shift due to the added mass on MC surface is numerically estimated and compared it with experimental results. Difference between the observed and calculated is attributed to the stiffness change of the MC due to adsorption. The estimated stiffness change is corroborated with measurements of the surface stress generated during adsorption, through bending measurements.

The details of MCs studied in this work are presented in table 2.1 and experimental setup used for water adsorption studies on MC is presented in detail in section 2.4 of Chapter 2.

The unloaded resonance frequency, ' f_1 ', of an oscillating MC is given by

$$f_1 = \frac{1}{2\pi} \sqrt{\frac{k}{m^*}} \quad (4.1)$$

where ' k ' is the spring constant and ' m^* ' is the effective mass of the MC. When adsorbates are deposited uniformly on the cantilever surface, the resonance frequency ' f_2 ', given by,

$$f_2 = \frac{1}{2\pi} \sqrt{\frac{k + \Delta k}{m^* + \Delta m}} \quad (4.2)$$

where, ' Δm ' and ' Δk ' are the changes in mass and spring constant respectively due to adsorption.

The equation 4.2 can be expressed in terms of f_1 is given by

$$f_2 = f_1 \sqrt{\frac{k + \Delta k}{k}} \sqrt{\frac{m^*}{m^* + \Delta m}} \quad (4.3)$$

It is evident from equation (4.3) that if $\Delta k = 0$, added Δm will always results in negative frequency shift ($f_2 < f_1$) which is the case with equation 1.11 in chapter1.

4.1.2 Results and Discussions

Figure 4.1 shows the relative resonance frequency shift of MC1, MC2 and MC3 (see Table 2.1 of chapter 2) as a function of increasing RH i.e., during physisorption of water molecules. Dramatically different behaviors are seen from this figure for the three MCs: For the cantilever MC1, the frequency decreases with added mass, as would be expected, but whereas for MC2 and MC3, the frequency hardens initially with the added mass. At higher mass loading, in the case of MC2, the frequency decreases. These trends clearly indicate that the observed frequency change is a combination of both the mass loading and stiffness change during the adsorption of water [6].

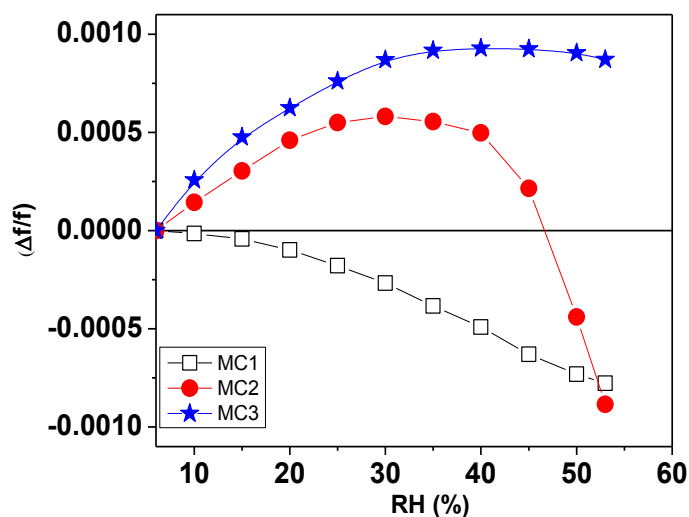


Figure 4.1 Relative shift in resonance frequency with increasing RH in MC1, MC2 and MC3.

In order to discriminate the contribution of each of these two effects, we have numerically computed the frequency shift due to added mass on MC surface. Assay and Kim [30] through infrared experiments have studied the relation between the adsorbed water layer thickness and RH for SiO_2 surface and is shown in figure 4.2(a).

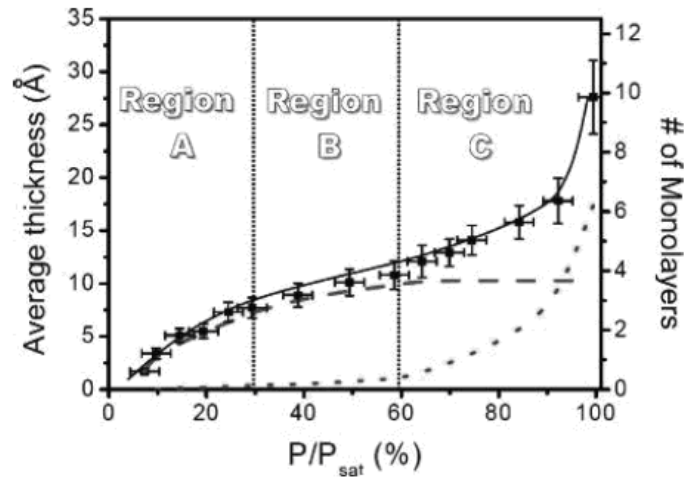


Figure 4.2 (a) Adsorption isotherm of adsorbed water on the SiO_2 surface taken from [30]. Square symbols in this figure are the total thickness of the adsorbed water layer calculated from the intensity of H-O-H bending vibration peak.

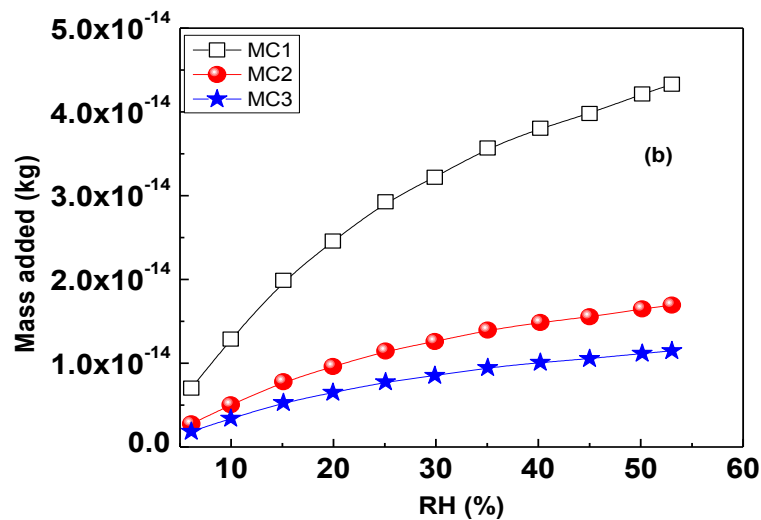


Figure 4.2 (b) Estimated mass on three MCs with increasing RH. Water layer thickness on SiO_2 surface was taken from Assay and Kim data [30] and density of water was taken as 1000 kg/m^3 .

We have evaluated the added mass Δm on three MCs studied in the present work with increasing RH, by assuming the thickness of water layer at each RH from 4.2 (a) and multiplying with density of water (1000 kg/m^3) and dimensions of surface and these are shown in figure 4.2 (b).

The expected frequency shift, due to added mass alone, for each MC is calculated by substituting $\Delta k = 0$ in equation (4.3), wherein the effective mass $m^* = 0.24\rho V$ [6], and ' ρ ' and ' V ' are density of silicon and volume of the MC respectively. The difference between the observed frequency shift (cf. Fig. 4.1) and calculated as above, is converted into to the variation in spring constant (Δk) for all the MCs.

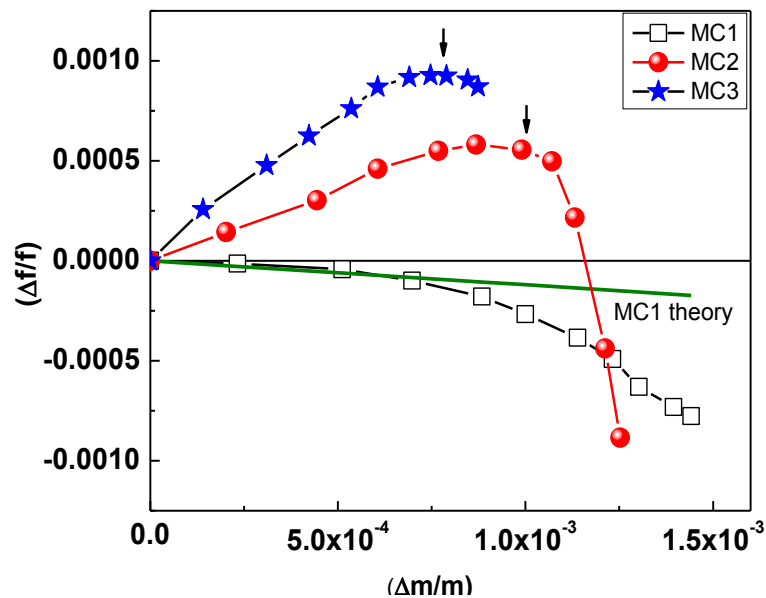


Figure 4.3 Relative shift in resonance frequency with relative mass on three MCs. This figure also shows the estimated frequency shift in MC1.

Figure 4.3 shows the relative frequency shift with respect to relative mass ($\Delta m/m$) of MCs during adsorption. This figure also shows the estimated frequency shift for MC1. In the case of MC1, measured and estimated frequency shift coincides

initially, indicating the adsorption induced stiffness changes is negligible i.e. the assumption of $\Delta K = 0$ is valid. However, the deviation at higher added mass may be due to the formation of continuous water film on MC surface at high humidity regime [31]. In MC2 and MC3, the positive frequency shift during initial stages is clearly due to the adsorption induced stiffness change i.e. the assumption of $\Delta K = 0$ is not valid here. Also, the change in the direction of $(\Delta f/f)$ in MC2 and MC3 (shown by arrow marks) indicates the change from “stiffness dominated effect” to “mass dominated effect”.

Figure 4.4(a) shows the computed relative change in stiffness $(\Delta k/k)$ for three MCs with added mass per unit area (surface density). From this figure it is clear that $(\Delta k/k)$ is maximum in MC3 and as expected is negligible for MC1. The observed $(\Delta k/k)$ arises due to the surface stress generated during adsorption. To estimate the surface stress, MC bending measurements were carried out. It is performed using the same set up after the resonance frequency measurements. The photo diode signal was converted into MC deflection (Δz) using the method discussed in section 2.3 of chapter 2. From the deflection (Δz) , differential surface stress $(\Delta \sigma)$ is estimated using Stoney’s equation given by [6],

$$\Delta \sigma = \frac{ET^2}{3(1-\nu)L^2} \Delta z \quad (4.4)$$

where, ‘E’ is Young’s modulus, ‘ ν ’ is Poisson’s ratio and ‘L’ and ‘T’ are length and thickness of the MC used. The differential surface stress $(\Delta \sigma)$ generated during adsorption with surface density in all the MCs is shown in figure 4.4(b). In Fig. 4.4(c), we plot $(\Delta k/k)$, as obtained from Fig. 4.4(a) with $\Delta \sigma$, as obtained above.

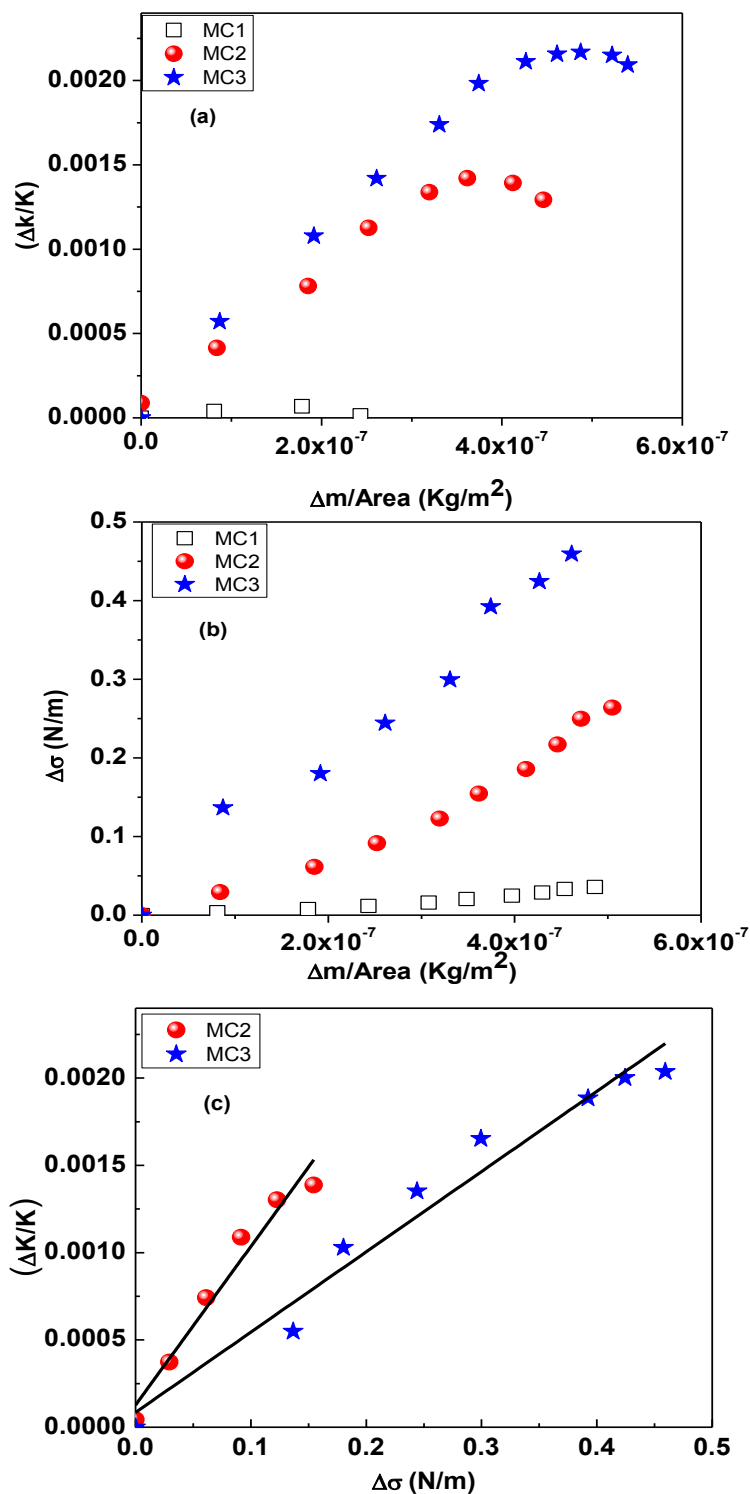


Figure 4.4 (a) Variation of stiffness change with respect to mass per unit area of three MCs. This was estimated by converting the difference of fig.4.1 and 4.2(b) as Δk using equation 4.3. (b) Surface stress generated during adsorption in all the MCs with respect to mass per unit area. This was estimated from cantilever bending data using Stoney's equation. (c) Linear fit of $(\Delta k/k)$ with $(\Delta\sigma)$ in MC2 and MC3.

A linear correlation between the change in stiffness constant and the measured change in surface stress due to adsorbed water is clearly seen for the smaller cantilevers MC2 and MC3, in which a positive frequency shift is observed with added mass (cf. Fig. 4.3). We attribute these experimental observations to the in-plane stress generated during adsorption at fixed end of MC i.e. clamping effect [28]. Clamping exerts reaction forces to cancel out the curvature induced by the bending moment during adsorption. It must be emphasized that MCs are rigidly clamped to a chip substrate and does not participate in the vibration during dynamic measurements. This results in non uniform curvature at fixed end there by increasing the stiffness of MC which will be dominant when MC dimensions reduce [27].

Lachut et al [28] have pointed out that the resonance frequency change of a MC is dictated by the ratio of the surface stress and a stiffness parameter given by $K_{\text{ref}} = ET^3L/W^3$. While the above model, estimates orders of magnitude larger surface stress, than is seen experimentally, we take their dimensional dependencies. It is to be noted that in this model, the change in dimensions of length has a relatively weaker effect as compared to the change in width or thickness. Taking these aspects into consideration, we plot in Fig. 4.5, $(\Delta k/k)$ vs $\Delta\sigma(W/T)^3$, and it is seen that data for MC2 and MC3 collapse into a single curve unlike in figure 4.4 (c).

This clearly indicates that the stiffness changes are proportional to both surface stress generated during adsorption and dimensions, particularly the width and thickness, of the MC under consideration. However, more detailed and systematic experiments on the effect of aspect ratio, surface area etc., are needed to evaluate the dimensional dependence of stiffness changes in MCs during adsorption.

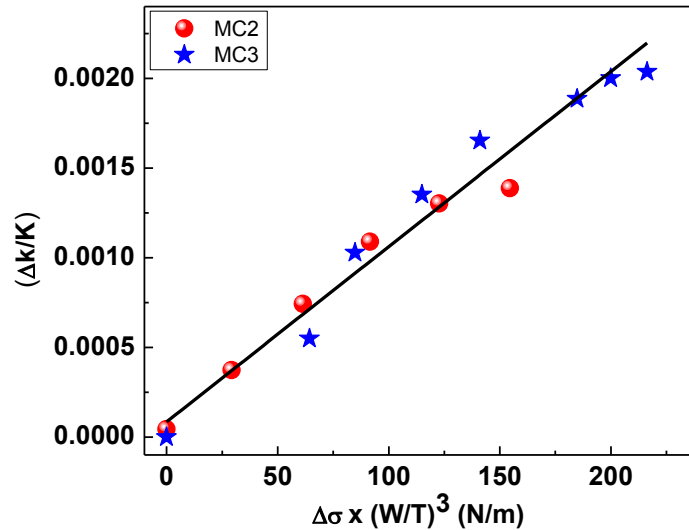


Figure 4.5 $(\Delta k/k)$ Vs $(\Delta\sigma)$ scaled to $(W/T)^3$ ratio in MC2 and MC3. Collapsing of the data in this figure is the experimental evidence for the dependence of stiffness changes during adsorption to surface stress and MC dimensions.

The results indicate that MC1 can be used as humidity sensor. The sensitivity is estimated from observed frequency shift is found to be 0.18 Hz/%RH for VB1 when RH is varied from 50% to 6%. This sensitivity can be enhanced by working at higher modes of vibration of MC.

4.2 Higher modes of vibration of Si microcantilever for humidity detection

Figure 4.6 shows resonance frequency shift of (a) VB1 and (b) VB7 modes of vibration of MC1 when RH is varied from 50% to 6%. It is observed from the figures that the frequency shifts for VB1 and VB7 are 8 Hz and 2.12 kHz respectively. The sensitivities are estimated as 0.18 Hz/%RH and 48 Hz/%RH for VB1 and VB7 respectively. The changes in resonance frequency of other modes torsional (TB) and lateral bending (LB) modes as a function of RH is also studied and compared to fundamental mode responses.

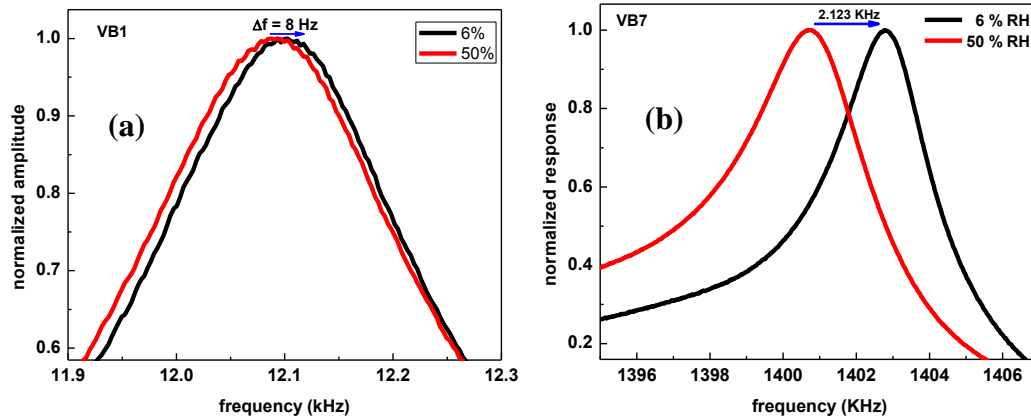


Figure 4.6 The frequency shifts for (a) VB1 and (b) VB7 modes of vibration of MC1 for the change of RH from 50% to 6%.

Table 4.1 shows the resonance frequency (f_1) measured at 50 % RH and shift in frequency (Δf) when RH was reduced to 6 % for MC1 in three different modes. It is clear from the table that compared to VB1, VB7 is more sensitive to RH change and is due to increase in base frequency.

TABLE 4.1 Resonance frequency (f_1), shift in frequency (Δf) and sensitivity of various modes of vibration of MC1 when RH is varied from 50 % to 6%.

Modes	f_1 (KHz)	Δf (Hz)	Sensitivity (Hz/%RH)
VB1	12.092	8	0.18
VB7	1400.4	2123	48
LB1	198.51	255	5.7
TB1	311.1	240	5.4

4.3 Adsorption and desorption kinetics of water molecules on uncoated microcantilever

Now, a method that exploits dynamic and static mode of MCs to measure the adsorption-desorption kinetics of water molecules onto exposed Si surfaces is presented. The time evaluation of adsorption and desorption of water molecules from a Si surface exposed to the vapors is followed using the variation in the resonant frequency and bending of the MC. During adsorption, the resonant frequency of the cantilever decreases due to an increase in mass while the resonant frequency of the cantilever increases during desorption since the total mass associated with the cantilever decreases. Depending on mass loading on MC, rate constant for desorption of water molecules is calculated. The obtained rate constant for desorption is used to estimate the activation energy for desorption of water molecules. Surface stress variation with time is fitted to Langmuir isotherm and is proportional to number of excess adsorbed molecules on back side of the cantilever. Information obtained from this study can be vital in the design of sensors to be used for the detection of water molecules.

All these studies are performed on MC1, where adsorption induced stiffness changes are minimum. The experimental setup used for this study is given in chapter 2. The RH vs time information is also recorded.

4.3.1 Kinetics during dynamic mode

Figure 4.7 shows the variation in resonant frequency of the MC1 as a function of time when its surface was exposed to water vapor. Relative humidity in the chamber was varied from 50% to 6% and vice versa shown as open circles in the figure. Note

that the frequency increases as a function of time when reducing the RH from 50% to 6% and that the frequency changes rapidly over a period of 12000 seconds. This increasing in frequency can be attributed to decrease in the total MC mass, showing clearly that water desorbs from MC surface. In the adsorption case (i.e from 6% to 50%), frequency decreases as a function of time and that the frequency changes rapidly over a period of 6000 seconds. This lowering in frequency can be attributed to an increase in the total cantilever mass, showing clearly that water adsorbs and sticks to the cantilever surface.

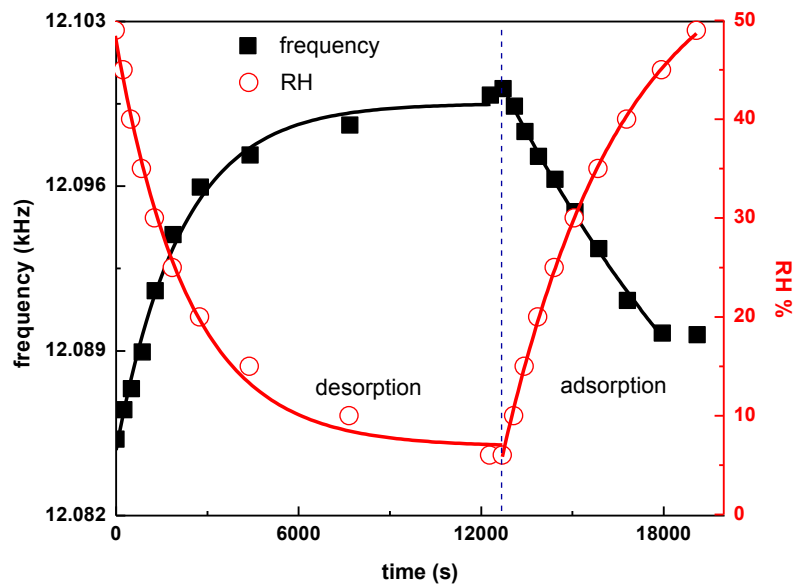


Figure 4.7 Variation in the resonant frequency of MC1 and the relative humidity as a function of time.

The frequency change can be correlated to a change in mass using the Eq. 1.14 in chapter 1. From the observed frequency shift at various RH value (f_2), with respect to its value at 6% / 56% RH (f_1), the added / removed mass was estimated.

Figure 4.8 (a) and (b) shows the variation in frequency and desorbed mass/adsorbed mass as a function of time during desorption/adsorption.

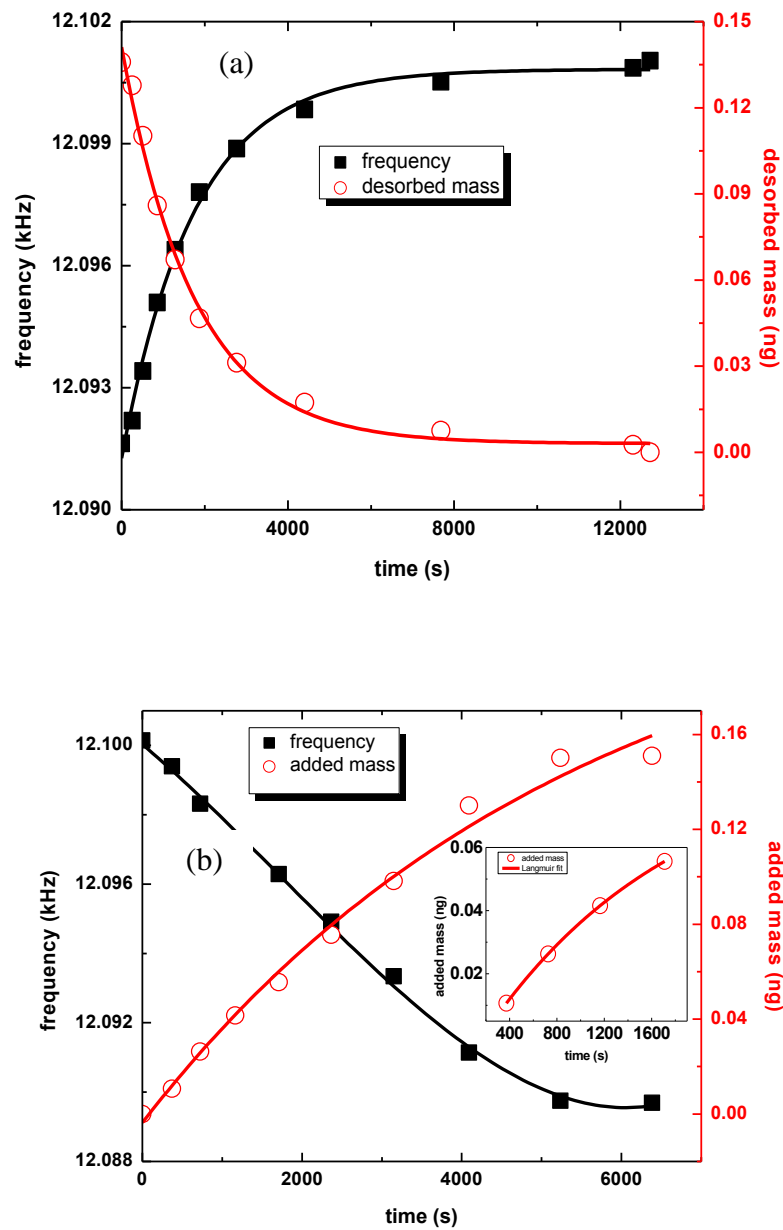


Figure 4.8 Variation in the resonant frequency of the microcantilever and desorbed/adsorbed mass as a function of time (a) during desorption and (b) adsorption of water molecules. Desorption is fitted to single exponential decay with rated constant of 0.000573. Initial adsorption is well fitted to Langmuir fit as shown in inset in 4.8 (b).

In figure 4.8 (a), the time desorption data fitted to a single exponential decay model well. The single exponential decay conforms to the relationship

$$y = 0.00304 + 0.1431 \exp(-0.000573 * t) \quad (4.4)$$

It is important to note that the desorption kinetics varies exponentially rather than linearly with time. The possible explanation for the non-linear relationship is that the surface coverage is complex (dispersed islands of water), and the rate of desorption which would be expected to be proportional to the total surface area of water, does not vary linearly with time for a constant rate of loss of water [32].

From the total mass change estimated during desorption from figure 4.8 (a) and assuming 4 mono layers of water molecules on each side of MC, we estimate the mass of monolayer of water molecules to be 16.9 pg. Now, from the total surface area of MC ($3.6 \times 10^{-4} \text{ cm}^2$) and for a surface site density of 10^{15} cm^{-2} one can convert desorption rate of 0.5 pg/s into 5.3×10^9 molecules/sec. Desorption rate is expected to follow an Arrhenius-type behavior with a rate coefficient, k_d , given by,

$k_d = A \exp\left[\frac{-E_a}{NkT}\right]$, Where E_a is the heat of adsorption, N is Avogadro's constant ($6.02 \times 10^{23} \text{ mol}^{-1}$), k is Boltzmann's constant ($1.38 \times 10^{-23} \text{ JK}^{-1}$), T is the temperature (297 K) [33]. The pre-exponential factor A is a vibrational frequency of the weak molecule-surface bond of the order of 10^{12} s^{-1} . By substituting these values and k_d as 5.3×10^9 molecules/sec, we calculated the activation energy to be $12.94 \text{ kJ mol}^{-1}$ which corresponds to the desorption of weakly held higher adsorbed layers and is a measure of $\text{H}_2\text{O}-\text{H}_2\text{O}$ interactions [34]. It may be noted the desorption activation energy is an average property which depends on the extent of coverage and the distribution of adsorbed molecules among different layers.

The added mass of water molecules as a function of time during adsorption is shown in figure 4.8 (b) in open circles. It is interesting to note that the rate of adsorption show two regimes. The initial adsorption is well described by a Langmuir model

given by the equation $y=0.2326 \{1- \exp (-0.000183*t)\}$ and is shown in inset of figure 4.8 (b). At higher adsorption times, Langmuir like behavior is deviated. It is believed that at this stage there is more than a monolayer of water on the surface of the cantilever and hence represents multilayer adsorption. A simple calculation based on the adsorbed mass shows that for the range of mass measured in this study, the process is more likely to be multilayer rather than monolayer adsorption.

4.3.2 Kinetics during static mode

Figure 4.9 shows the deflection response of uncoated MC1 as a function of time during desorption and adsorption of water molecules.

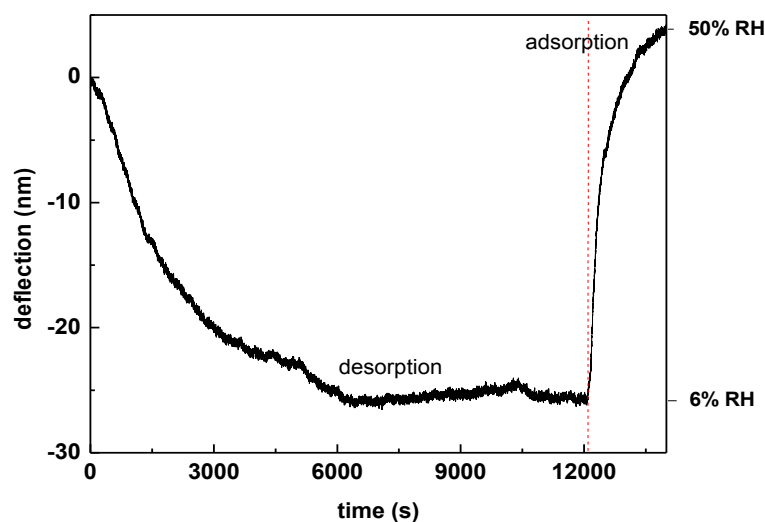


Figure 4.9 Variation of deflection of the MC as a function of time during desorption and adsorption of water molecules

From the deflection data of the adsorption-desorption cycle, differential surface stress was estimated using Stoney's equation and is plotted as a function of time during desorption and adsorption of water in figure 4.10 (a) and (b). Time

dependence of surface stress during desorption fits well to single exponential decay with a rate of 0.00051s shown in figure 4.10 (a). This rate corresponds to the number of extra water molecules desorbing from back side of MC.

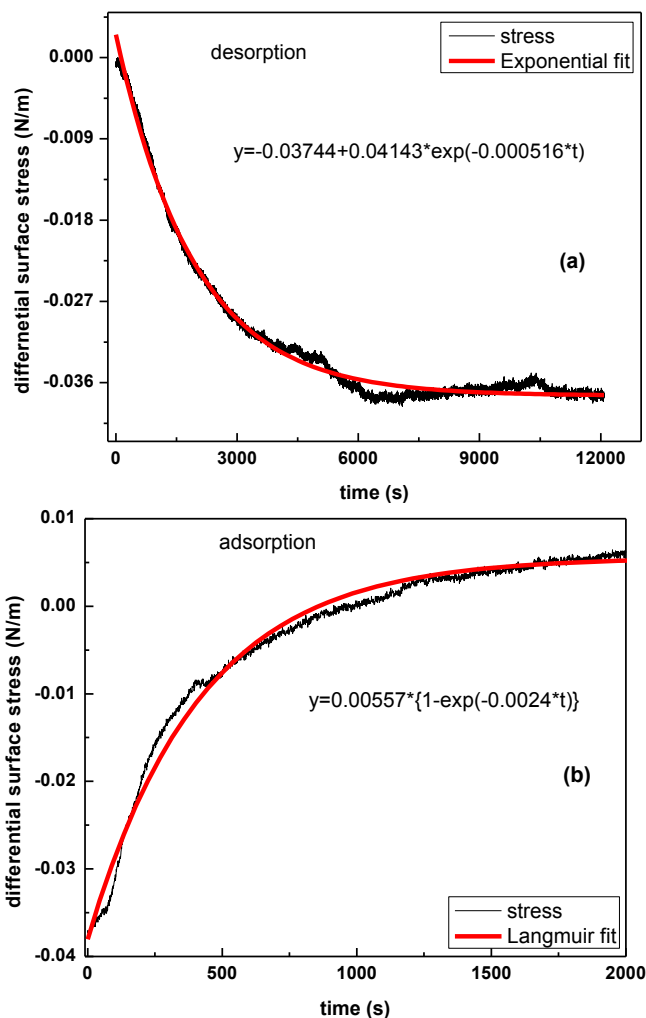


Figure 4.10 Differential surface stress estimated from deflection of the MC during (a) desorption and (b) adsorption of water molecules. Adsorption and desorption data fits to Langmuir isotherm and single exponential decay respectively.

Surface stress variation during adsorption was found to follow Langmuir model shown in figure 4.10 (b). This implies that surface stress generated is proportional to the number of excess adsorbed molecules on back side of the cantilever. The

experimental data was fit to this model using non-linear curve fitting method and the k was estimated to be 0.0024 s^{-1} .

In conclusion, we have studied the adsorption and desorption of water vapors from MC surfaces. We have estimated the activation energy for an uncoated MC1 from the mass data and was found to be 12.0 kJ mol^{-1} . This confirms the adsorption of water on silicon microcantilever was multilayer adsorption. Surface stress variation during adsorption was found to follow Langmuir isotherm with a rate constant of 0.0024 s^{-1} . This indicates that the surface stress generated is proportional to the number of excess water molecules adsorbed on back side of the MC.

4.4 Stress concentrators as origin of uncoated microcantilever bending

4.4.1 Literature survey

The bending of MC has been a subject of study in the context of evolution of fundamental material parameters such as surface stress during adsorption on exposure to analytes etc [26, 35, 36]. These experiments hinge strongly on the basis of Stoney's equation, where the bending of MC is associated with the magnitude of change in surface stress [37]. However, the application of Stoney's equation warrants a planar surface, which is in contrast to real surfaces possessing a corrugation either due to intrinsic nature of formation or during deposition. Several experimental studies reported in literature show a strong tendency of the enhancement [38-42] and otherwise [43, 44], on the cantilever response to surface features upon adsorption. Lavrik et al [38] compared the deflection sensitivity of MCs with different surface roughness and concluded that it enhances when surface roughness increases. However, Godin et al [43] found that MC with rough surface

deflects less compared to smooth surface and attributed it to the formation of incomplete mono layers during molecular adsorption. In a similar study, Desikan et al [44] did not observe any significant increase in surface stress and thus deflection of MC due to increase in surface roughness.

Weissmuller and Duan [2] theoretically characterized the implications of surface roughness on adsorption of analytes in terms of its geometry and molecular interaction. It is shown in ref. [2] that in plane component of the mean surface stress is only weakly affected by roughness, while the out of plane stress component couples to the tangential stress due to transverse contraction. Further, the sensitivity of the cantilever and the sign of bending strongly depended on the mean square surface inclination angle $\langle\theta^2\rangle$ (related to experimentally measurable RMS roughness (ρ) by, $\rho \approx 1 + \frac{1}{2}\langle\theta^2\rangle$), and the Poisson's ratio of the surface. In a recent report, Hayden et al [1], performed the computation analysis of the effect of surface roughness on the deflection of a gold coated silicon MC, and showed that the adsorption induced deflection increases with increasing roughness despite the decrease in the number of bonding sites.

However, these studies [1, 2, 38-44] have been carried out on gold coated MCs, where it is known that passivation leads to enhanced sensitivity. It is well established that on passivation or functionalization, the surface stress is enhanced due to the differential molecular adsorption between opposite sides of a MC. However, the gold coated MCs lead to poor reproducibility of results and the properties of gold significantly influence the response of the MCs [41]. Another

shortcoming with gold coating / passivation is, it often introduces a gradient of mechanical stress which results in an initial undesired bending of MCs. Keeping this in mind, there are attempts to directly modify the Si surface, like fabrication of porous silicon cantilevers [45] to enhance the sensitivity. Our approach, however, consists of working with commercially available uncoated MCs having sides that are structurally different. This idea is based on the fact that the larger surface roughness on back side compared to front side of uncoated MCs is expected during bulk microfabrication. Incidentally, dynamic mode operation of MCs without sensitive coating is already explored to enhance the mass sensitivity [46].

In the present thesis, we demonstrate that uncoated MCs with inherently different topologies on opposite sides of MC can be as sensitive as passivated ones, which is evidenced from our bending measurements upon water adsorption. Experiments are performed on two commercial MCs - one having different roughness and another of comparable roughness on opposite sides, resulting in bending and non bending, respectively. Experiments are also performed to prove that the observed deflection is not an artifact. It is shown that the inherent difference in the localized areas of increased stress or ‘stress concentrators’ on the opposite sides of MC is responsible for the large deflection validating the recent theoretical models [1, 2]. We report the first experimental evidence to show that stress concentrators indeed play an important role in bending and hence in sensitivity of the MCs.

The details of MCs used in this study are presented in table 2.1 of chapter 2. The water desorption / adsorption and subsequent bending of MC is studied using an experimental setup presented in section 2.4 of chapter 2.

4.4.2 Results and discussions

Figure 4.11 shows the deflection response of MC1 when laser is focused on the back side of the MC1 during four representative desorption-adsorption cycles when RH is switched between 50 and 6%. It is evident from this figure that the switching is repeatable and the deflection is positive (bending backwards) during desorption with a magnitude of ~ 450 nm during each switching sequence.

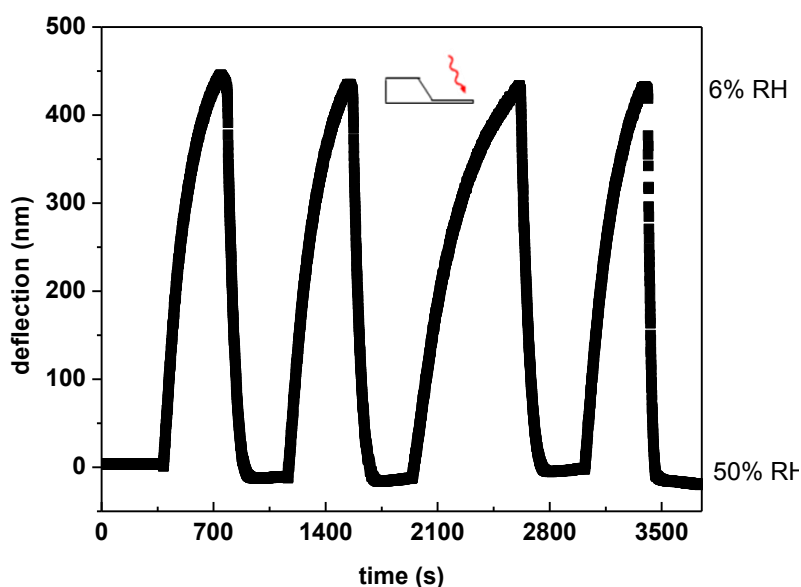


Figure 4.11 Deflection response of MC1 for four adsorption-desorption cycles when RH switched between 50% to 6%. Laser was focused on back side of MC1.

In order to establish that the MC bending is not an artifact, two approaches are adopted. One, experiments were conducted by recording deflection data from both the front and back side of the MC1, varying the RH under similar experimental conditions as shown in figure 4.12 (a) and (b). The direction of focusing of incident laser on MC1 is shown as inset in these figures. This figure clearly shows that the deflection of the MC is in opposite directions with comparable magnitudes.

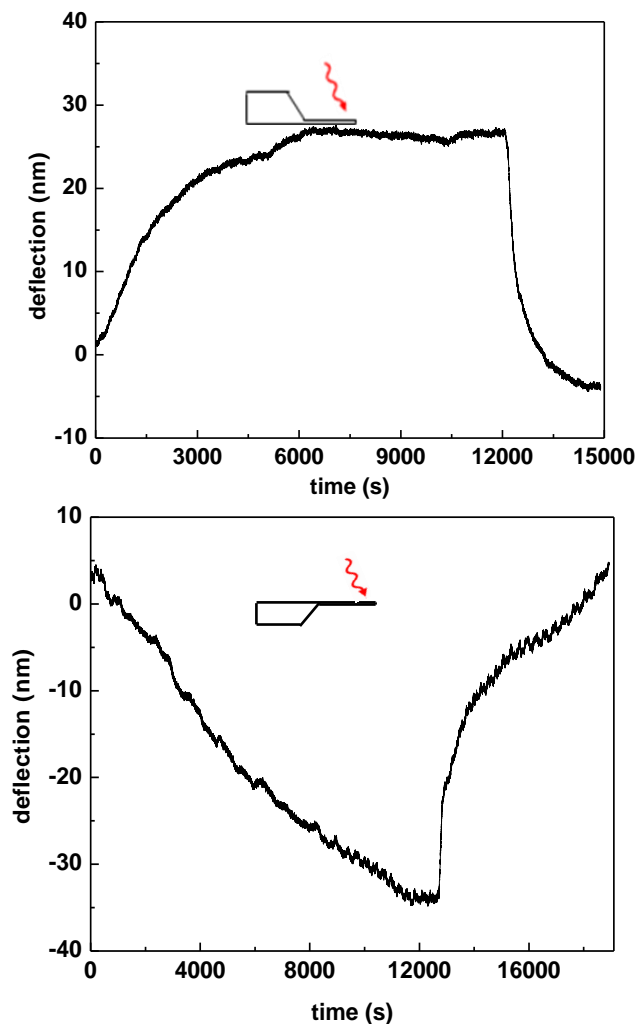


Figure 4.12 Long time deflection response of MC when laser is focused on (a) back and (b) front surface of MC1.

Two, in order to understand if the bending could arise due to the continuous incidence of laser on MC, the temperature changes during the experiments was monitored. The rise in temperature in the chamber was $\sim 3^{\circ}\text{C}$ during RH change from 50 to 6%. The quantum of bending for 3°C rise in temperature was computed following the procedure outlined in ref [25], in which water adsorption is considered to occur on a bimaterial (SiO_2 on top of Si). By assuming a 5 nm native silicon dioxide layer and 4 monolayers of water (typically 1 nm) on silicon surface, the

expected deflection was computed to be about 1.4 nm and 2.3 nm, respectively. These results confirm that MC is indeed bending during adsorption and is not an experimental artifact.

It is well known that confined adsorption of molecules on one side of MC results in upward or downward bending, depending on the tensile or compressive stresses generated, respectively. Since the MC used here is uncoated, it is expected that the surface stress generated during adsorption or desorption should be equal on both sides and therefore, the resultant differential stress should be zero, thereby leading to no bending. Taking a clue from the theoretical work of Weissmuller and Duan [2], the surface topology in terms of inclination angle on opposite sides of MC are examined. AFM images of front and back side of MC is shown in figure 4.13(a) and (b) with an estimated RMS roughness of 1.6 nm and 3.8 nm, respectively. Typical horizontal cross section line profile of the images is shown in inset. The higher surface roughness on back side of MC is expected during bulk microfabrication, since the MC will be released in the final step by chemical etching using TMAH or KOH [47]. The estimated root mean square inclination angle $\langle\theta^2\rangle^{1/2}$ from the measured RMS roughness on front and back sides is 62° and 135° , respectively. This data clearly indicates that the inclination has a decisive role in bending of the MC, indicating that out of plane surface stress components couple into the in-plane stress via transverse elastic coupling [2].

Apart from the measured RMS roughness, which is $< 5\text{nm}$ on both the sides, one needs to look at the surface features, as it also plays a crucial role in bending of MC

[1]. These features act as quasi 3D structures which increases the surface area and thus the number of available binding sites for adsorption. In addition, it produces confinement of the molecules in cavities, increasing the intermolecular forces (such as the solvation, steric, osmotic, and hydration forces [41, 42]) acting as localized stress concentration regions or simply “stress concentrators” [1]. It is also possible that around stress concentrators, water molecules get preferentially adsorbed in the form of dispersed islands.

We define a stress concentrator as a feature whose height is above a ‘certain’ threshold value for a given average surface roughness. The number of stress concentrators is estimated by performing grain size distribution analysis on the AFM images. This analysis revealed, there are 108 and 203 stress concentrators present on front and back surfaces, respectively and their mean height distribution is shown as insets of figure 4.13(a) and (b). We envisage the difference in the number of stress concentrators on opposite sides is responsible for the deflection of the uncoated MC studied in the present work. Presence of more number of stress concentrators on back side results in compressive stress during desorption thereby bending the MC in the direction of back side which is seen as positive deflection signal in figure 1 and vice versa. Our results are in agreement with those of Hayden et al [1], wherein their simulations have also shown that with increasing surface roughness, the MC deflection increases because of the increase in stress concentrators.

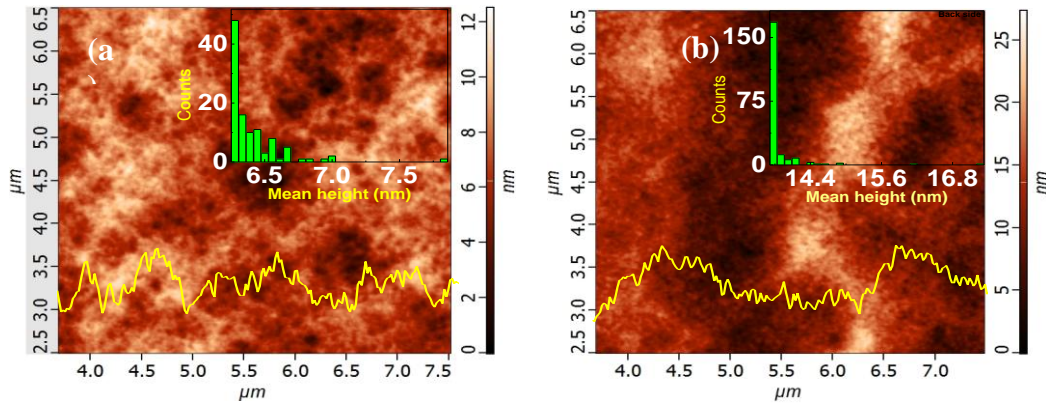


Figure 4.13 Surface morphology of (a) front and (b) back side Si microcantilever used in the present study. Scan area is $4 \times 4 \mu\text{m}^2$. Inset shows a typical horizontal cross section line profile. Inset also shows the histogram plots of “stress concentrators” on front and back surface. This was estimated by considering a threshold surface at 50 % from maximum height in each case.

To further support our argument, an experiment under identical conditions is performed on another MC from same batch, with almost equal RMS roughness (~ 2 nm) on both the sides. The deflection response of this MC (with equal roughness) along with the former MC (with unequal roughness) is shown in figure 4.14. This figure also shows the AFM images of both sides of MC.

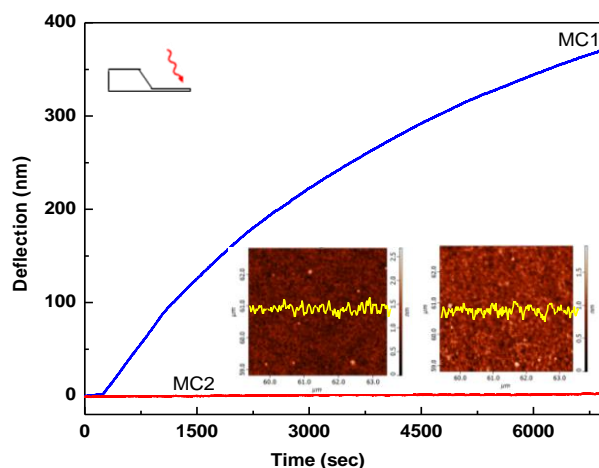


Figure 4.14 Deflection response of MC1 and MC2 during desorption of water molecules when RH is switched from 50 % RH to 6 %. Inset shows Surface morphology of front and back side of MC2. The estimated RMS roughness is ~ 2 nm on both sides. This result is a experimental evidence for the roughness induced MC bending.

The MC(s) did not show any bending and further analysis from the AFM images (fig) did not reveal the presence of stress concentrators. Further, $\langle\theta^2\rangle^{1/2}$ computed from the measured RMS roughness on front and back side are almost equal in magnitudes, with values 77° and 81° , respectively. We believe that absence of stress concentrators and equal surface inclination on opposite sides does not generate differential surface stress and hence no bending is seen. It further confirms that an uncoated Si MC with differential surface topologies on opposite sides can be effectively used as a sensor (in particular, humidity) with good sensitivity and repeatability with a response time of ~ 2.5 minutes.

In conclusion, we have demonstrated that uncoated MC can be as sensitive to adsorption of analytes and water in particular, as passivated / functionalized ones. Experiments were conducted to show that the observed large bending is not an experimental artifact. The role played by differences in surfaces features quantified in terms of stress concentrators clearly elucidated the origin of bending. The RMS surface inclination of the grains supports the theoretical work of Weissmuller and Duan [2] justifying the idea that out of plane stress components couple to the in plane stress components through the transverse elastic coupling. It is therefore concluded that difference in stress concentrators and their geometry on opposite sides is necessary for MC bending.

4.5 Conclusions

This chapter deals with the dynamic and static response of uncoated silicon microcantilever when exposed to water molecules.

- Influence of surface stress on microcantilever stiffness during adsorption of water molecules is studied by varying relative humidity. We estimated the stiffness change (from resonance frequency shift) and differential surface stress generated (from static bending data) during adsorption in three microcantilevers with reducing dimensions.
- It is concluded that the surface stress generated during adsorption influences the stiffness of microcantilever and this effect increases with reducing the dimensions of the same.
- The stiffness change estimated was found to follow a linear relationship with differential surface stress scaled to the cube of width to height ratio of microcantilevers validating the model of Lachut et al [28].
- It is pointed out that reducing the dimensions of the microcantilever can greatly influence the adsorption induced stiffness changes and care must be exercised while interpreting the observations.
- The possibility of using higher order modes of vibration of silicon microcantilever for relative humidity detection is also studied. It is concluded that compared to fundamental mode, higher bending mode of a microcantilever is more sensitive to RH. The sensitivities are estimated as 0.18 Hz/%RH and 48 Hz/%RH for VB1 and VB7 respectively.
- We have estimated the activation energy for an uncoated MC1 from the mass data and was found to be 12.0 kJ mol⁻¹. This confirms the adsorption of water on silicon microcantilever was multilayer adsorption.
- Surface stress variation during adsorption was found to follow Langmuir isotherm with a rate constant of 0.0024 s⁻¹. This indicates that the surface

stress generated is proportional to the number of excess water molecules adsorbed on back side of the cantilever.

- The origin of bending of uncoated MCs during water adsorption is studied. It is found that the inherent difference in the surface roughness of the front and back side of the microcantilever is the reason for the observed deflection. It is concluded that the presence of large number of stress concentrators on back side is responsible for the generation of stress during water adsorption.
- Our results point out that uncoated Si microcantilever can be used for relative humidity detection with good sensitivity and repeatability with a response time of ~2.5 minutes.

4.6 References

1. V. C. Hayden, S. M. Saydur Rahman and L. Y. Beaulieu, *J. Appl. Phys.* 113, (2013) p.054501
2. J. Weissmuller and H.L. Duan., *Phys. Rev. Lett.*, 101, (2008) p.146102
3. Mo Li, H.X Tang and M.L Roukes, *Nature Nanotechnol.* 2, (2007) p.114-120
4. P.S. Waggoner and H.G. Craighead, *J. Appl. Phys.* 105, (2009) p.054306
5. J. Tamayo, D. Ramos, J. Mertens, and M. Calleja, *Appl. Phys. Lett.* 89, (2006) p.224104
6. G.Y.Chen, T.Thundat, E.A.Wachter, R.J.Warmack, *J. Appl. Phys.* 77, (1995)p. 3618–3622
7. A. K. Gupta, P. R. Nair, D. Akin, M. R. Ladisch, S. Broyles, M. A. Alam and R. Bashir, *Proc. National Acad. Sci.* 103, (2006) p.13362
8. T. Thundat, G.Y. Chen, E.A. Wachter, D. P. Allison and R.J. Warmack, *Anal.Chem.*67, (1994) p.519
9. J. Lagowski, H. C. Gatos, and E. S. Sproles, *Appl. Phys. Lett.* 26, (1975)p. 493

10. P.C.Y. Lee, Y.S. Wang, X. Markenscoff, *J. Acoust. Soc. Am.* 57, (1975) p.95
11. Y.T. Yang, C. Callegari, X.L. Feng, K.L. Ekinici, M.L. Roukes, *Nano Lett.* 6, (2006) p.583
12. A.W. McFarland, M. A. Poggi, M. J. Doyle, L. A. Bottomley, and J. S. Colton, *Appl. Phys. Lett.* 87, (2005) p.053505
13. K. S. Hwang, K. Eom, J. H. Lee, D.W. Chun, B. H. Cha, D. S. Yoon, T. S. Kim, and J. H. Park, *Appl. Phys. Lett.* 89, (2006) p.173905
14. D. Ramos, J. Tamayo, J. Mertens, M. Calleja, A. Zaballos, *J. Appl. Phys.* 100, (2006)p. 106105
15. A. K. Naik, M. S. Hanay, W.K. Hiebert, X. L. Feng, and M. L. Roukes, *Nature Nanotech.* 4, (2009)p. 445
16. S. Cherian and T. Thundat, *Appl. Phys. Lett.* 80, (2002)p.2219
17. T. Braun, V. Barwich, M.K. Ghatkesar, A.H. Bredekamp, C. Gerber, M. Hegner, H.P. Lang, *Phys. Rev. E.* 72, (2005) p.031907
18. D.W. Chun, K.S. Hwang, K. Eom, J.H. Lee, B.H. Cha, W.Y. Lee, D.S. Yoon, T.S. Kim, *Sens. Actuat. A* 135, (2007) p.857
19. T.Y. Kwon, K. Eom, J.H. Park, D.S. Yoon, T.S. Kim, H.L. Lee, *Appl. Phys. Lett.* 90, (2007) p.223903
20. Z. Hu, T. Thundat, R.J. Warmack, *J. Appl. Phys.* 90, (2001) p.427
21. D.W. Dareing, T. Thundat, *J. Appl. Phys.* 97, (2005) p.043526
22. G. Huang, W. Gao, S. Yu, *Appl. Phys. Lett.* 89, (2006) p.043506
23. P. Lu, H.P. Lee, C. Lu, S.J. O'Shea, *Phys. Rev. B* 72, (2005) p.085405
24. R. B. Karabalin, L. G. Villanueva, M. H. Matheny, J. E. Sader and M. L. Roukes, *Phys. Rev. Lett.* 108, (2012) p. 236101
25. L.Feng, F. Gao, M.Lie, S.Wang, L.Li, M.Shen and Z.Wang, *J. Appl. Phys.* 112, (2012) p.013501
26. X. Yi, H.L. Duan, *J. Mech. & Phys. Soild.* 57, (2009)p.1254-66
27. J. Tamayo, J.J. Ruz, V. Pini, P. Kosaka and M. Calleja, *Nanotech.* 23, (2012) p.475702
28. M. J. Lachut and J. E. Sader, *Phys. Rev. Lett.* 99, (2007)p.206102 :
M.J.Lachut and J.E.Sader, *Phys.Rev.B* 85, (2012) p.085440

29. L.Qiao and X.Zheng, *J.Appl.Phys.* 113, (2013) p.013508
30. D.B. Assay and S.H. Kim, *J. Phys. Chem. B.* 109, (2005) p.16760figure 2.
31. H.S.Wasisto, S. Merzsch, A. Waag, E. Uhde, T. Salthammer, E. Peiner,
Sens. Actuators B. 180, (2013) p.77-89
32. G. Muralidharan, A. Wig, L.A. Pinnaduwege, D. Hedden, T. Thundat and
R.T. Lareau, *Ultramicroscopy* 97, (2003) p.433-439
33. L.A.Pinnaduwege, T.Thundat, A.Gehl, S.D.Wilson, D.L.Hedden, R.T.
Lareau, *Ultramicroscopy* 100, (2004) p.211-216
34. Prashanth Raghu, Chris Yim and Farhang Shadman, *Kinetics and catalysis*,
50(8), (2004) p.1881-8
35. W. Haiss, *Rep. Prog. Phys.* 64, (2001)p.591
36. M. Godin, V.T. Cossa, Y. Miyahara, T. Monga, P.J. Williams, L.Y.
Beaulieu, R.B. Lennox and P. Grutter, *Nanotech.*21, (2010) p.075501
37. H. Ibach, *Surf. Sci. Rep.* 29, (1997)p.195
38. N.V. Lavrik, C.A. Tipple, M.J. Sepaniak, P.G. Datskos, *Chem. Phys. Lett.*
336, (2001) p. 371
39. N.V. Lavrik, C.A. tipple, *Biomed. Microdevices*, 3, (2001) p.35
40. V. Tabad Cossa, M. Godin, I.J. Burqess, T. Monga, R.B. Lennox and P.
Grutter, *Anal. Chem.*79, (2007) p.8136
41. J. Mertens, M. Calleja, D. Ramos, A. Taryn and J. Tamayo, *J. Appl. Phys.*
101, (2007) p.034904
42. J.J. Headrick, M.J. Sepaniak, N.V. Lavrik, P.G. Datskos, *Ultramicroscopy.*
97, (2003) p. 417
43. M. Godin, P. J. Williams, V. Tabard-Cossa, O. Laroche, L. Y. Beaulieu, R.
B. Lennox, and P. “Grutter, *Langmuir* 20, (2004) p.7090–7096
44. R. Desikan, I. Lee, and T. Thundat, *Ultramicroscopy* 106, (2006) p.795–799
45. S. Stolyarova S. Cherian, R. Raiteri, J. Zeravik, P. Skladal and Y.
Nemirovsky, *Sens. Actuat.B.* 131, (2008) p.509–515
46. S. Tetin, B. Caillard, F. Menil, H. Debeda, C. Lucat, C. Pellet, I. Dufour,
Sens. Actuat. B. 14, (2010) p.555–560.
47. V.Jovic, J.Lamovec, M.Popovic and Z.Lazic, *J.Serb.Chem.Soc.*72 (11)
(2007) p.1127-1138

Chapter 5 - Summary and Scope of future work

Present thesis addressed two important aspects of microcantilever based sensors and the conclusions are given below.

Microcantilever based mass sensors

- Four vertical bending mode shapes of a microcantilever (MC) are mapped experimentally using Nano vibration Analyzer successfully and are compared with FEM simulation results.
- It is proved that mass sensitivity increases linearly with increase of eigenvalue (λ_n^2) and decreasing dimensions (T/L^2) where T is thickness and L is length of MC. It is pointed out that although mass sensitivity can be enhanced by either method, quality factor, which is an important parameter for sensor characterization, reduces after the addition of polymer mass at higher modes.
- Using, FEM simulations, it is shown that mass sensitivity of MCs can be enhanced by attaching nanostructures like nanobelt, nanowire and nanotube at the free end. It is proved that mass sensitivity can be enhanced by introducing a step discontinuity along the length of the cantilever. It is also proved that mass sensitivity is dependent on the position of mass loading in cantilever based mass sensors.

- Demonstrated that PVP coated MC can be effectively used as gamma radiation dosimeters. Since the damage occurs only in PVP, the same Si MC can be re-used by once again coating with a fresh PVP.
- Demonstrated that micro-Raman spectroscopy can be effectively used as a tool to study residual stress in microcantilever.

Adsorption of water molecules on uncoated Si microcantilevers

- Experimental evidence is presented to show that the effect of dimensions of microcantilever leads to three distinct behaviors clearly depicting the competition between mass loading and stiffness changes. It is concluded that the surface stress generated during adsorption influences the stiffness of MC and this effect increases with reducing the dimensions of the same.
- The stiffness change estimated was found to follow a linear relationship with differential surface stress scaled to the cube of width to height ratio of MCs validating the model of Lachut et al [1].
- It is concluded that even uncoated MCs with tailored topology can be as sensitive as passivated ones. It is shown that the inherent difference in the surface roughness of the front and back side of the microcantilever is the reason for the observed deflection of uncoated MCs. Present results point out that uncoated Si MC can be used for relative humidity detection with good sensitivity and repeatability with a response time of ~2.5 minutes.

Future work

1. In the present work, it is shown that MC mass sensitivity can be enhanced by working at higher modes. Role of mode shape on the enhanced sensitivity of these sensors can be carried out as a future work.
2. In this thesis, we have observed dimensional dependence of adsorption induced stiffness changes in microcantilever with scaling factor of surface stress. In order to further understand these results, more experiments should be performed with different aspect ratios of microcantilever. Similarly, adsorption studies to be performed with different chemical solutions like alcohol vapors, etc at different temperatures.
3. The potential of uncoated MC for humidity detection is demonstrated in the present work. Further experiments on the use and limitations of uncoated MCs for sensing other vapors can be undertaken.

Reference

1. M. J. Lachut and J. E. Sader, *Phys. Rev. Lett.* 99, 206102 (2007); M.J.Lachut and J.E.Sader, *Phys.Rev.B* 85, 085440 (2012)

Publications:

a. Journal Publications:

1. **K.Lakshmoji**, K.Prabakar, A.Kumar, J.Brijitta, J.Jayapandian, B.V.R.Tata, A.K.Tyagi and C.S.Sundar, Microcantilever-based mass sensors:working at higher modes against reducing the dimensions, *Micro & Nano Letters*, Vol.7, Iss.7, pp. 613-616, 2012.
2. **K.Lakshmoji**, K.Prabakar, Atul Kumar, J.Jayapandian and A.K.Tyagi, Enhancing the mass sensitivity of nanocantilever, *International Journal of Nanoscience*, Vo.11, No.1, 1250002, 2012.
3. **K.Lakshmoji**, K.Prabakar, R. Mythili, J.Jayapandian, *Effect of UV light on the bending properties of piezoresistive microcantilevers*, Proceedings of “International Conference on Nanoscience, Engineering and Technology (ICONSET 2011)” held at Sathyabama University, Chennai, IEEE Conf. series (December, 2011) 518 – 519.
4. **K.Lakshmoji**, K. Prabakar, S. Tripura Sundari, J. Jayapandian, A.K. Tyagi and C.S. Sundar, Origin of bending in uncoated microcantilever-Surface topography?, *Appl. Phys. Lett.*, 104, 041602, 2014.
5. **K.Lakshmoji**, K.Prabakar, S. Tripura sundari, J.Jayapandian and C.S.Sundar, Effect of surface stress on microcantilever resonance frequency during water adsorption: influence of microcantilever dimensions (*Ultramicroscopy*, revised)

b Conference proceedings:

1. **K.Lakshmoji**, K.Prabakar, J.Jayapandian, Relative humidity detection using higher modes of microcantilevers, Proceedings of the 9th Nanomechanical

Sensing workshop, held at IIT Bombay, Mumbai on 6th-8th June, 2012. pp.162-163

2. Atul Kumar, K. Prabakar, **K. Lakshmoji** and J. Jayapandian, Thermomechanical analysis of bimaterial cantilever, Presented at Fourth ISSS National Conference on Microsystems, Smart Materials, and Structures Organized by Visvesvaraya National Institute of Technology (VNIT), Nagpur September 30th, - Oct. 01st, 2010.
3. **K. Lakshmoji**, K. Prabakar, Atul Kumar, S. Dhara, J. Jayapandian, A.K. Tyagi and C.S. Sundar, “Micro-Raman spectroscopy on Si microcantilevers” International Conference on Nanoscience and Technology organized by International Advanced Research Center for Powder Metallurgy and New Materials (ARCI), Hyderabad, Jan 20-23,2012. (Abstract)
4. **K.Lakshmoji**, K. Prabakar, Atul Kumar, J. Jayapandian, A.K.Tyagi and C.S.Sundar, Tailoring the nano cantilever for enhanced sensitivity, Presented at International Conference on Nano science and Technology organized by IIT Mumbai, February 17th-20th, 2010. (Abstract)

Appendix A – Programs used in NVA

A – 1 Program for estimation of natural frequency of MC

Program used:

```
; This script shows the usage of the external generator control
; We sweep the excitation frequency of a piezo bar and determine
; first set some variables to make an adaption more easy

SET startfreq=3800 fstep=100
; prepare the measurement
; you have to adapt this, for your sample rate

PREPARESTART samplerate=20000 blocklen=32768 trigger=false
; set the generator to start frequency
; the amplitude should be set manually

GENERATOR frequency=startfreq output=true
; wait for the generator to set up

WAIT delay=3000
; set a label for the jump statement
LABEL number=0

; Begin with measurement
; the timeout parameter lets wait until block is acquired,
; if a lot of more blocks should be measured don't forget to adapt the timeout value

START BLOCKS=20 timeout=60000

; set Frequency
GENERATOR deltaf=fstep
; wait until we can be sure that the generator has set the requested frequency
WAIT delay=3000

; now jump to the label with the number=0
; if the frequency is lower than the
IF _frequency<=5000 JUMP number=0

; stop the measurement (counterpart of preparestart)
STOP
; save the results, a questionmark as name will ask for the name
SAVE file=?
```

A – 2 Program for mapping the mode shape of vibration of MC

Program used:

```
; This script scans a cantilever of an AFM
; The cantilever has a rectangle shape with a triangle tip
; The rectangle is scanned with help of two nested loops
; The triangle tip portion is scanned with single data points

; first prepare the software for the measurement
; because we want to reconstruct the movement with the SIOS3Dviewer,
; the measurement must be triggered to preserve the phase conditions between the blocks
```

```
PREPARESTART samplerate=50000 blocklen=32768 trigger=true triggersource=true
; the following statements are created with the wizard from saved positions (using the
crosstable control)
```

```
; now the rectangular field
; move to the begin
MOVE_CT x=0 y=0 timeout=3000
WAIT delay=1000
```

```
; set a label for the loop
LABEL number=0
; measure position
START blocks=10 timeout=60000
```

```
; move relative 2µm to the next position in the row
MOVEREL_CT x=1 y=0 timeout=3000
```

```
WAIT delay=1000
; jump back to label with number=0, 4 times, count the jumps with counter0
JUMP counter=0 counts=10 number=0
```

```
; next column
MOVEREL_CT x=-10 y=10 timeout=3000
```

```
WAIT delay=1000
; reset the counter0 for the next inner loop
DEL COUNTER counter=0
; jump to the begin of the loop, 12 times; count the jumps with counter1
JUMP counter=1 counts=18 number=0
```

```
; ready, stop the measurement
STOP
WAIT delay=3000
```

```
; save the data
SAVE file=cantilever1.mds
```